

NAVAL POSTGRADUATE SCHOOL

Monterey, California



CONTRACT REPORT

AN ANALYSIS OF THE WYNGAARD-LEMONE MODEL OF
REFRACTIVE INDEX AND MICROMETEOROLOGICAL STRUCTURE
FUNCTIONS AT THE TOP OF A TURBULENT MIXED LAYER

C. W. Fairall
BDM Corporation
P.O. Box 2019
Monterey, CA 93940

October 1982

Report for the period 15 April - 30 Sept 1982

Approved for public release; distribution unlimited.

Prepared for: Naval Environmental Prediction Research Facility
Monterey, California 93940

Fed 1013
D 208 14/2: DPS-63-82: COVER

NAVAL POSTGRADUATE SCHOOL
Monterey, California 93940

Rear Admiral J. J. Ekelund
Superintendent

D. A. Schrady
Provost

The work reported herein was carried out for the Naval Environmental Prediction Research Facility by BDM Corporation under Work Order 1202, Contract Number N00014-82-C-0251. The work was part of a program entitled "Optical turbulence in the Marine Boundary Layer," funded by the Naval Environmental Prediction Research Facility and under the cognizance of Prof. K. L. Davidson.

Reproduction of all or part of this report is authorized.

This report was prepared by:

Unclassified

SECURITY CLASSIFICATION OF THIS PAGE (When Data Entered)

REPORT DOCUMENTATION PAGE		READ INSTRUCTIONS BEFORE COMPLETING FORM
1. REPORT NUMBER NPS63-82-006 CR	2. GOVT ACCESSION NO.	3. RECIPIENT'S CATALOG NUMBER
4. TITLE (and Subtitle) An Analysis of the Wyngaard-LeMone Model of Refractive Index and Micrometeorological Structure Functions at the Top of a Turbulent Mixed Layer		5. TYPE OF REPORT & PERIOD COVERED Contractor Report 15 Apr 82 - 31 Sep 1982
7. AUTHOR(s) C. W. Fairall		6. PERFORMING ORG. REPORT NUMBER
9. PERFORMING ORGANIZATION NAME AND ADDRESS BDM Corporation P.O. Box 2019 Monterey, CA 93940		8. CONTRACT OR GRANT NUMBER(s) N00014-82-C-0251
11. CONTROLLING OFFICE NAME AND ADDRESS Naval Environmental Prediction Research Facility Monterey, California 93940		10. PROGRAM ELEMENT, PROJECT, TASK AREA & WORK UNIT NUMBERS Work Order 1202
14. MONITORING AGENCY NAME & ADDRESS (if different from Controlling Office)		12. REPORT DATE October 1982
		13. NUMBER OF PAGES 101
		15. SECURITY CLASS. (of this report) Unclassified
		15a. DECLASSIFICATION/DOWNGRADING SCHEDULE
16. DISTRIBUTION STATEMENT (of this Report) Approved for public release; distribution unlimited.		
17. DISTRIBUTION STATEMENT (of the abstract entered in Block 20, if different from Report)		
18. SUPPLEMENTARY NOTES Principal Investigator, K. L. Davidson, Professor of Meteorology, Naval Postgraduate School, Monterey, CA 93940		
19. KEY WORDS (Continue on reverse side if necessary and identify by block number)		
20. ABSTRACT (Continue on reverse side if necessary and identify by block number) The Wyngaard and LeMone (1980) model of interfacial turbulence structure functions (temperature, C_T^2 , and water vapor, C_Q^2) in an entraining mixed layer is analyzed. The model indicates that in the interfacial region $z \approx z_i$ C_X^2 is proportional to $(\Delta X)^2 z_i^{-2/3} \theta_{v*}/\Delta \theta_v$ where $X = T$ or Q , ΔX is the jump in X across the interface, z_i is the height of the interface, and θ_{v*} is the convective mixed layer scaling parameter for temperature. Although based on a number of assumptions (referred to as the "quasi-steady"		

DD FORM 1 JAN 73 1473

EDITION OF 1 NOV 65 IS OBSOLETE
S/N 3102-014-5601

Unclassified

SECURITY CLASSIFICATION OF THIS PAGE (When Data Entered)

Unclassified

SECURITY CLASSIFICATION OF THIS PAGE(When Data Entered)

approximation), the model is found to have more general application. A theoretical analysis indicated that the model might not apply where $\Delta\theta_v$ is large (on the order of 10 K), particularly for C_T^2 . A comparison against 23 aircraft profile measurements revealed that the model agreed within a factor of three.

Unclassified

SECURITY CLASSIFICATION OF THIS PAGE(When Data Entered)

ABSTRACT

The Wyngaard and LeMone (1980) model of interfacial turbulence structure functions (temperature, C_T^2 , and water vapor, C_Q^2) in an entraining mixed-layer is analyzed. The model indicates that in the interfacial region ($Z \approx Z_i$) C_X^2 is proportional to $(\Delta X)^2 Z_i^{-2/3} \theta_{v*}/\Delta\theta_v$ where $X = T$ or Q , ΔX is the jump in X across the interface, Z_i is the height of the interface, and θ_{v*} is the convective mixed-layer scaling parameter for temperature. Although based on a number of assumptions (referred to as the "quasi-steady" approximation), the model is found to have more general application. A theoretical analysis indicated that the model might not apply where $\Delta\theta_v$ is large (on the order of 10 K), particularly for C_T^2 . A comparison against 23 aircraft profile measurements revealed that the model agreed within a factor of three.

CONTENTS

Abstract	ii
Table of Contents	iii
List of Tables	iv
List of Figures	v
I. Introduction	1
II. Theory	2
A. Background	2
B. Evaluation of $\langle X \rangle$	3
C. Structure Functions	8
D. Discussion	11
III. Atmospheric Data	16
A. Measurement Techniques	16
B. Surface Fluxes and Scaling Parameters	16
C. Data Sets.	18
IV. Results	21
V. Conclusions	35
References	37
Appendix A	38

LIST OF TABLES

- Table 1. Meteorological data and surface scaling parameters from the cloud free NPS data sets.
- Table 2. Surface scaling ($\overline{w\theta}_{vs}$ and L), convective scaling (W_* , θ_{v*} and ϵ_i) and inversion scaling (R , S and W_{eo}) parameters. Two formulae are used to estimate W_{eo} : "steady" is Eq 20 and "Lilly" is Eq 64.
- Table 3. Measured values of the interfacial structure functions (C_T^2 and C_Q^2) and their resultant values for
- $$I_X = z_i^{2/3} C_X^2 / ((\Delta X)^2 D_X F_X) \text{ where } X=T \text{ or } Q$$
- These are compared with theoretical values, I_c , using the "steady" and "Lilly" entrainment values.

LIST OF FIGURES

- Figure 1. Schematic representation of the convective boundary layer (taken from Wyngaard and LeMone, 1980) with its interfacial layer showing h_0 , z_i , h_2 , Δh , fluxes and jumps. Note that $\Delta\theta_v = \theta_v(h_2) - \theta_v(h_0)$ is positive while ΔQ is negative.
- Figure 2a. Comparison of measured inversion layer structure function, C_T^2 , versus WL theory. The data points are indicated by the first letter (P,W,M,B) of the experiment.
- Figure 2b. Similar to Fig. 2a but for C_Q^2 .
- Figure 3. Theoretical expression for H_T and H_Q (Eq. 68) illustrating the difference between the dependence of C_T^2 and C_Q^2 on $\Delta\theta_v$ and ΔQ .
- Figure 4a. A comparison of the measured value of I_T (Eq. 65) and the theoretical value (Eq. 66) for the "quasi-steady" entrainment formula.
- Figure 4b. Similar to Fig. 4a but for C_Q^2 .
- Figure 5a. The measured value of C_T^2 divided by the WL model value as a function of $\Delta\theta_v$.
- Figure 5b. Similar to Fig. 5a but for C_Q^2 .
- Figure 6. The measured value of C_T^2 divided by the model value using the simplified expression (Eq. 70).

I INTRODUCTION

This report is a theoretical and experimental analysis of a model (Wyngaard and LeMone, 1980) used to calculate the refractive index structure function parameter, C_n^2 , at the interfacial region at the top of an entraining, turbulent mixed layer. C_n^2 is related to the micrometeorological structure functions for temperature, C_T^2 , humidity, C_Q^2 , and T-Q covariance, C_{TQ} . The mixed layer interfacial region is important for EM propagation because C_n^2 is greatly increased by large T and Q fluctuations due to the entrainment of warm, dry air from the nonturbulent atmosphere above the mixed layer.

Assuming that the rate of entrainment is in equilibrium with the free tropospheric virtual potential temperature (buoyancy) lapse rate, the model indicates that C_X^2 is proportional to $(\Delta X)^2 \theta_{v*} Z_i^{-2/3} / \Delta \theta_v$ where X is T or Q, ΔX the jump at the interface, Z_i the height of the boundary layer and θ_{v*} the convective temperature mixed layer scaling parameter. The theoretical basis of this model is examined and four data sets from the NPS aircraft measurements program are used to test the model.

II THEORY

A. Background

The structure function parameters for temperature, C_T^2 , and specific humidity, C_Q^2 , are to be evaluated in the inversion region by averaging between heights $z = h_0$ and $z = h_2$ (see Fig. 1). The complete theory was developed by Wyngaard and LeMone (1980), hereafter referred to as WL, so only a summary of the derivation will be presented in this report. In a few instances WL's work will be expanded to make certain assumptions and manipulations more explicit.

The height h_0 is defined as the top of the mixed layer where $\overline{w\theta}_v = 0$. At h_2 both fluxes and flux divergences are equal to zero. The average structure functions are

$$\langle C_T^2 \rangle = \Delta h^{-1} \int_0^2 C_T^2 dz \quad (1a)$$

$$\langle C_Q^2 \rangle = \Delta h^{-1} \int_0^2 C_Q^2 dz \quad (1b)$$

where $\Delta h = h_2 - h_0$ and the 0, 2 on the integral denotes h_0, h_2 .

The average structure functions are related to their respective dissipation rates by the Corrsin equation

$$\langle C_T^2 \rangle = 1.6 \langle \epsilon \rangle^{-1/3} \langle \chi_\theta \rangle \quad (2a)$$

$$\langle C_Q^2 \rangle = 1.6 \langle \epsilon \rangle^{-1/3} \langle \chi_Q \rangle \quad (2b)$$

where ϵ is the rate of dissipation of turbulent kinetic energy, X and X_Q are the scalar dissipation rates (the factor 1.6 implies X is the rate of dissipation of temperature variance $\overline{\theta^2}$).

B. Evaluation of $\langle X \rangle$

For the moment, the development will be confined to the specific humidity (Q). The dissipation rate is calculated from the scalar variance budget equation (Q denotes mean while q denotes fluctuating specific humidity; later in the paper q will denote mixing ratio, Q/ρ).

$$dv/dt + Wdv/dZ + d(\overline{wq})/dZ + 2 \overline{\rho wq} d(Q/\rho)/dZ = -X_Q \quad (3)$$

where $v = \overline{q^2}$, W is the mean vertical velocity (subsidence) and ρ is the density of air. Integrating this equation from h_0 to h_2 , as in Eq. 1, yields

$$\langle X_Q \rangle = -\langle D_Q \rangle - \langle T_Q \rangle - \langle P_Q \rangle \quad (4)$$

where D is the first two terms in Eq. 3, T (transport) the third and P (gradient production) the fourth. Assuming "quasi-steady" conditions, WL show that $\langle D_Q \rangle$ and $\langle T_Q \rangle$ are negligible compared to $\langle P_Q \rangle$; therefore

$$\langle X_Q \rangle = -\langle P_Q \rangle \quad (5)$$

At this point the generalized inversion structure model (Deardorff, 1979) is introduced

$$Q = Q_0 + \Delta Q f(Z); \quad h_0 < Z < h_2 \quad (6a)$$

$$dQ/dZ = \Delta Q df/dZ \quad (6b)$$

where $f(Z)$ describes the shape of the Q profile in the inversion region (assumed to be the same for Q and T) with $f(h_0) = 0$ and $f(h_2) = 1$, Q_0 is the mixed layer value and ΔQ the jump in Q across the inversion. Substituting Eq. 6b into Eq. 5 and integrating by parts one obtains

$$-\langle P_Q \rangle \Delta h = 2 \Delta Q \int_0^2 d(\overline{wQ})/dZ f dZ \quad (7)$$

The mean Q continuity equation

$$-d(\overline{wQ})/dZ = dQ/dt + W dQ/dZ \quad (8)$$

is used in Eq. 7 to obtain

$$-\langle P_Q \rangle \Delta h = -2\Delta Q \int_0^2 dQ/dt f dZ - 2\Delta Q \int_0^2 W dQ/dZ f dZ \quad (9)$$

The time derivative of Eq. 6a

$$dQ/dt = dQ_0/dt + f d\Delta Q/dt \quad (10)$$

and Eq. 6b can be substituted into Eq. 1a. First the "quasi-steady" assumption is invoked, setting the following conditions

$$d\Delta Q/dt = 0 \quad (11a)$$

$$d\Delta\theta_v/dt = 0 \quad (11b)$$

$$dh_o/dt = 0 \quad (11c)$$

$$d\Delta h/dt = 0 \quad (11d)$$

However, since

$$dh_o/dt = W_o + W_{eo} \quad (12)$$

then Eq. 11c implies $W_{eo} = -W_o$. Assuming constant divergence

$$W = W_o Z/h_o \quad (13a)$$

$$dW/dZ = W_o/h_o \quad (13b)$$

$$W_2 = (1 + \alpha) W_o \quad (13c)$$

where $\alpha = \Delta h/h_o$ is the normalized thickness of the interfacial region. Employing these relations in Eq. 9 and doing the second integral by parts gives

$$-\langle P_Q \rangle \Delta h = -2\Delta Q h Y_Q dQ_o/dt + (\Delta Q)^2 W_{eo} (1 + \alpha - \alpha Z_Q) \quad (14)$$

where the interfacial functions Y_Q and Z_Q are

$$Y_Q = \Delta h^{-1} \int_0^2 f \, dz \quad (15a)$$

$$Z_Q = \Delta h^{-1} \int_0^2 f^2 \, dz \quad (15b)$$

The time derivative term in Eq. 14 is eliminated by integrating the conservation equation (Eq. 10) from h_0 to h_2

$$\Delta h dQ_0/dt - W_{e0} \Delta Q (1 + \alpha - \alpha Y_Q) = \overline{wq_0} \quad (16)$$

which is substituted into Eq. 14 to obtain (WL Eq. 42)

$$-\langle P_Q \rangle \Delta h = -2\Delta Q Y_Q \overline{wq_0} + (\Delta Q)^2 W_{e0} [-2Y_Q(1 + \alpha - \alpha Y_Q) + (1 + \alpha - \alpha Z_Q)] \quad (17)$$

Later in their paper, WL use the equation

$$-\Delta Q W_{e0} (1 + \alpha - \alpha Y_Q) = \overline{wq_0} \quad (18)$$

which, in view of Eq. 14, obviously implies $dQ_0/dt = 0$. Since WL have already required that $d\Delta Q/dt = 0$, this solution appears to be quite restrictive. If Eq. 18 is used in Eq. 17 then

$$-\langle P_Q \rangle \Delta h = (\Delta Q)^2 W_{e0} (1 + \alpha - \alpha Z_Q) \quad (19)$$

Despite the simplicity of Eq. 19, WL prefer to keep the $\overline{wq_0}$ term separate in their development. The primary reason for this is to simplify the analogous development for θ_v , since $\overline{w\theta_{v0}} = 0$. Therefore, WL now employ the "quasi-steady" entrainment formula

$$W_{eo} = 0.8 W_* S^{-1}/(1+\alpha) \quad (20)$$

where

$$S = g \Gamma_{\theta 2} h_0^2 / (W_*^2 T) \quad (21)$$

with $\Gamma_{\theta 2} = d\theta_v/dZ$ at $Z = h_2$ and W_* is the convective scaling velocity ($Z_i = h_0/0.8$)

$$W_*^3 = g \overline{w\theta}_{vs} Z_i / T \quad (22)$$

and "s" denotes the surface value.

Rather than make an explicit substitution for W_{eo} at this point, one could keep W_{eo} as a variable, giving

$$\langle X_Q \rangle = -2\Delta Q Y_Q \overline{wq}_0 / (\alpha h_0) + (\Delta Q)^2 W_{eo} (1+\alpha) S F_Q / h_0 \quad (23)$$

where

$$F_Q = [-2Y_Q (1+\alpha-\alpha Y_Q) + (1+\alpha-\alpha Z_Q)] / (\alpha(1+\alpha)S) \quad (24)$$

Using the WL solutions obtained for Eq. 24 (and $Y_Q \approx 1/2$)

$$F_Q = (6R)^{-1} \quad (25)$$

then

$$\langle X_Q \rangle = -\Delta Q \overline{wq}_0 Y_Q / (\alpha h_0) + (\Delta Q)^2 W_{eo} (1+\alpha) S / (6R h_0) \quad (26)$$

Where

$$R = g \Delta\theta_v h_0 / (W_*^2 T) \quad (27)$$

The final result is obtained by substituting for \overline{wq}_0 in Eq. 26. First the θ_v continuity equations at h_0 and at h_2 are

combined with the h_0 to h_2 integral form similar to Eq. 16 to produce the relation

$$d \Delta\theta_v/dt + w_{eo} \Delta h(1+\alpha)\Gamma_{\theta 2} - w_{eo} \Delta\theta_v(1+\alpha-\alpha Y_Q) = \overline{w\theta_{v0}} \quad (28)$$

Since WL assume $d\Delta\theta_v/dt = \overline{w\theta_{v0}} = 0$,

$$\Delta\theta_v(1+\alpha-\alpha Y_Q) = \Gamma_{\theta 2} h(1+\alpha) \quad (29)$$

Using Eq. 29 and Eq. 18 in Eq. 26, one obtains

$$\langle X_Q \rangle = (\Delta Q)^2 w_{eo}(1+\alpha)S(1+6^{-1})/(h_0 R) \quad (30)$$

Note that the first term in Eq. 26 (which was proportional to $\overline{wq_0}$) is six times as large as the second term (WL obtain 15/2 for this ratio because they use two separate formulae for w_{eo} which differ by a factor of 4/5, i.e. $6*5/4 = 15/2$).

The development for temperature is parallel until the θ_v equation analagous to Eq. 26 is reached. Since $\overline{w\theta_{v0}} = 0$, the final result is

$$\langle X_2 \rangle = (\Delta\theta_v)^2(1+\alpha)w_{eo} S/(6Rh_0) \quad (31a)$$

$$\langle X_Q \rangle = 7(\Delta Q)^2(1+\alpha)w_{eo} S/(6Rh_0) \quad (31b)$$

C. Structure Functions

The final step in this process is to specify that $\langle \theta \rangle$ is one

half the value typically found at z_i under convective conditions

$$\langle \epsilon \rangle^{1/3} = (0.2)^{1/3} w_* z_i^{-1/3} \quad (32)$$

Assuming the "quasi-steady" entrainment rate, the structure functions become

$$\langle C_Q^2 \rangle = 3.9 (\Delta Q)^2 \theta_{v*} / (z_i^{2/3} \Delta \theta_v) \quad (33a)$$

$$\langle C_{Tv}^2 \rangle = 0.5 \Delta \theta_v \theta_{v*} / z_i^{2/3} \quad (33b)$$

where $\theta_{v*} = \overline{w\theta}_{vs} / w_*$. The virtual temperature structure function is related to the temperature structure function, C_T^2 , by

$$\langle C_T^2 \rangle = 2 T_i \langle C_{Tv}^2 \rangle / \Delta \theta_v \quad (34)$$

where T_i is the function given by WL.

One point worth more discussion is the approximation $F_Q = (6R)^{-1}$ and the final forms of Eq. 31. Suppose the results of Eq. 19 were used and a different function defined

$$\langle \chi_Q \rangle = (\Delta Q)^2 w_{e0} (1+\alpha) S G_Q / h_0 \quad (35a)$$

$$\langle \chi_g \rangle = (\Delta \theta_v)^2 w_{e0} (1+\alpha) S F_Q / h_0 \quad (35b)$$

where F_Q remains as per Eq. 19 but

$$G_Q = (1 + \alpha - \alpha Z_Q) / (\alpha (1 + \alpha) S) \quad (36)$$

Using Eq. 29 one can show

$$F_Q = G_Q - 2Y_Q/R \quad (37)$$

Following the calculations WL have in their Appendix A, α , F_Q and G_Q are unique function of R/S (providing the mixed layer gradient is zero). G_Q is considerably less variable than F_Q . The following formula are reasonable approximations for $0.1 < R/S < 10$

$$\alpha = 0.96 R/S - 0.11 (R/S)^{1.5} \quad (38a)$$

$$G_Q = (1 + 0.064 \sqrt{R/S}) R^{-1} \quad (38b)$$

$$F_Q = (1 + 0.28 \sqrt{R/S}) R^{-1/6} \quad (38c)$$

These formulae lead to slight modifications to the structure function equations

$$\langle C_Q^2 \rangle = 3.3 (\Delta Q)^2 \epsilon_{\gamma}^* (Z_i^2 / 3 \Delta \theta_{\gamma}) \quad (39a)$$

$$\langle C_T^2 \rangle = 0.57 (\Delta \theta_{\gamma}) \epsilon_{\gamma}^* D_T / Z_i^2 \quad (39b)$$

where $D_T = 1 + 0.22 \sqrt{R/S}$.

The equations for C_Q^2 and C_T^2 can be written in various general forms (now dropping the bracket notation)

$$C_X^2 / ((\Delta X)^2 D_X E_X) = 1.14 \theta_{v*} / (\Delta \theta_v Z_i^{2/3}) \quad (40)$$

or, without substituting explicitly for W_{e0} and ε

$$C_X^2 / ((\Delta X)^2 D_X E_X) = \frac{0.53(1+\alpha) \Gamma_\theta W_{e0}}{\Delta \theta_v \langle \varepsilon \rangle^{1/3}} \quad (41)$$

where $D_Q = 1$, $E_Q = 3$, and

$$E_T = T_i / \Delta \theta_v \quad (42)$$

D. Discussion

It is of interest to ponder the significance of the various "quasi-steady" assumptions (Eq. 11, 12, 13). Suppose we exhume the original conservation equation integrals from Deardorff's (1979) paper (his Eq. 18 and 21). Assuming only horizontal homogeneity and constant divergence, the general equations become

$$\Delta h \, dQ_0/dt + \Delta h Y_Q \, d\Delta Q/dt - \Delta Q [(1 - Y_Q) W_{e2} + Y_Q W_{e0}] = \overline{wq_0} \quad (43a)$$

$$\Delta h \, d\theta_{v0}/dt + \Delta h Y_Q \, d\Delta \theta_v/dt - \Delta \theta_v [(1 - Y_Q) W_{e2} + Y_Q W_{e0}] = 0 \quad (43b)$$

Thus Eq 16 and the θ_v analogue can be reproduced by requiring

$$W_{e2} = (1 + \alpha) W_{e0} \quad (44a)$$

$$d\Delta Q/dt = d\Delta\theta_v/dt = 0 \quad (44b)$$

It is not necessary to require $W_e = -W$, $dh_0/dt = dh_2/dt = d\Delta h/dt = 0$. This explains why WL found excellent agreement with Aschurch data where $W = 0$ and $W_{e0} \approx 10$ cm/s.

Similarly, the general forms for the dissipation integrals are

$$\begin{aligned} -\langle P_Q \rangle \Delta h &= -2\Delta h \Delta Q Y_Q dQ_0/dt - 2\Delta h Z_Q \Delta Q d\Delta Q/dt \\ &\quad + (\Delta Q)^2 [(1 - Z_Q) W_{e2} + Z_Q W_{e0}] \end{aligned} \quad (45a)$$

$$\begin{aligned} -\langle P_\theta \rangle \Delta h &= 2\Delta h \Delta\theta_v (Y_Q^2 - Z_Q) d\Delta\theta_v/dt \\ &\quad + (\Delta\theta_v)^2 [-2Y_Q [(1 - Y_Q) W_{e2} + Y_Q W_{e0}] \\ &\quad + (1 - Z_Q) W_{e2} + Z_Q W_{e0}] \end{aligned} \quad (45b)$$

which reduce to Eq 14 if the conditions of Eq 44 are met.

Since entrainment and surface flux tend to counteract each other in the Q case, it seems quite reasonable to assume that the $d\Delta Q/dt$ and dQ_0/dt terms are negligible in Eq 45a

$$-\langle P_Q \rangle \Delta h = (\Delta Q)^2 [(1 - Z_Q) W_{e2} + Z_Q W_{e0}] \quad (46)$$

Instead of making the assumption Eq 44a, suppose we simply assume

$$W_{e2} = W_{e0} = \alpha \overline{w\theta}_{vs} / \Delta\theta_v \quad (47)$$

which is the standard cloud-free result from Lilly (1968) where typically $\alpha = 0.2$. Then one can easily show that

$$\langle C_Q^2 \rangle = 3.3 (\Delta Q)^2 \theta_{v*} / (z_1^{2/3} \Delta\theta_v) \quad (48)$$

which is identical to the WL result as expressed in Eq. 39a! In other words, the combination of "quasi-steady" assumptions $W_{e2} = (1 + \alpha)W_{e0}$ and $W_{e2} = \overline{w\theta}_{vs} / (\Gamma_\theta h_0)$ are equivalent to the assumptions of Eq. 47 even though they may imply vastly different entrainment rates.

If one uses the assumptions of Eq. 47 and parallels the WL development, then the equivalent to Eq. 18 is

$$\overline{wq}_0 = - \Delta Q W_{e0} \quad (49)$$

and the equilibrium condition from the θ_v equation is

$$\overline{w\theta}_{v0} = W_{e0} (\alpha h_0 \Gamma_\theta - \Delta\theta_v) \quad (50)$$

which, assuming $\overline{w\theta}_{v0} = 0$, gives

$$\alpha = R/S \quad (51)$$

The results for θ_v are also interesting because it is not clear that the $d\Delta\theta_v/dt$ term should be negligible compared to the

other terms in Eq 46 b. Suppose we let

$$-\langle P_\theta \rangle \Delta h = A + B \quad (52)$$

Then the $d\Delta\theta_v/dt$ term is small if A/B is small (returning to the "quasi-steady" format)

$$A/B = \frac{h_0(Y_Q^2 - Z_Q) d\Delta\theta_v/dt}{\Delta\theta_v (1 + \alpha) W_{e0}} \quad (53)$$

Since $Y_Q^2 - Z_Q \approx -0.1$, we can write

$$A/B = \frac{-0.6 h_0(R/S) d\Delta\theta_v/dt}{(1 + \alpha) W_{e0} \Delta\theta_v} \quad (54)$$

The magnitude of A/B can be examined by using the general relation

$$d\Delta\theta_v/dt = -d\theta_0/dt + \Gamma_\theta W_{e2} \quad (55)$$

and writing a simple entrainment formula (e.g. "quasi-steady")

$$W_{e2} = \overline{w_{\theta vs}} (\Gamma_\theta h_0) \quad (56)$$

The integral of the conservation equation from $Z = 0$ to $Z = h_0$ gives

$$h_0 \, d\theta_{v0}/dt = \overline{w\theta}_{vs} + w_{e0}\Delta\theta_v \quad (57)$$

therefore

$$d\Delta\theta_v / dt = - w_{e0} \Delta\theta_v / h_0 \quad (58)$$

using Eq. 54 we find

$$A/B = \frac{0.6}{(1+\alpha)} R/S \quad (59)$$

A good example is the Aschurch data quoted by WL where Eq. 57 was shown to be applicable. Since $R/S = 0.3$ for that data, $A/B = 0.15$ and $d\Delta\theta_v/dt$ is negligible.

Certainly the conditions set by WL are consistent with neglecting $d\Delta\theta_v/dt$. It is not clear how to identify conditions where this assumption is invalid. Eq. 54 cannot provide much guidance because it is based on solutions to Eq. 28 with $d\Delta\theta_v/dt = 0$. It is interesting that in the conditions where the WL equations for "quasi-steady" entrainment are expected to breakdown ($\Delta\theta_v$ large, $R/S > 1$) then the Lilly type relations give the same results for C_Q^2 . If the $d\Delta\theta_v/dt$ term becomes important, then one anticipates the WL formulation will underestimate C_T^2 .

III ATMOSPHERIC DATA

A. Measurement Techniques

The measurements were made using a single engine Bellanca Viking aircraft operated by Airborne Research Associates of Weston, MA. The instrumentation and data processing have been previously described in detail (Fairall et. al., 1980; Schacher et. al., 1980) so only a brief summary is given here.

- i) Mean temperature, T : platinum resistance sensor with standard aircraft mount.
- ii) Mean humidity, Q : cooled mirror dew cell.
- iii) Mean windspeed, U : estimated at the surface from the sea state and DMV navigational aid. The present LORAN system was not available.
- iv) Sea surface temperature, T_s : Barnes PRT-5 IR radiometer.
- v) C_T^2 : microthermal sensors (4.5 μ m dia. tungsten) in the paired configuration.
- vi) C_Q^2 : Lyman-alpha fast humidimeters using the inertial subrange filter method. Absolute calibration based on comparison with a microwave refractometer.
- vii) ϵ : hot wire (4.5 μ m dia. tungsten) constant temperature anemometer. The inertial subrange filter method was used.

B. Surface Fluxes and Turbulence Scaling Parameters

Surface fluxes were evaluated from aircraft measurements using two methods: a) bulk aerodynamic and b) dissipation (inertial subrange). The fluxes are defined in terms of the

following scaling parameters:

$$\text{momentum:} \quad \overline{\rho u w}_s = -\rho u_*^2 \quad (60a)$$

$$\text{sensible heat:} \quad \rho C_p \overline{w \theta}_s = -\rho C_p u_* T_* \quad (60b)$$

$$\text{moisture:} \quad \overline{\rho q w}_s = -\rho u_* q_* \quad (60c)$$

The momentum flux is also referred to as the Reynolds stress, τ .

Note: the bulk method was not used overland.

1. Bulk aerodynamic method.

The exact details were described in a recent paper (Davidson et al, 1981). Using Eq. 4a from that paper, one can relate the values of some meteorological variable (temperature, moisture or wind speed) at the sea surface, X_s , and at some height Z in the surface layer, X_z , to the scaling parameter, X_* :

$$u_* = u_z k [\ln (Z/Z_0) - \psi_u (Z/L)]^{-1} \quad (61a)$$

$$T_* = (T_z - T_s) \beta k [\ln (Z/Z_{0T}) - \psi_T (Z/L)]^{-1} \quad (61b)$$

$$q_* = (q_z - q_s) \beta k [\ln (Z/Z_{0T}) - \psi_T (Z/L)]^{-1} \quad (61c)$$

where Z_0 and Z_{0T} are roughness lengths, L is the Monin-Obukhov length, β and k are constants, and ψ_u and ψ_T are empirical functions.

2. Dissipation method.

The dissipation method relies on semi-empirical relationships of inertial subrange turbulence to surface-layer scaling parameters (Fairall et al., 1980). The equations are

$$u_* = [(\epsilon k z)/\phi(z/L)]^{1/3} \quad (62a)$$

$$T_* = [z^{2/3} C_T^2/f(z/L)]^{1/2} \quad (62b)$$

$$Q_* = [z^{2/3} C_Q^2/(A f(z/L))]^{1/2} \quad (62c)$$

where ϵ is the dissipation rate, ϕ and f are empirical functions, and A is a constant. Because the structure-function parameters C_T^2 and C_Q^2 are related to the square of the scaling parameter, a sign ambiguity exists. This can usually be eliminated by examining the low-level height dependence of ϵ , C_Q^2 and C_T^2 because the functions ϕ and f have characteristic profiles for stable and unstable conditions.

Both methods yield accuracies on the order of 10% for u_* , $\pm 0.02^\circ\text{C}$ for T_* and $\pm 0.02 \text{ g/m}^3$ for Q_* (note: $q_* = Q_*/\rho$).

C. Data Sets

The data given in this report were obtained in four field programs:

i) Panama City (PC), 1978 (more detail available in Fairall, 1979) over the Gulf of Mexico in Florida.

ii) White Sands (WS), 1979. Two profiles over the desert under highly convective daytime conditions.

iii) MAGAT (MG), 1980 (more detail available in Fairall, 1980) in the Monterey Bay area.

iv) Bahamas (BH), 1980. A series of profiles taken near Andros Island in the late fall.

The complete data sets were examined to remove profiles that encountered boundary-layer clouds. A total of 23 profiles were selected. Graphs of the mean and turbulence profiles for each case are given in Appendix A. A summary of the basic scaling parameters is given in Table 1.

TABLE 1.

Meteorological data and surface scaling parameters
from the cloud free NPS data sets.

#	Site	Date	Time	u_*	T_*	q_*	Z_i	$\Delta\theta_v$	ΔQ	α	Γ_a
				ms^{-1}	K	gkg^{-1}	km	K	gm^{-3}		Kkm^{-1}
1	PC	11/26	1252	.40	-.082	-.16	.85	1	-6.5	.4	5.5
2	PC	11/26	1436	.23	-.095	-.16	.90	.5	-2.3	.1	5.3
3	PC	12/2	1405	.24	-.14	-.18	.23	4	-.5	.7	4.6
4	PC	12/10	1324	.38	-.35	0	.91	6	-1	.35	10
5	PC	12/10	1410	.32	-.49	-.49	.75	.3	-1	.15	11
6	PC	12/10	1523	.34	-.48	-.48	.85	3	-1.3	.25	11
7	PC	12/10	1637	.34	-.49	-.50	1.1	3	-3	.1	17.5
8	PC	12/11	1021	.28	-.44	-.43	.7	3	-1	.5	9.5
9	PC	12/13	1154	.19	0.21	-.47	.6	1.5	.2	.35	10
10	PC	12/13	1459	.17	-.20	-.42	.5	.5	-2	.4	11
11	WS	10/17	1330	.47	-.42	0	1.1	1.5	-2.5	.1	3.0
12	WS	10/18	1330	.47	-.42	0	1.9	1.5	-2.5	.1	3.3
13	MG	4/30	1610	.28	-.078	-.11	.36	6.5	-4.5	.35	9
14	MG	5/4	1024	.21	-.085	-.11	.36	11	-5.2	.4	10
15	MG	5/4	1201	.30	-.075	-.12	.46	9	-5.2	.5	15
16	MG	5/4	1244	.30	-.075	-.12	.54	9	-5	.2	15
17	MG	5/7	1043	.41	-.04	-.05	.23	7	-2	.5	9
18	BH	12/12	1414	.15	-.16	-.27	.5	1	-2.5	?	5
19	BH	12/13	1540	.33	-.30	-.39	.65	0	0	?	4.8
20	BH	12/14	1330	.23	-.17	-.27	.90	2.5	-8.5	.15	6.3
21	BH	12/15	1333	.20	-.16	-.26	1.5	3.5	-9	.15	5.5
22	BH	12/15	1347	.20	-.16	-.26	1.5	3.5	-9	.3	5.5
23	BH	12/15	1637	.14	-.14	-.25	1.1	1	-4.5	.4	6.3

IV. RESULTS

A summary of the secondary scaling parameters used for the NPS data set is given in Table 2. Also shown in Table 2 is a comparison of the measured and model assumed values for ϵ at the inversion. With very few exceptions, the model assumption (Eq. 32) is very good. The entrainment velocities calculated from the "quasi-steady" assumption used by WL (Eq. 20) and the more conventional parameterization of Lilly (1968).

$$W_{e0}/W_* = 0.2 \theta_{v*}/\Delta\theta_v \quad (63)$$

are also calculated.

In Table 3 are the measured values of C_T^2 and C_Q^2 at the inversion plus their normalized forms

$$I_X = z_i^{2/3} C_X^2 / ((\Delta X)^2 D_X F_X) \quad (64)$$

taken from Eq. 40. According to WL (Eq. 26), the theoretical value is

$$I_C = 1.14 \theta_{v*}/\Delta\theta_v \quad (65)$$

which is the same for T and Q.

A direct comparison of measured and calculated values of C_T^2 and C_Q^2 is given in Fig. 2. The model predicts the measurements within a factor of three. The uncertainty is slightly greater than the factor of two suggested by WL but

Table 2.

Surface scaling ($\overline{w\theta}_{vs}$ and L), convective scaling (W_* , θ_{v*} and ϵ_i) and inversion scaling (R , S and W_{eo}) parameters. Two formulae are used to estimate W_{eo} : "steady" is Eq 20 and "Lilly" is Eq 64.

#	$\overline{w\theta}_{vs}$	L	W_*	R	S	R/S	$\langle \epsilon_i \rangle^{1/3}$		W_{eo}		θ_{v*}
	Kms^{-1}	m	ms^{-1}				$\text{m}^{2/3} \text{s}^{-1}$		cm s^{-1}		K
							meas	calc	Steady	Lilly	
1	.044	-125	1.1	33	103	.32	.063	.066	.81	.88	.04
2	.028	- 50	.93	16	160	.1	.096	.052	.65	1.1	.03
3	.040	- 29	.67	67	18	3.7	.10	.063	2.7	.2	.06
4	.13	- 34	1.6	70	105	.67	.074	.095	1.3	.43	.081
5	.19	- 15	1.7	25	70	.36	.073	.11	2.4	1.3	.11
6	.19	- 17	1.7	29	90	.32	.084	.11	2.0	1.3	.11
7	.20	- 16	1.9	30	190	.16	.071	.11	1.2	1.3	.11
8	.14	- 24	1.5	30	65	.46	.11	.096	1.7	.93	.093
9	.056	- 10	1.0	29	82	.35	.063	.072	.8	.74	.056
10	.048	- 9	.92	10	105	.10	.10	.069	.75	1.9	.053
11	.20	- 45	1.9	14	32	.44	.11	.11	6.6	2.7	.11
12	.20	- 45	2.3	17	71	.24	.11	.11	3.4	2.7	.087
13	.027	- 70	.65	110	77	2.2	.13	.056	.84	.08	.042
14	.022	- 38	.6	110	84	3.7	.046	.053	.59	.04	.037
15	.02	-120	.7	250	170	1.5	.087	.051	.39	.04	.029
16	.02	-120	.75	280	170	1.6	.046	.051	.24	.04	.027
17	.02	-300	.5	200	54	3.7	.063	.051	.89	.06	.04
18	.03	-9.5	.79	26	63	.4	.040	.059	.96	.6	.038
19	.12	- 27	1.37	0	36	0	.10	.093	3.1		.088
20	.049	- 22	1.12	60	134	.45	.084	.072	.9	.4	.044
21	.039	- 17	1.24	110	265	.42	.053	.063	.43	.22	.032
22	.039	- 17	1.24	110	265	.42	.11	.063	.45	.22	.032
23	.024	- 10	.95	40	280	.14	.048	.063	.3	.42	.025

Table 3.

Measured values of the interfacial structure functions (C_T^2 and C_Q^2) and their resultant values for

$I_X = z_i^{2/3} C_X^2 / ((\Delta X)^2 D_X F_X)$ where $X=T$ or Q These are compared with theoretical values, I_c , using the "steady" and "Lilly" entrainment values.

	$\langle C_T^2 \rangle$	$\langle C_Q^2 \rangle$	D_T	E_T	I_T	I_Q	I_c (Theory)		I_T/I_c	I_Q/I_c
	$K^2 m^{-2/3}$	$(q m^{-3})^2 m^{-2/3}$					Steady	Lilly		
	MEAS	10								
	.3		1.12	8.1	.003		.048	.048	.065	
	5.6		1.07	5.1	.396		.068	.11	5.7	
	5		1.42	.58	.014		.017	.0013	.82	
	12		1.18	.61	.044		.015	.005	2.9	
	11		1.13	.73	.135		.042	.0023	3.1	
	5.7		1.12	.80	.064		.042	.027	1.5	
	9		1.09	1.23	.079		.042	.046	1.9	
	43		1.15	.73	.45		.035	.019	13	
	6.1		1.13	1.5	.12		.043	.040	2.8	
	3.4		1.07	4.4	.18		.12	.30	1.5	
	9.2		1.15	1.8	.22		.084	.034	2.6	
	3		1.11	1.8	.10		.066	.052	1.5	
	2.5	3.9	1.33	1	.0023	.0033	.0074	.0007	.31	.45
	1.3	2	1.42	.83	.0005	.0012	.0038	.0003	.13	.33
	10	9.8	1.27	.90	.0063	.0072	.0037	.0005	1.7	1.9
	2.8	25	1.29	.89	.0020	.022	.0035	.0006	.57	6.3
	1.7	1.6	1.42	.69	.0013	.0050	.0065	.0004	.20	.77
	6.8	33	1.14	2.6	.15	.11	.042	.026	3.6	2.6
	.6	3.3	1							
	2.7	16	1.16	3.6	.0093	.0069	.020	.009	.47	.35
		70	1.15	2.7		.038	.010	.0042		3.8
		16	1.15	2.7		.0087	.010	.0042		.87
		55	1.08	5.0		.097	.029	.0046		3.3

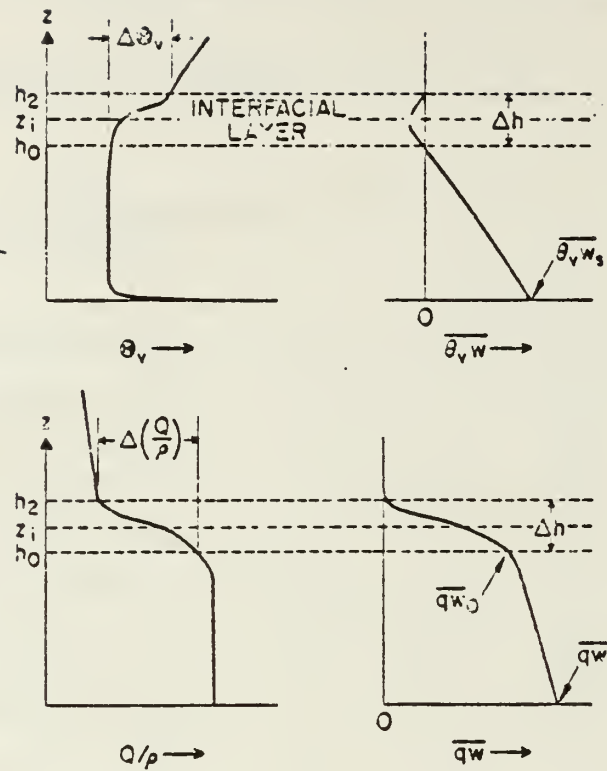
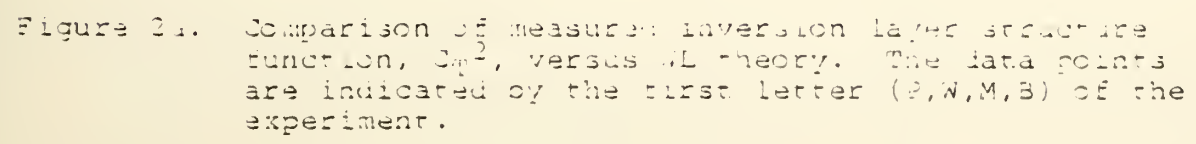


Figure 1. Schematic representation of the convective boundary layer (taken from Wyngaard and LeMone, 1980) with its interfacial layer showing h_0 , z_i , h_2 , Δh , fluxes and jumps. Note that $\Delta\theta_v = \theta_v(h_2) - \theta_v(h_0)$ is positive while ΔQ is negative.



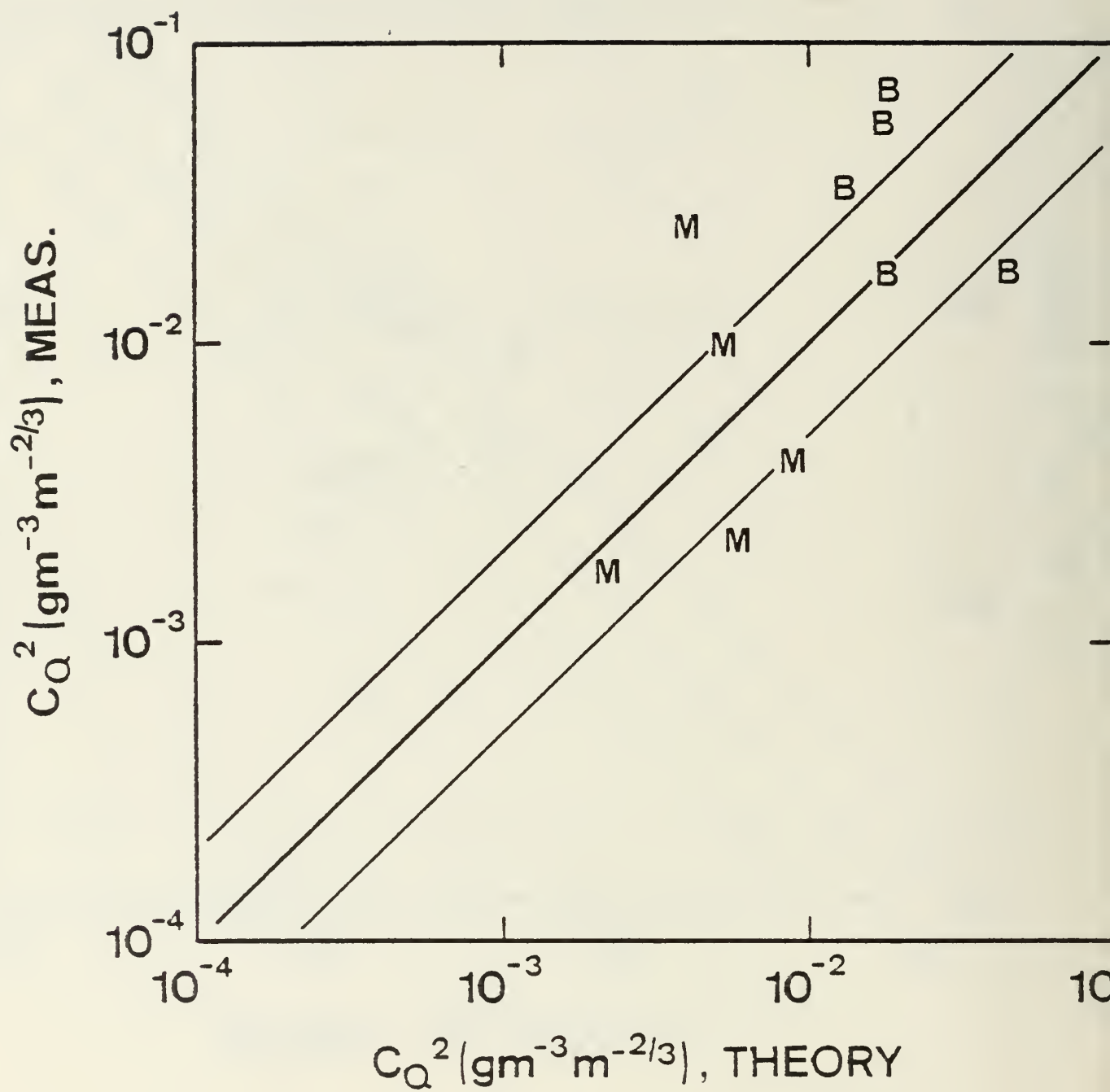


Figure 1b. Similar to Fig. 1a but for C_Q^2 .

includes various measurement errors and uncertainties. Note that the C_Q^2 data has a greater range of values than C_T^2 . This is consistent with the WL model. If we examine the function

$$H = Z_i^{2/3} C_X^2 / (D_X \theta_{v*}) \quad (66)$$

then

$$H_T = F_T \Delta \theta_v \quad (67a)$$

$$H_Q = (\Delta Q)^2 / \Delta \theta_v \quad (67b)$$

A graph of H_T and H_Q is shown in Fig. 3 for a typical range of $\Delta \theta_v$ and ΔQ from the NPS data set. Note that H_T varies roughly from 2 to 9 while H_Q varies from 4 to 72.

The entrainment parameterization was tested (Fig. 4) by plotting measured values of I_X (Eq. 65) against the model value (Eq. 66) which is based on the entrainment formula given by WL (Eq. 26). This plot gives a much higher correlation than a similar graph (not shown) using the more traditional formula due to Lilly (1968), Eq. 62, which gives

$$I_C' \text{ (Lilly)} = 0.18 (1+\alpha) \Gamma_0 Z_i \theta_{v*} / (\Delta \theta_v)^2 \quad (68)$$

This is not really significant because, when used in proper combination with Eq. 48, the Lilly formulation also leads to Eq. 66.

In order to look for systematic errors, the ratios (R_T and R_Q) of measured to model values of C_T^2 and C_Q^2 were calculated and plotted against $\Delta \theta_v$ (Fig. 5). A simple

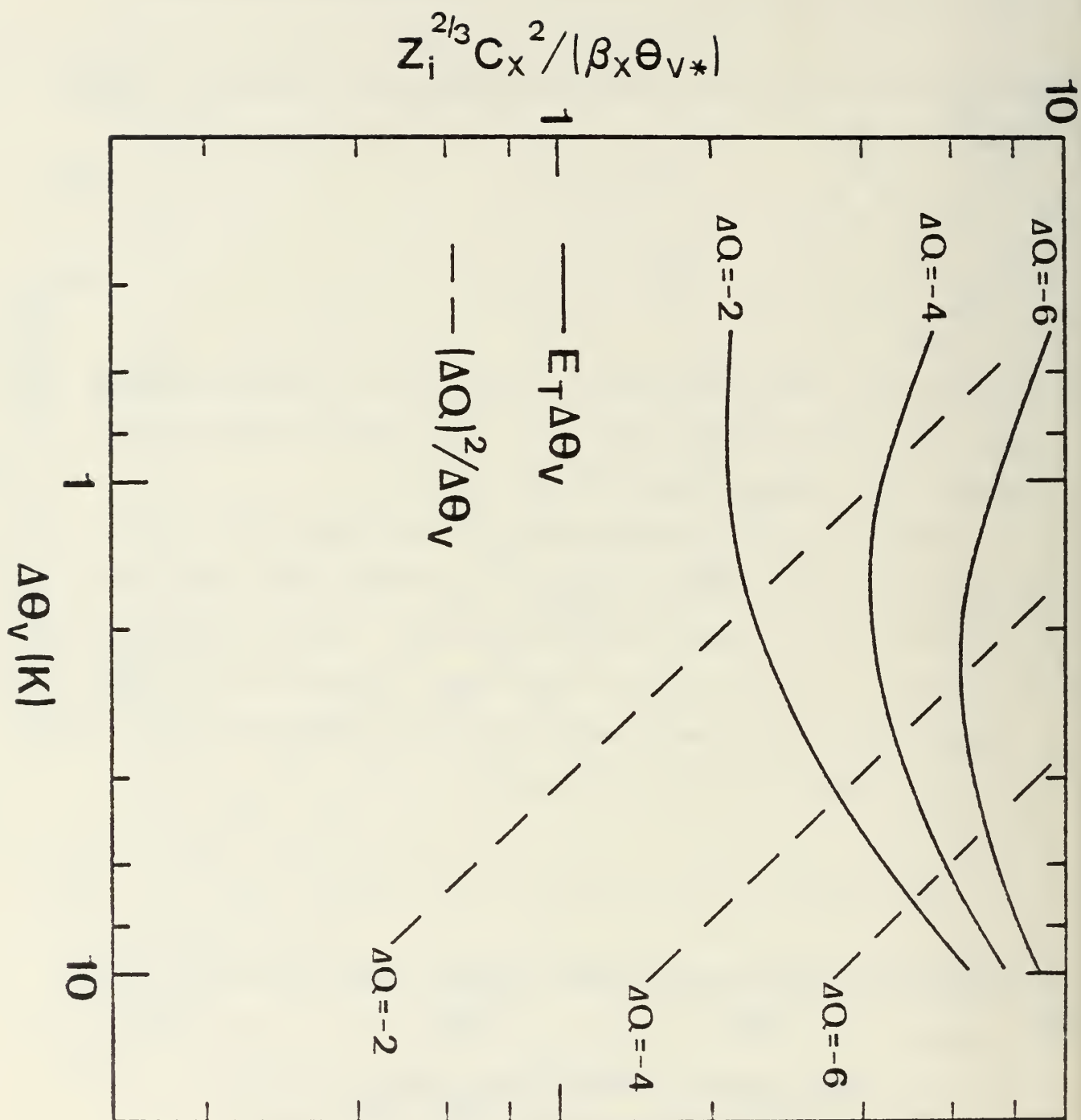


Figure 3. Theoretical expression for H_0 and H_1 (Eq. 9c) illustrating the difference between the dependence of C_T^2 and C_Q^2 on $\Delta \Theta_V$ and ΔQ .

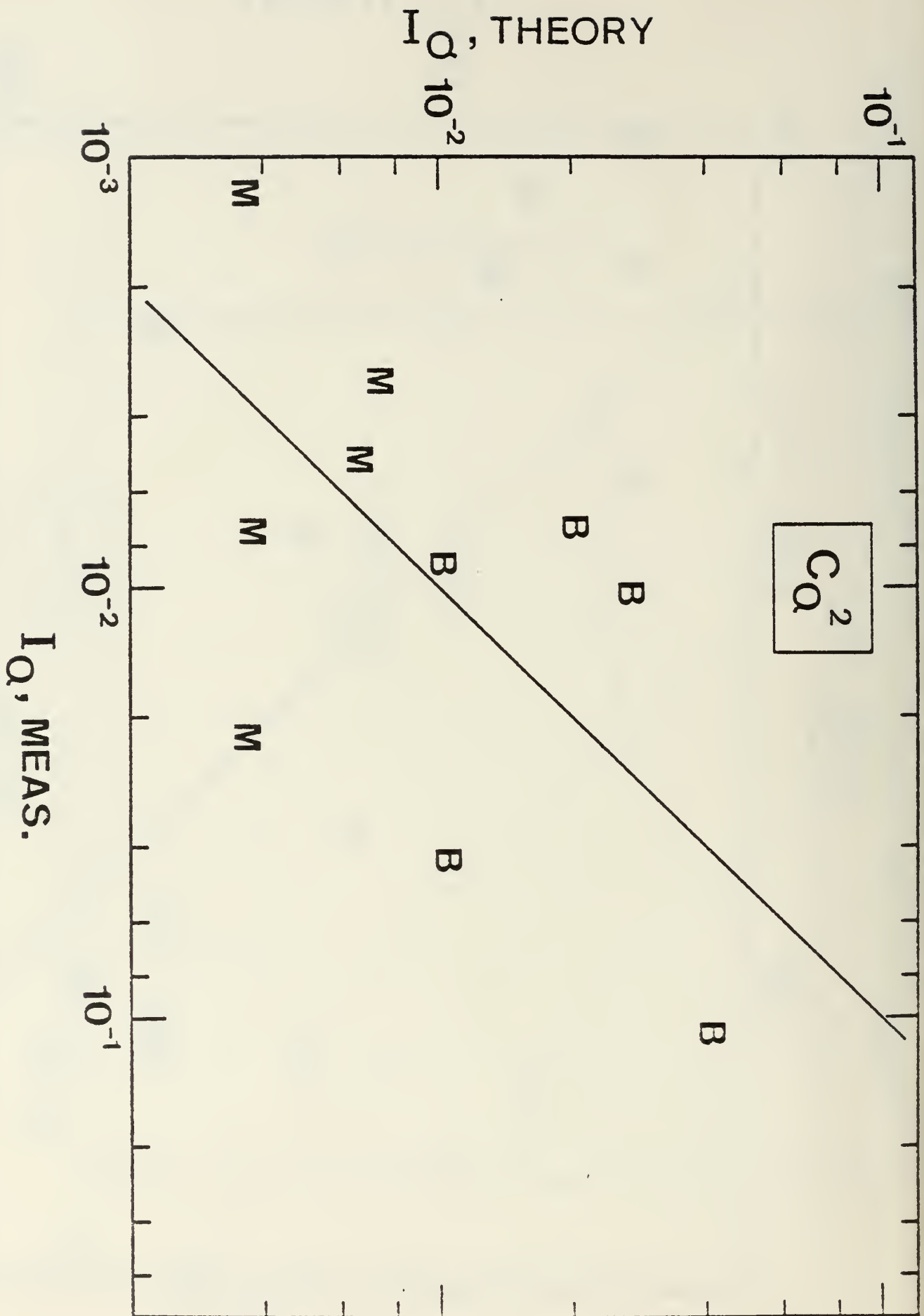


Figure 4b. Similar to Fig. 4a but for C_Q^2 .

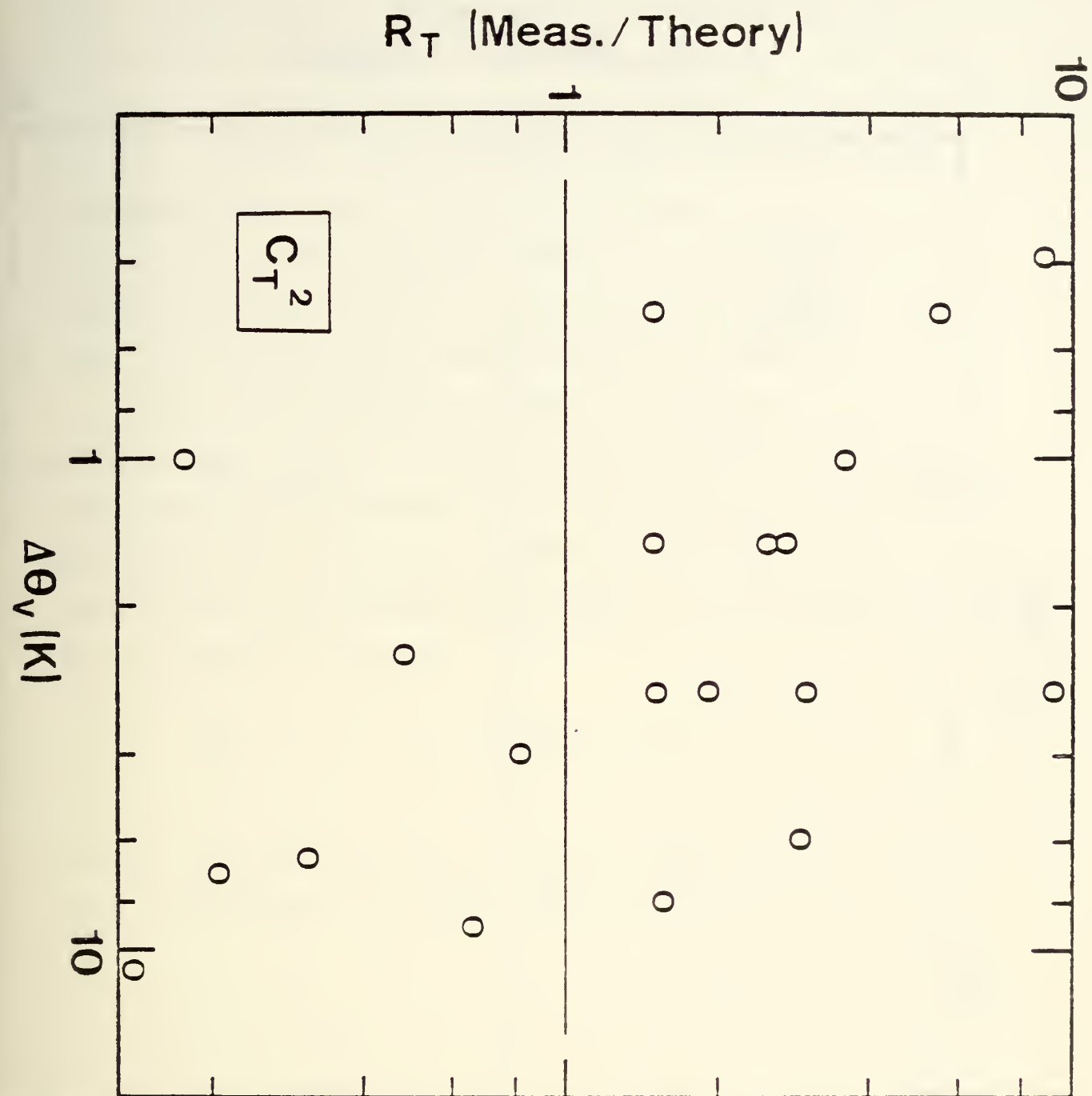


Figure 5a. The measured value of C_T^2 divided by the WL model value as a function of $\Delta\theta_v$.

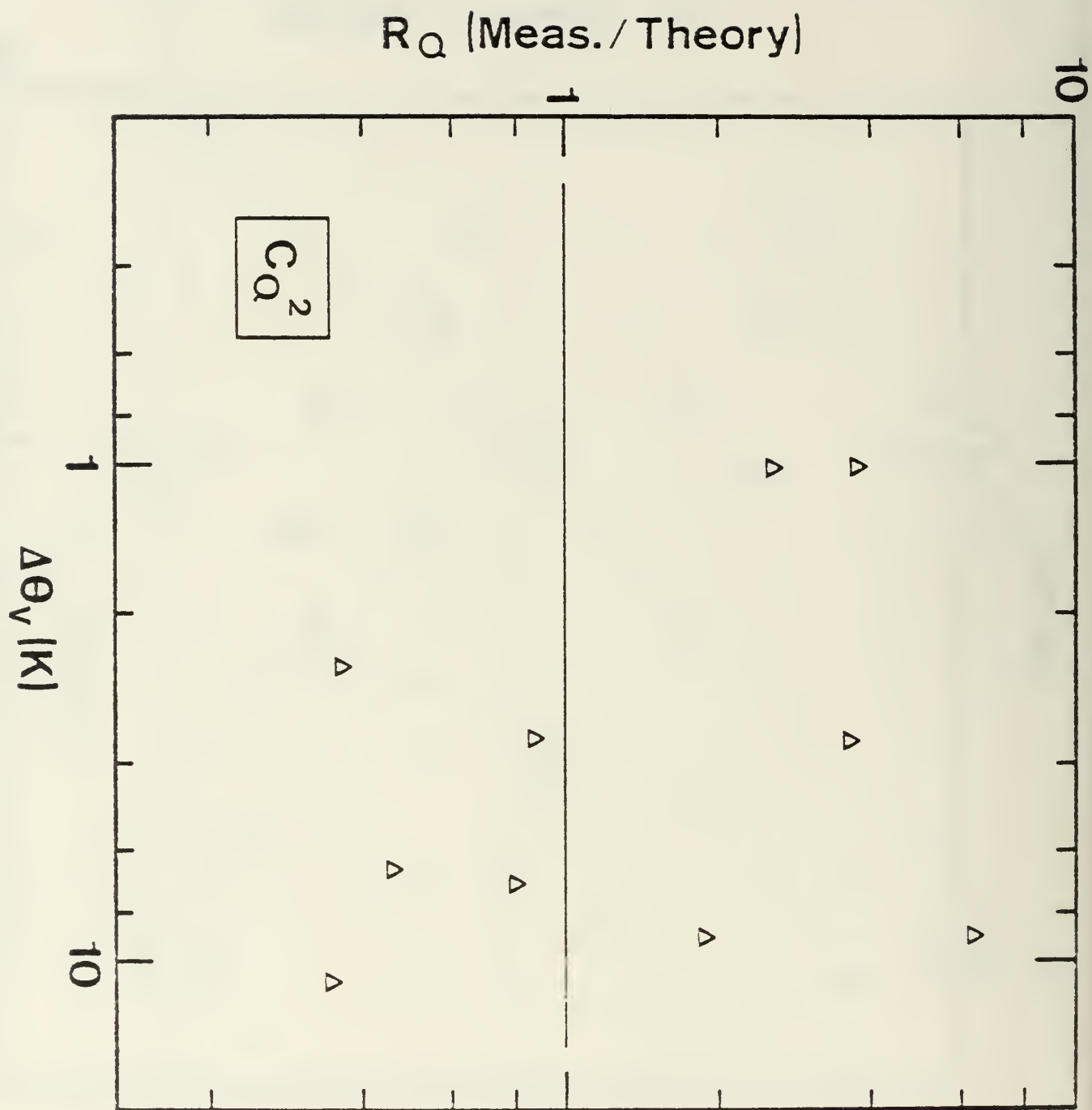


Figure 3b. Similar to Fig. 3a but for C_Q^2 .

log-average yields $R_T = 1.15$ and $R_Q = 1.3$. Figure 5a weakly suggests that the model underestimates C_T^2 (large R_T) when $\Delta\theta_v$ is small while it overestimates when $\Delta\theta_v$ is large (the C_Q^2 data is too sparse to clear up this question). This could be due to an error in the estimation of $\Delta\theta_v$ and ΔQ (admittedly rather subjective). An examination of Fig. 3 suggests that a reasonable adjustment of $\Delta\theta_v$ (several tenths K) will not move the data points substantially closer to the $R_T = 1$ midline. Another possibility is that Eq. 20 tends to overestimate W_{e0} when $\Delta\theta_v$ is large while underestimating for small $\Delta\theta_v$.

Given the considerable scatter in the results, the uncertainties in the estimation of $\Delta\theta_v$ and ΔQ from measured profiles and the insensitivity of C_T^2 to $\Delta\theta_v$ and ΔQ it is suggested that a simplified formula for C_T^2 can be used for application to radiosonde quality data. If one assumes (based in Fig. 3) that $H_T \approx 5$, then

$$C_T^2 \approx 5 \theta_{v*} Z_i^{-2/3} \quad (69)$$

Based on the NPS data set this approximation appears to be at least as accurate as the more complicated formula (Fig. 6).

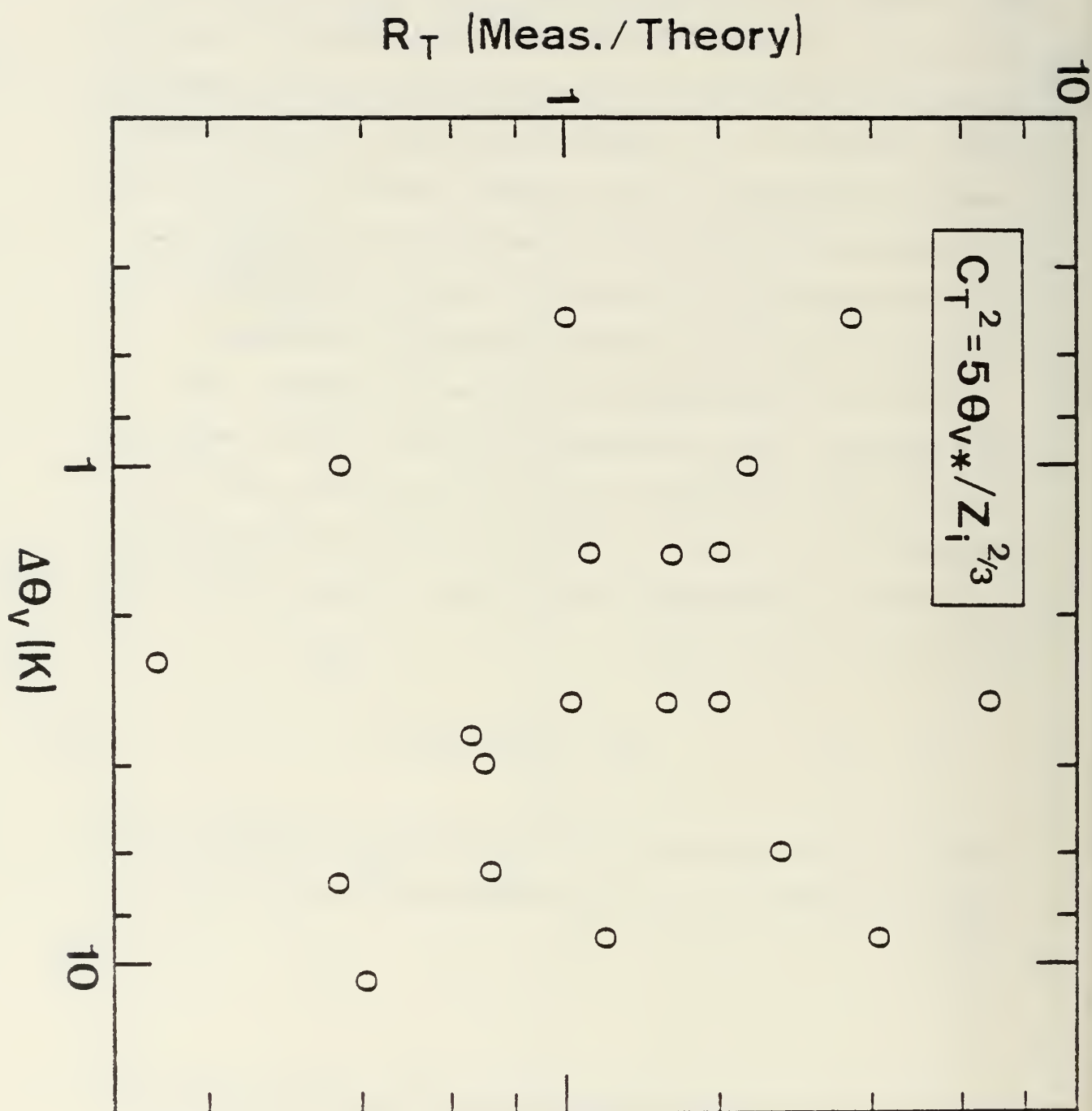


Figure 6. The measured value of C_T^2 divided by the model value using the simplified expression (Eq. 70).

V CONCLUSIONS

The Wyngaard-LeMone inversion layer scaling has been examined theoretically and tested against a data set obtained by NPS investigators in cooperation with Airborne Research Associates.

The theoretical examination indicated the following:

- i) The WL theory is more general than is implied by the strict assumptions of the "quasi-steady" theory.
- ii) The WL development can be simplified slightly, leading to modest adjustments of the normalization constants.
- iii) The steady state assumption that $d\Delta Q/dt$ is negligible is reasonable under most conditions. The assumption that $d\Delta\theta_v/dt$ is negligible may not be justified when $R/S > 1$.

The examination of the atmospheric data indicated the following:

- i) The assumption that ϵ at the inversion is proportional to a fixed fraction of the surface buoyancy flux was quite reasonable.
- ii) The WL model predicted the measured value of C_T^2 and C_Q^2 to within a factor of three.
- iii) Some evidence, though statistically weak, was found to suggest the model overestimates the structure functions for large $\Delta\theta_v$ ($> 3K$) while it underestimates for small $\Delta\theta_v$ ($< 2K$). On the other hand, this could be a manifestation of the Stein effect for comparison of data sets subject to error where small values are usually overestimated and large quantities are usually underestimated.

Based on these results, it is obvious that a major weakness of the model is its reliance on an entrainment formulation that is too restrictive. The two extremes of the buoyancy jump ($\Delta\theta_v$) may involve different entrainment regimes (e.g. encroachment, convective instability or the Lilly formulation). It would also be useful to include the effect of inversion windshear on W_e and on the structure functions. Another area of investigation might be stable surface layers. These may be very important for surface optical propagation because C_T^2 values are often sizeable and z_i is usually small (on the order of 100m).

ACKNOWLEDGEMENTS

The author wishes to recognize the efforts and cooperation of Ralph Markson and Jan Sedlacek of Airborne Research Associates and John Willett of NRL. The aircraft work was supported by the Naval Air Systems Command (AIR 370). This report was funded by NEPRF for the High Energy Laser Program.

REFERENCES

1. Davidson, K.L., G.E. Schacher, C.W. Fairall and A.K. Goroch, 1981: "Verification of the bulk method of calculating overwater optical turbulence", Appl. Opt., 20, 2919 - 2923.
2. Deardorff, J.W., 1979: "Prediction of convective mixed-layer entrainment for realistic capping inversion structure", J. Atmos. Sci. 36, 424-436.
3. Fairall, C.W., 1979: "Aircraft measurements of micro-meteorological parameters at Panama City, Florida", Tech. Report BDM/M-008-79, pp. 250.
4. Fairall, C.W., R. Markson, G.E. Schacher and K.L. Davidson, 1980: "An aircraft study of turbulence dissipation and temperature structure function in the unstable marine atmospheric boundary layer", Bound.-Layer Meteor. 19, 453-469.
5. Fairall, C.W., 1980: "Atmospheric optical propagation comparisons during MAGAT-80", Tech. Report BDM/M-010-80, pp. 143.
6. Lilly, D.K., 1968: "Models of cloud-topped mixed layers under a strong inversion", Quart. J.R. Met. Soc. 94, 292-309.
7. Schacher, G.E., K.L. Davidson, C.W. Fairall and D.E. Spiel, 1980: "Naval Postgraduate School shipboard and aircraft meteorological equipment", Tech. Report NPS-61-80-017, pp. 23.
8. Wyngaard, J.C. and M.A. Lemone, 1980: "Behavior of the refractive index structure parameter in the entraining convective boundary layer," J. Atmos. Sci. 37, 1573-1585.

APPENDIX A

This appendix contains graphs of mean (θ_v , q) and turbulence (C_T^2 , C_Q^2 , ϵ) profiles for each of 23 data sets. The site designations are defined in Section III-C. The abstraction of this data to obtain the relevant parameters (Tables 1, 2, 3 in the main text) is described in Section III.

List of Figures

APPENDIX A

Figure A1a.	Mean profile for	PC 11/26 1252.
Figure A1b.	Turbulence profile for	PC 11/26 1252.
Figure A2a.	Mean profile for	PC 11/26 1436.
Figure A2b.	Turbulence profile for	PC 11/26 1436.
Figure A3a.	Mean profile for	PC 12/2 1405.
Figure A3b.	Turbulence profile for	PC 12/2 1405.
Figure A4a.	Mean profile for	PC 12/10 1324.
Figure A4b.	Turbulence profile for	PC 12/10 1324.
Figure A5a.	Mean profile for	PC 12/10 1410.
Figure A5b.	Turbulence profile for	PC 12/10 1410.
Figure A6a.	Mean profile for	PC 12/10 1523.
Figure A6b.	Turbulence profile for	PC 12/10 1523.
Figure A7a.	Mean profile for	PC 12/10 1637.
Figure A7b.	Turbulence profile for	PC 12/10 1637.
Figure A8a.	Mean profile for	PC 12/11 1021.
Figure A8b.	Turbulence profile for	PC 12/11 1021.
Figure A9a.	Mean profile for	PC 12/13 1154.
Figure A9b.	Turbulence profile for	PC 12/13 1154.
Figure A10a.	Mean profile for	PC 12/13 1459.
Figure A10b.	Turbulence profile for	PC 12/13 1459.
Figure A11a.	Mean profile for	WS 10/17 1330.
Figure A11b.	Turbulence profile for	WS 10/17 1330.
Figure A12a.	Mean profile for	WS 10/18 1330.
Figure A12b.	Turbulence profile for	WS 10/18 1330.
Figure A13a.	Mean profile for	MG 4/30 1610.

Figure A13b. Turbulence profile for MG 4/30 1610.

Figure A14a. Mean profile for MG 5/4 1024.

Figure A14b. Turbulence profile for MG 5/4 1024.

Figure A15a. Mean profile for MG 5/4 1201.

Figure A15b. Turbulence profile for MG 5/4 1201.

Figure A16a. Mean profile for MG 5/4 1244.

Figure A16b. Turbulence profile for MG 5/4 1244.

Figure A17a. Mean profile for MG 5/7 1043.

Figure A17b. Turbulence profile for MG 5/7 1043.

Figure A18a. Mean profile for BH 12/12 1414.

Figure A18b. Turbulence profile for BH 12/12 1414.

Figure A19a. Mean profile for BH 12/13 1540.

Figure A19b. Turbulence profile for BH 12/13 1540.

Figure A20a. Mean profile for BH 12/14 1330.

Figure A20b. Turbulence profile for BH 12/14 1330.

Figure A21a. Mean profile for BH 12/15 1333.

Figure A21b. Turbulence profile for BH 12/15 1333.

Figure A22a. Mean profile for BH 12/15 1347.

Figure A22b. Turbulence profile for BH 12/15 1347.

Figure A23a. Mean profile for BH 12/15 1637.

Figure A23b. Turbulence profile for BH 12/15 1637.

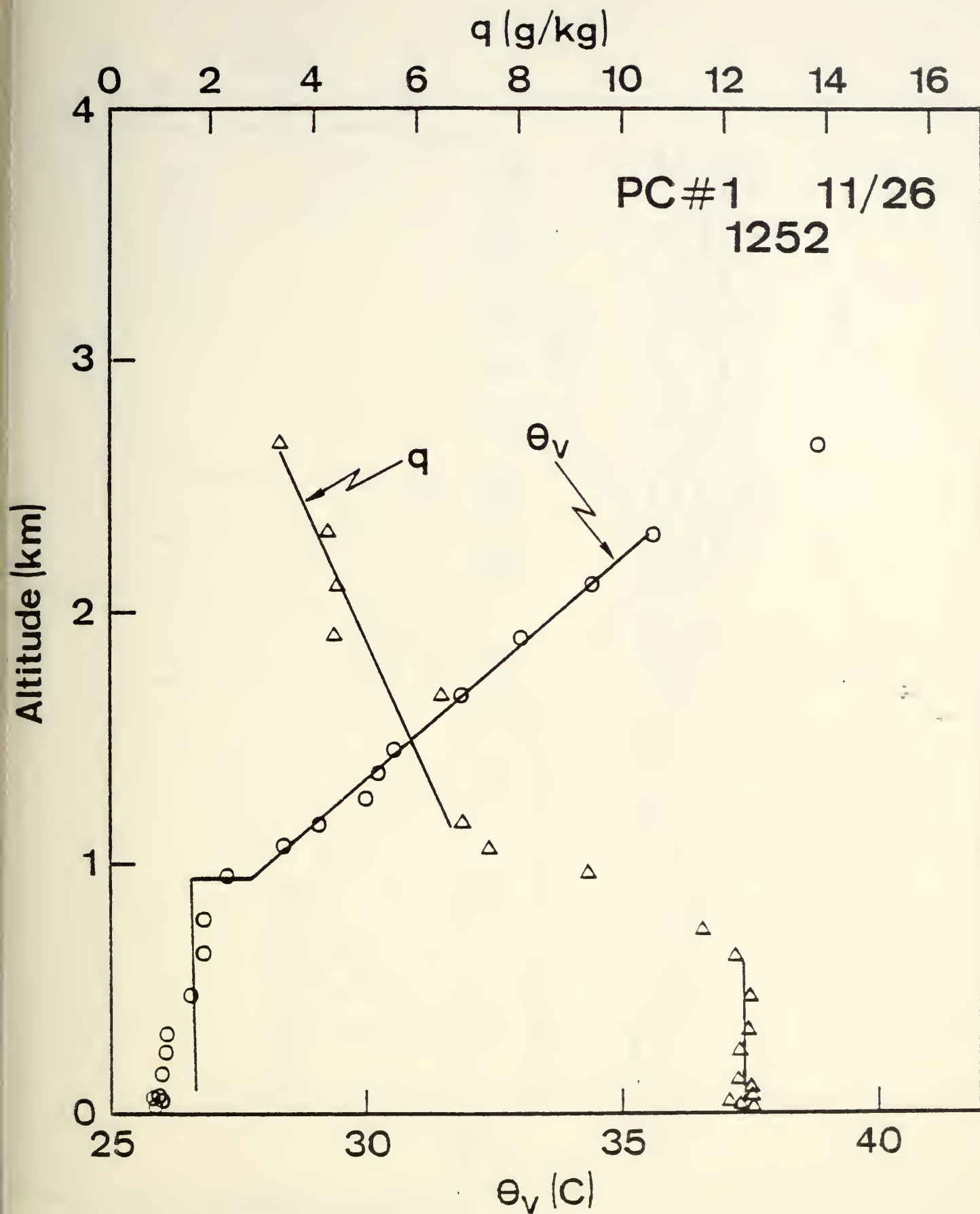
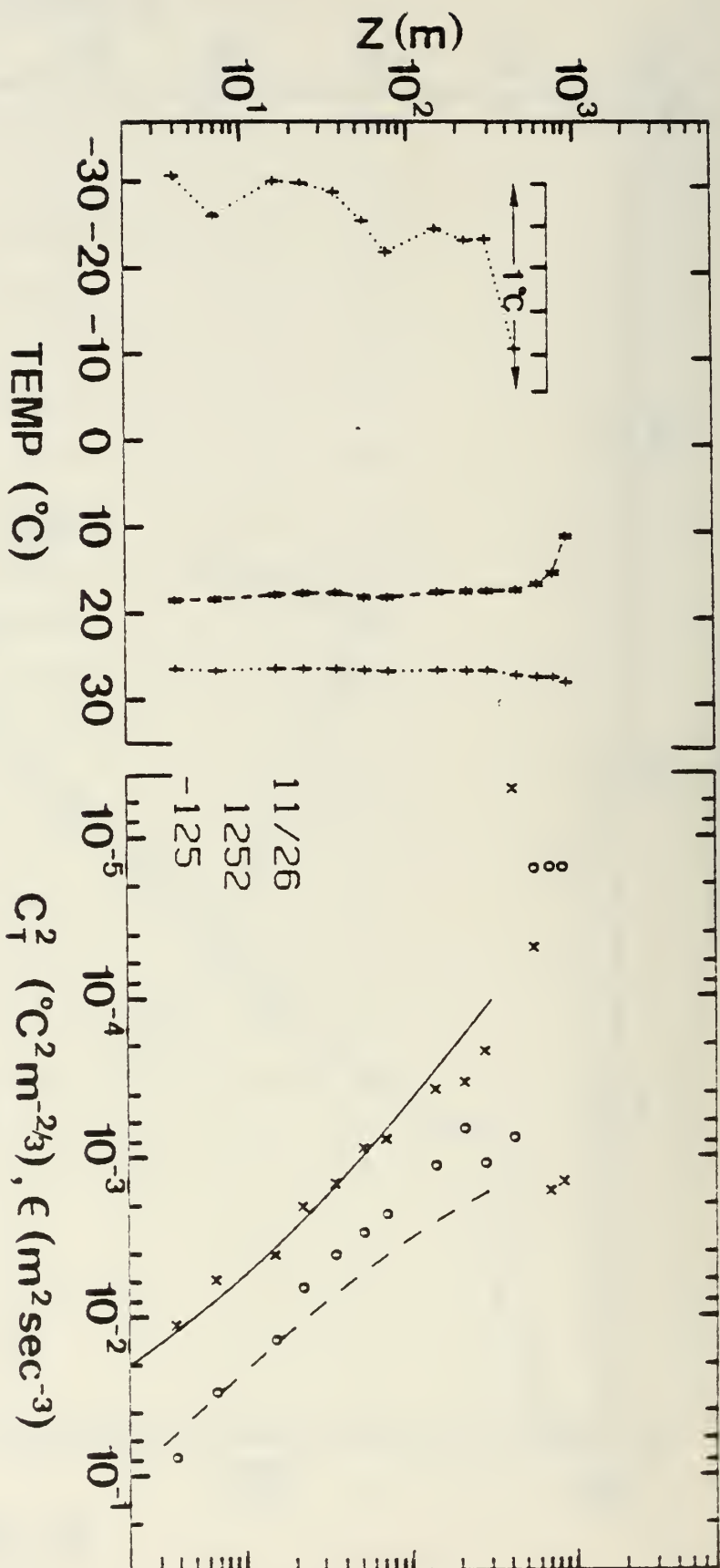


Figure 11a. Mean profile for

PC 11/26 1252.



NOTE: The data points plotted are virtual potential temperature (+), dew point temperature (*), C_T^2 (x), and ϵ (o). The solid line is the MOS expression for C_T^2 , and the long dash line is the MOS expression for ϵ . The extreme left-hand side of the graph shows an expanded scale plot of virtual potential temperature. The date, time, and Monin-Obukhov stability length, L , are given in the lower center of the graph.

Figure 1b. Turbulence profile for PC 11/26 1257.

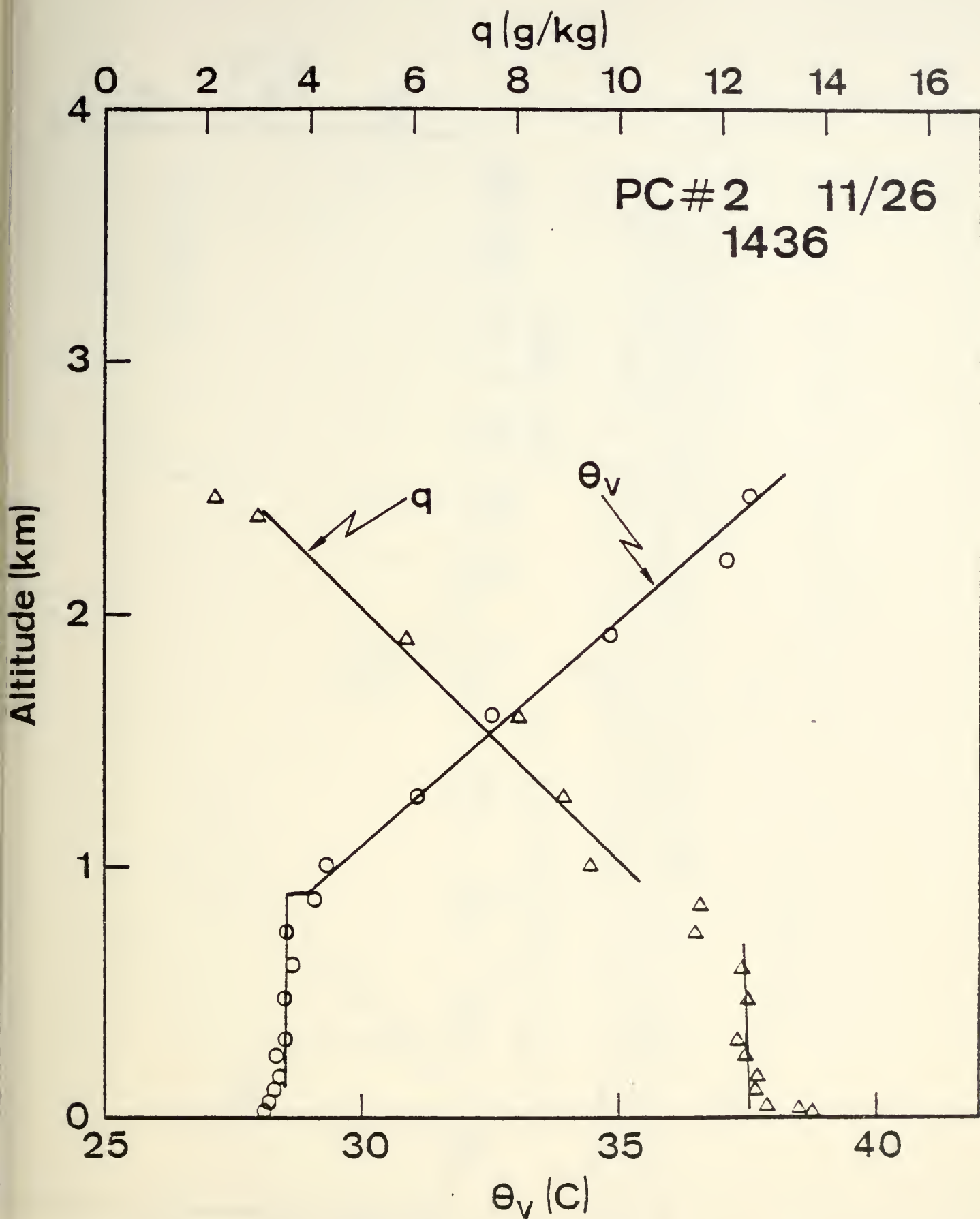
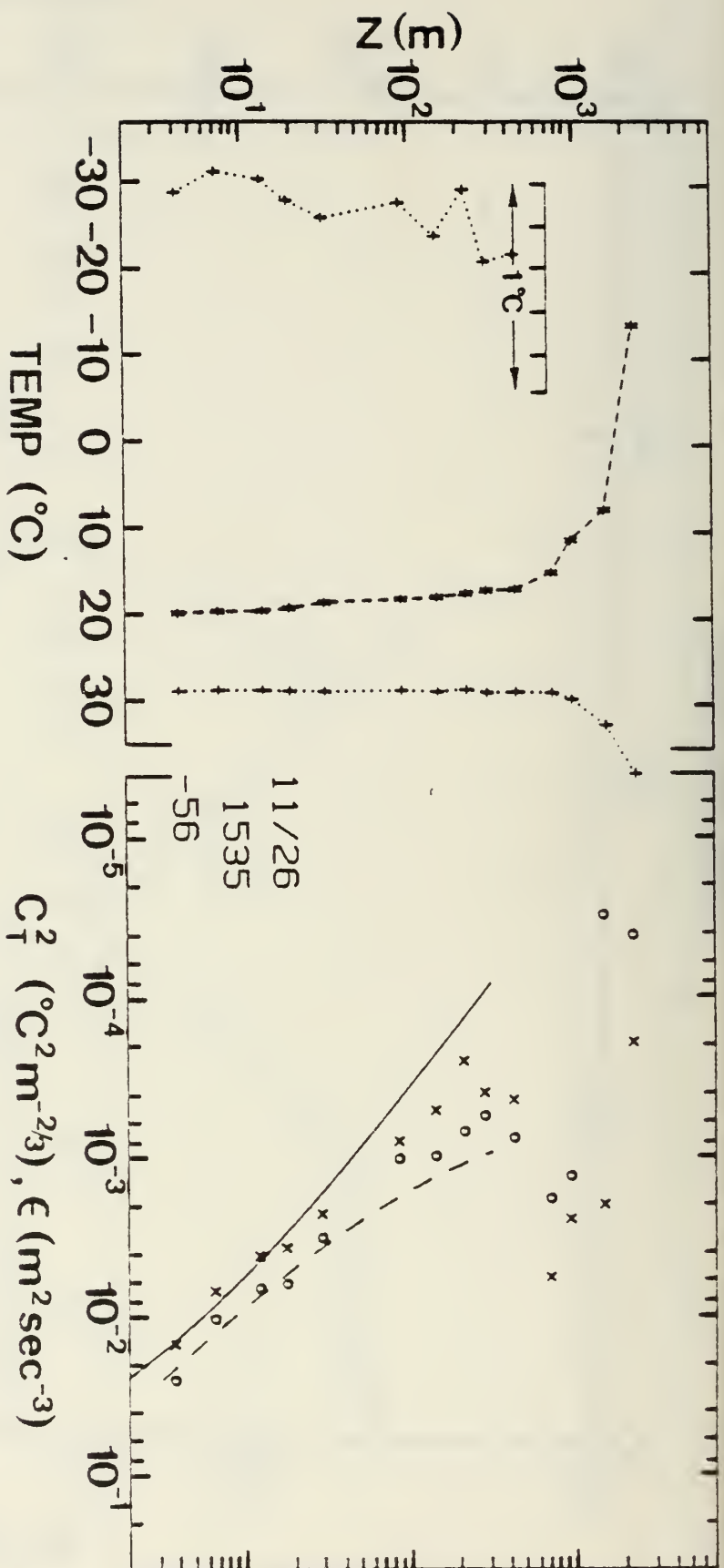


Figure A2a. Mean profile for PC 11/26 1436.



NOTE: The data points plotted are virtual potential temperature (+), dew point temperature (*), C_T^2 (x), and ϵ (o). The solid line is the MOS expression for C_T^2 , and the long dash line is the MOS expression for ϵ . The extreme left-hand side of the graph shows an expanded scale plot of virtual potential temperature. The date, time and Monin-Obukhov stability length, L , are given in the lower center of the graph.

Figure A2b. Turbulence profile for PC 11/26 1430.

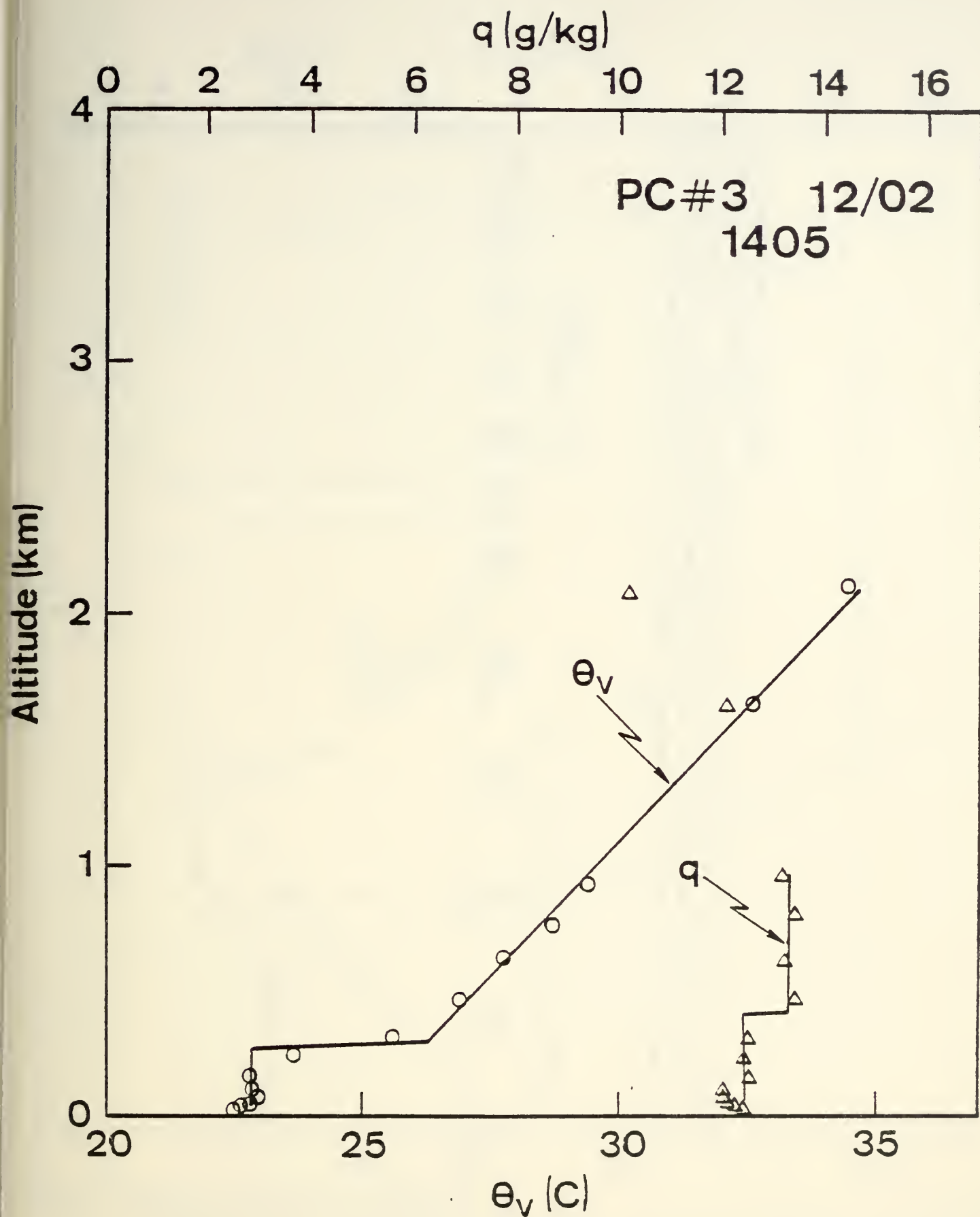
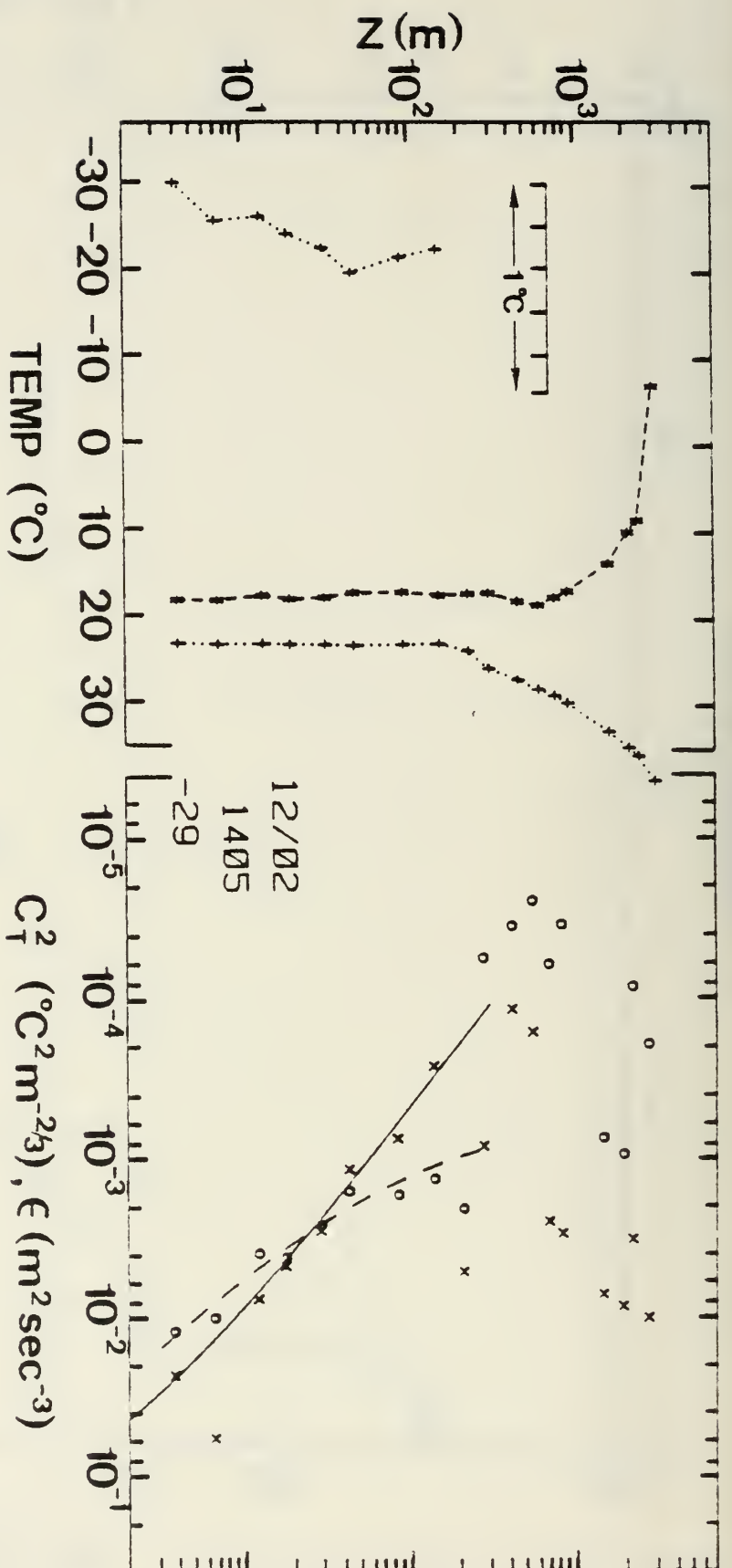
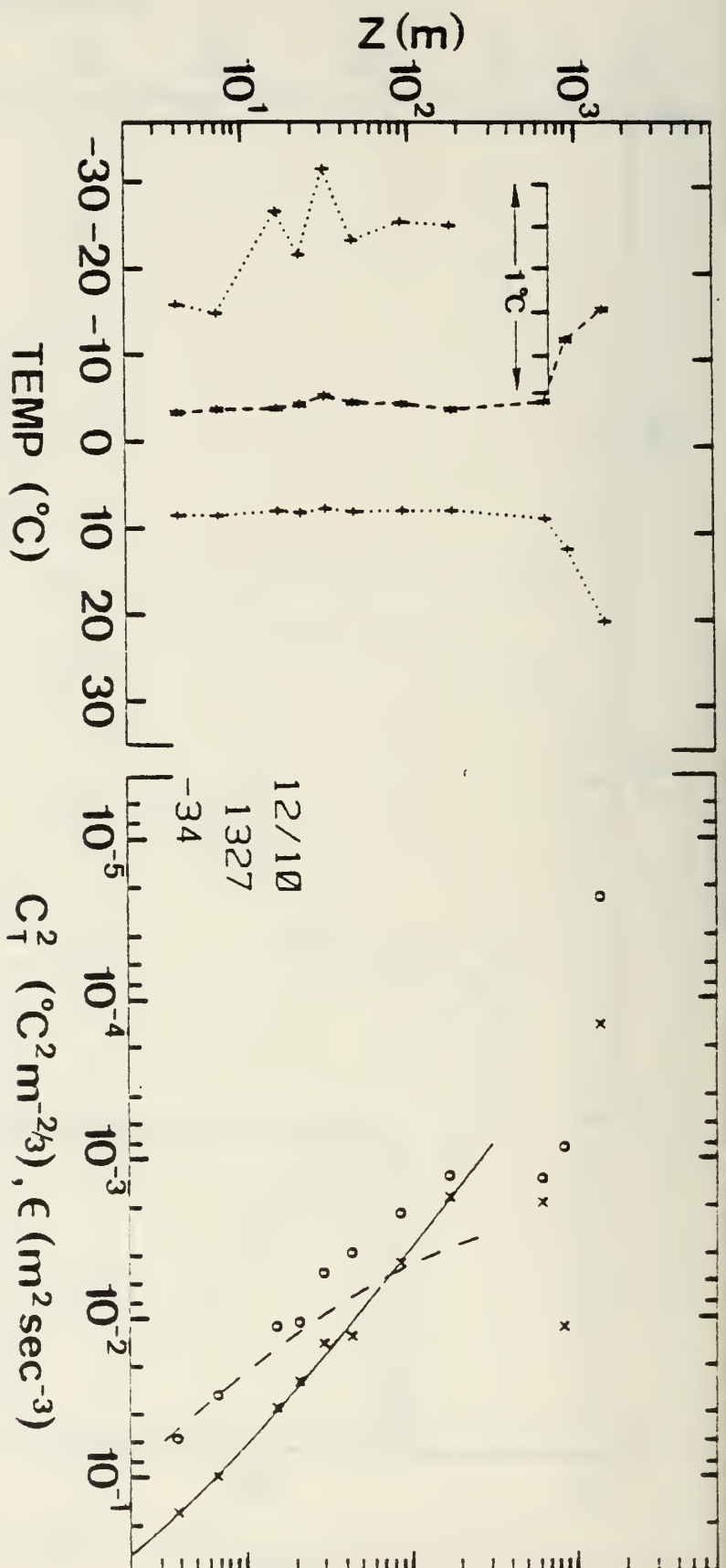


Figure A3a. Mean profile for PC 12/2 1405.



NOTE: The data points plotted are virtual potential temperature (+), dew point temperature (*), CT^2 (x), and ϵ (o). The solid line is the MOS expression for CT^2 , and the long dash line is the MOS expression for ϵ . The extreme left-hand side of the graph shows an expanded scale plot of virtual potential temperature. The date, time, and Monin-Obukhov stability length, L , are given in the lower center of the graph.

Figure A3b. Turbulence profile for PC 12/2 1405.



NOTE: The data points plotted are virtual potential temperature (+), dew point temperature (*), CT^2 (x), and ϵ (o). The solid line is the MOS expression for CT^2 , and the long dash line is the MOS expression for ϵ . The extreme left-hand side of the graph shows an expanded scale plot of virtual potential temperature. The date, time, and Monin-Obukhov stability length, L , are given in the lower center of the graph.

Figure A4b. Turbulence profile for PC 12/10 1324.

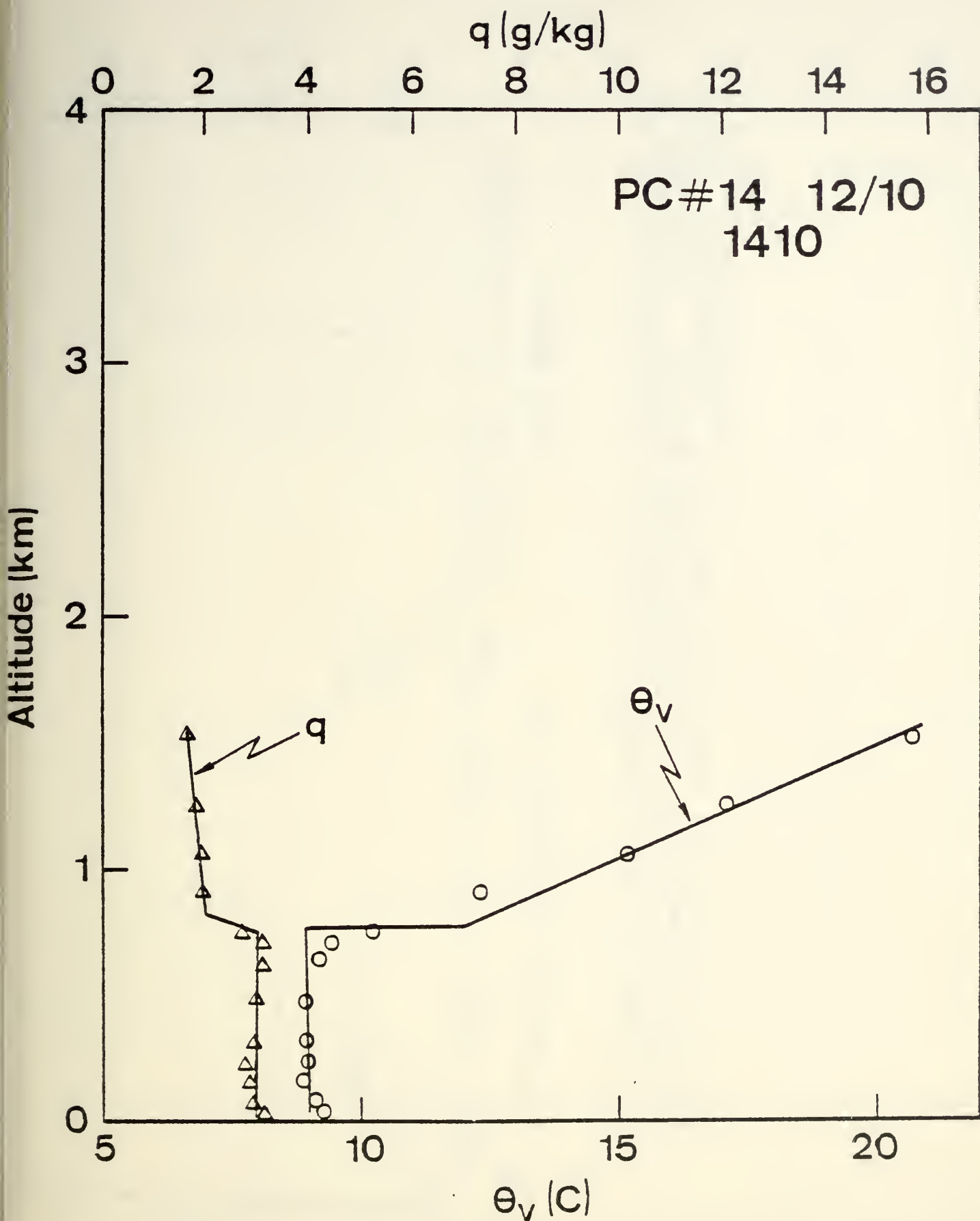
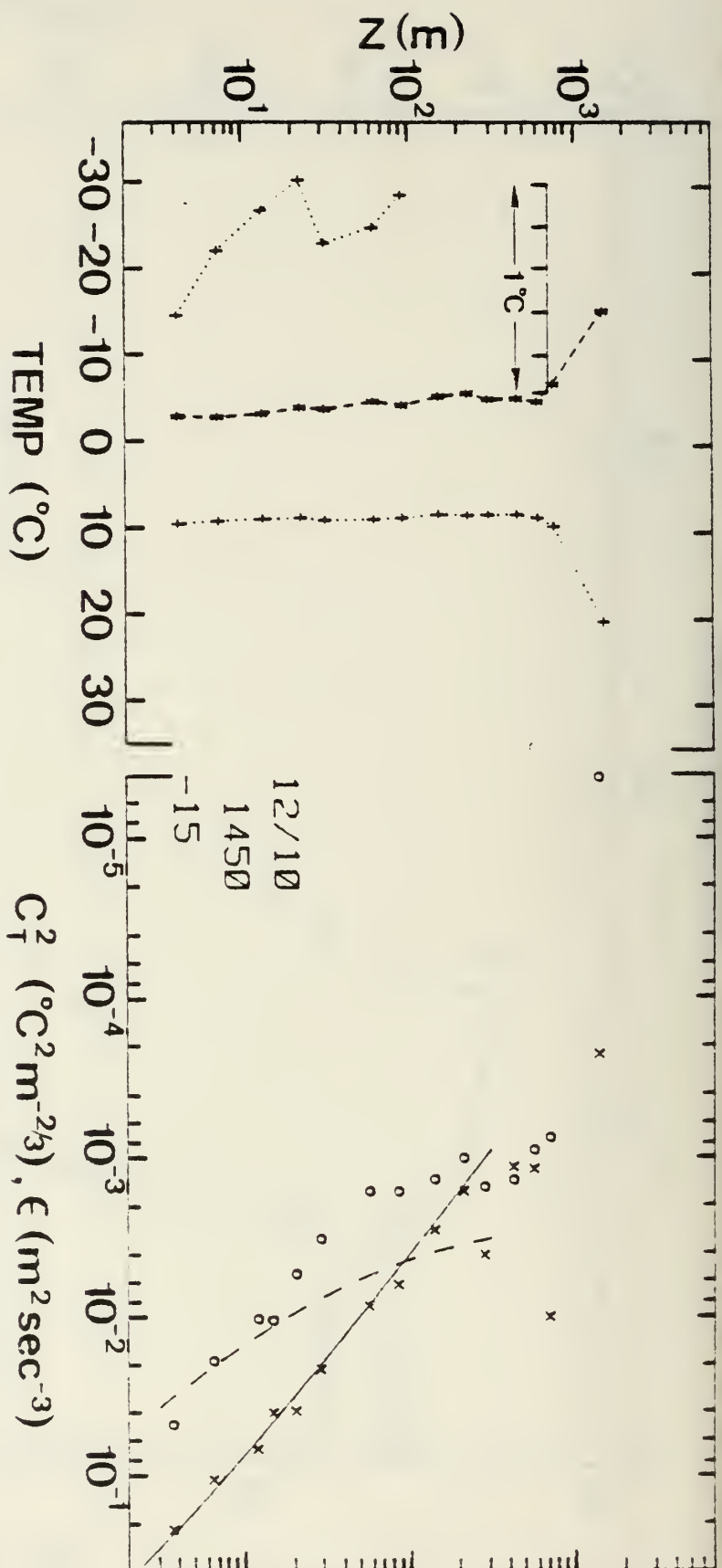


Figure A5a. Mean profile for PC 12/10 1410.



NOTE: The data points plotted are virtual potential temperature (+), dew point temperature (*), CT_2 (x), and $\epsilon(0)$. The solid line is the MOS expression for CT_2 , and the long dash line is the MOS expression for ϵ . The extreme left-hand side of the graph shows an expanded scale plot of virtual potential temperature. The date, time, and Monin-Obukhov stability length, L , are given in the lower center of the graph.

Figure A5b. Turbulence profile for PC 12/10 1410.

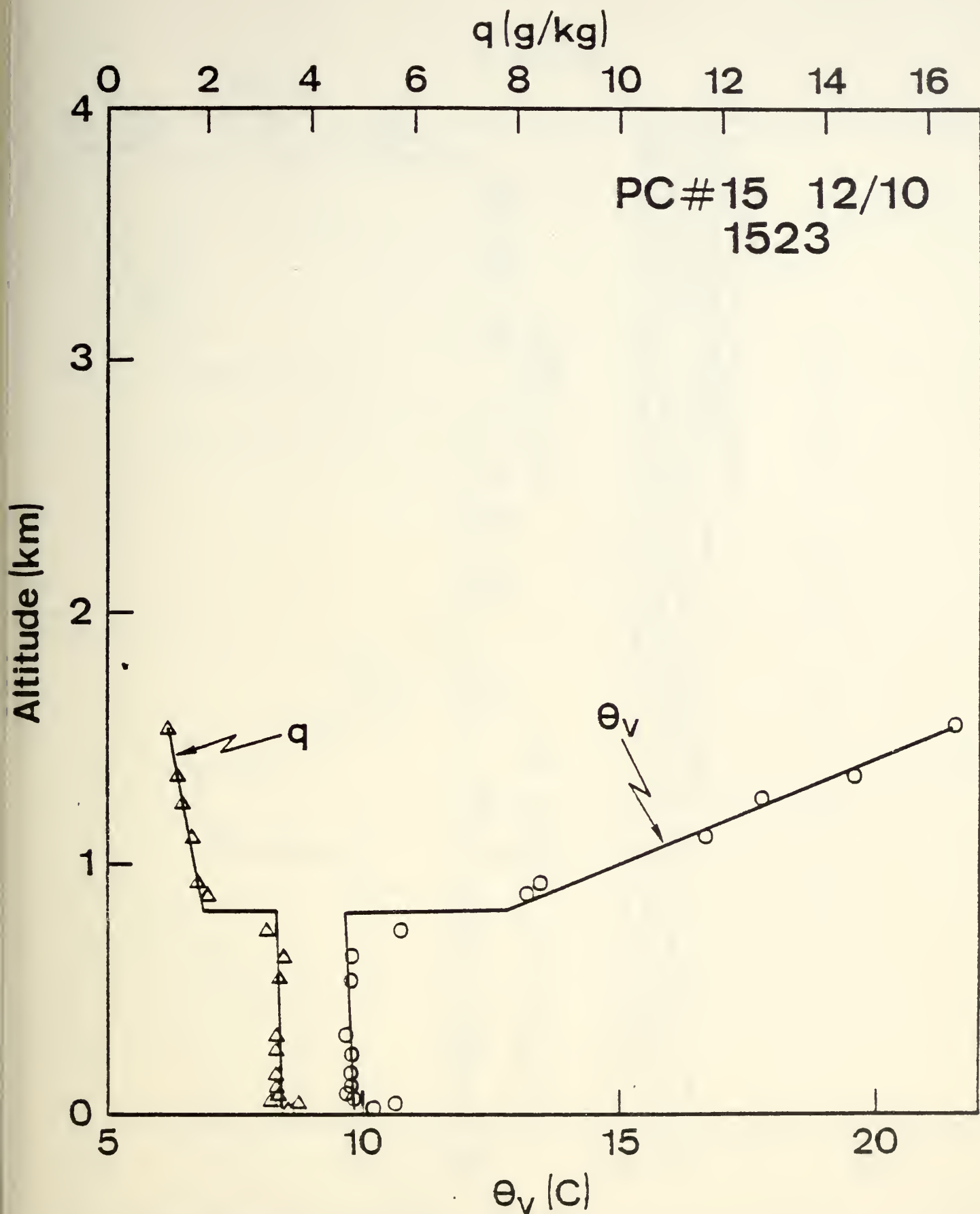
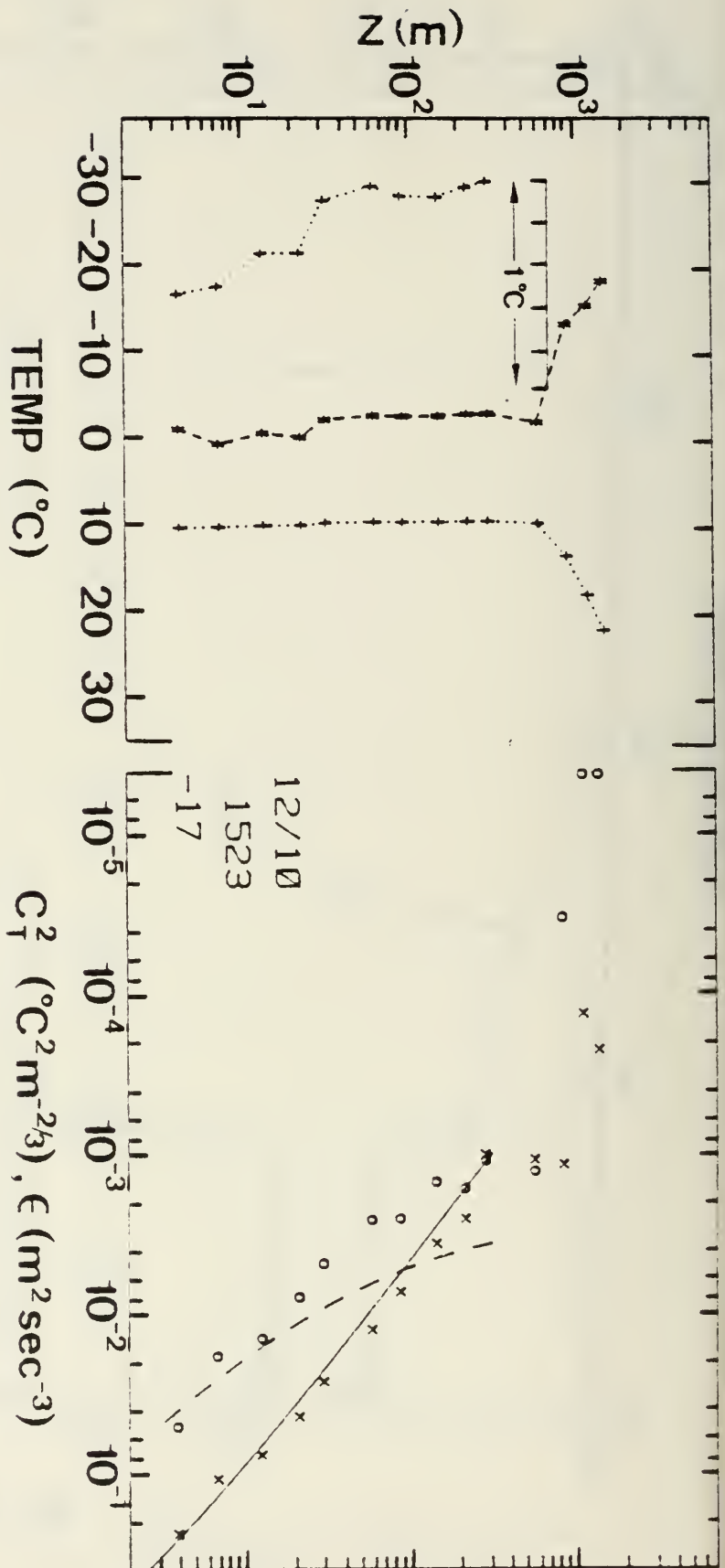


Figure A6a. Mean profile for PC 12/10 1523.



NOTE: The data points plotted are virtual potential temperature (+), dew point temperature (*), C_T^2 (x), and ϵ (o). The solid line is the MOS expression for C_T^2 , and the long dash line is the MOS expression for ϵ . The extreme left-hand side of the graph shows an expanded scale plot of virtual potential temperature. The date, time, and Monin-Obukhov stability length, L , are given in the lower center of the graph.

Figure A6b. Turbulence profile for PG 12/10 1523.

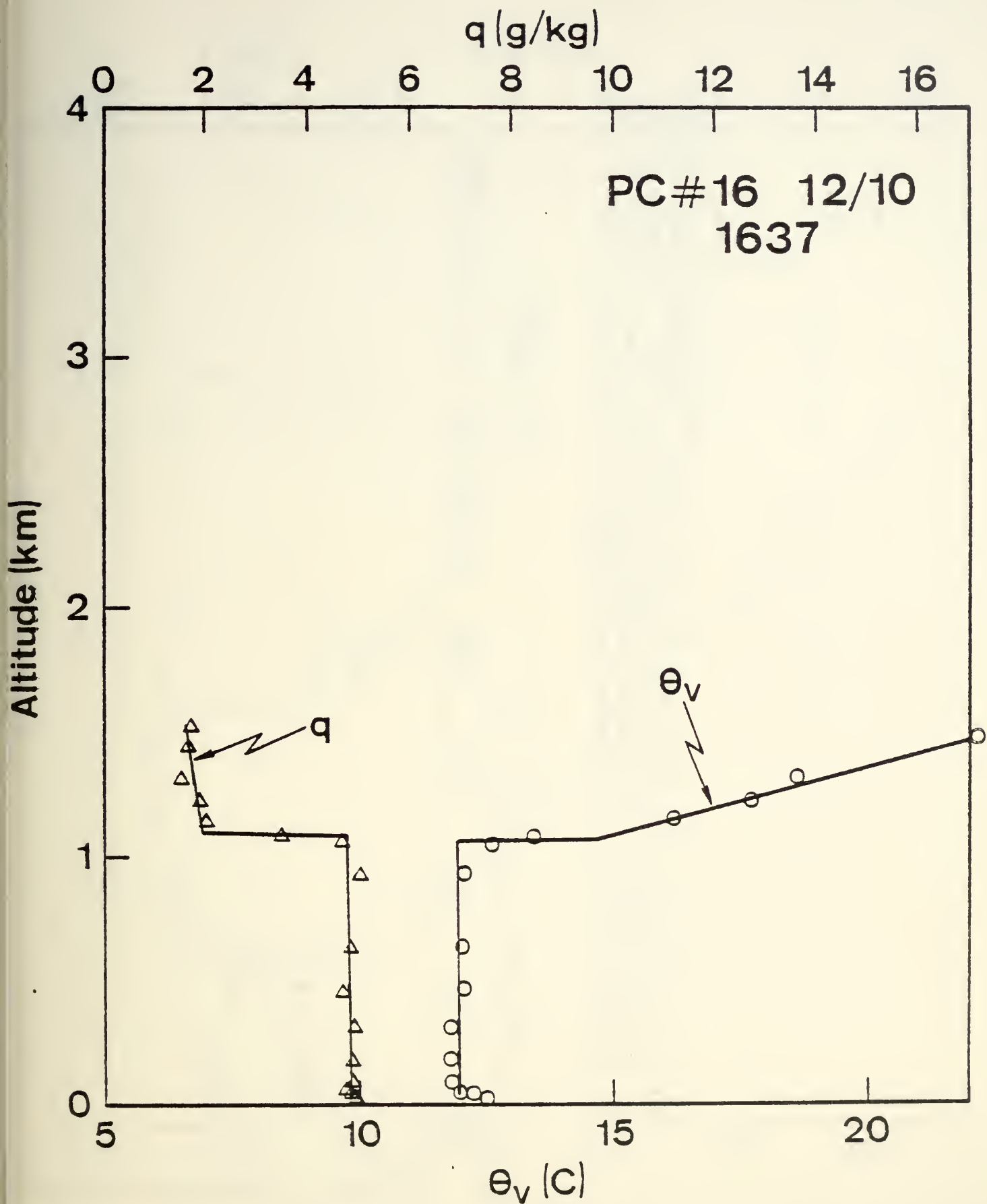
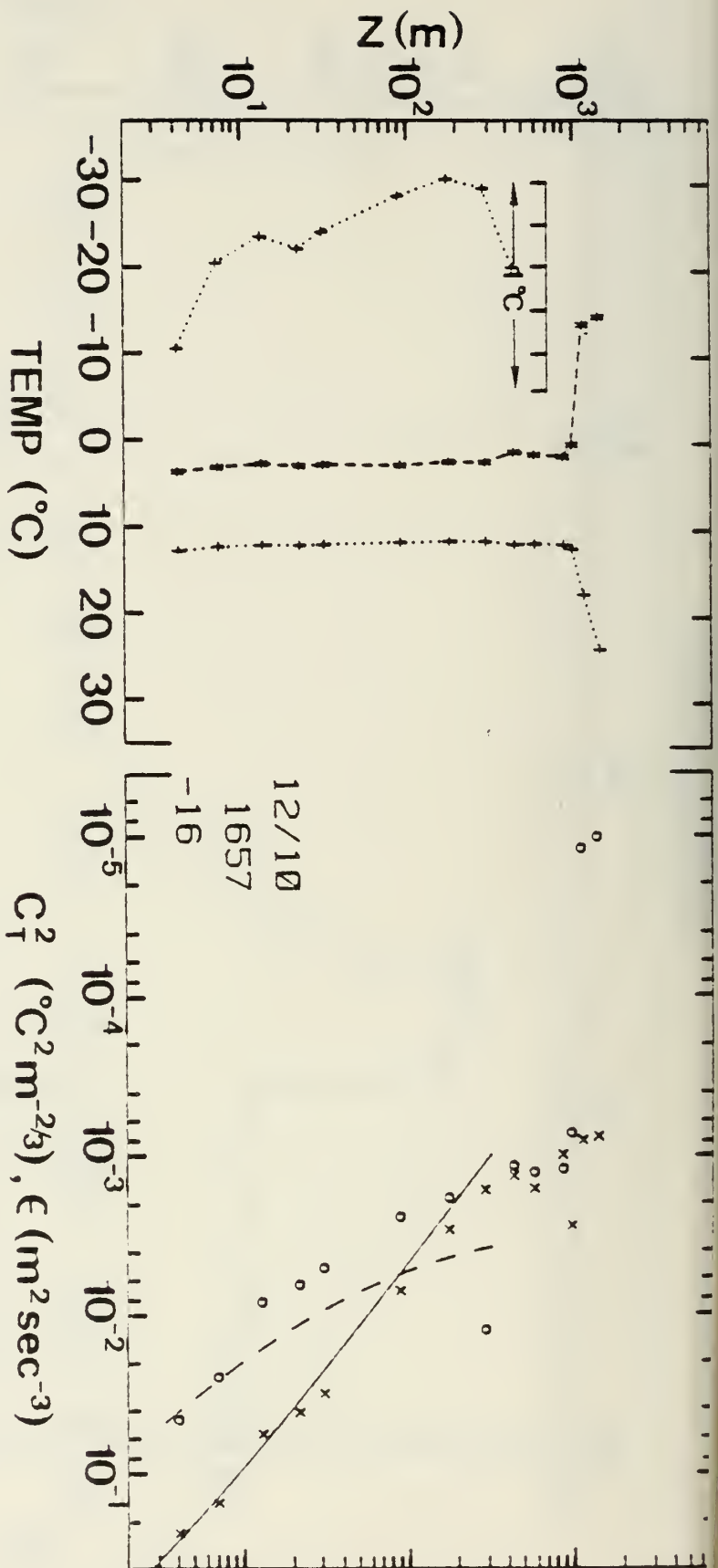


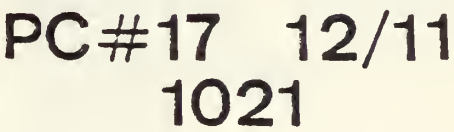
Figure A7a. Mean profile for

PC 12/10 1637.

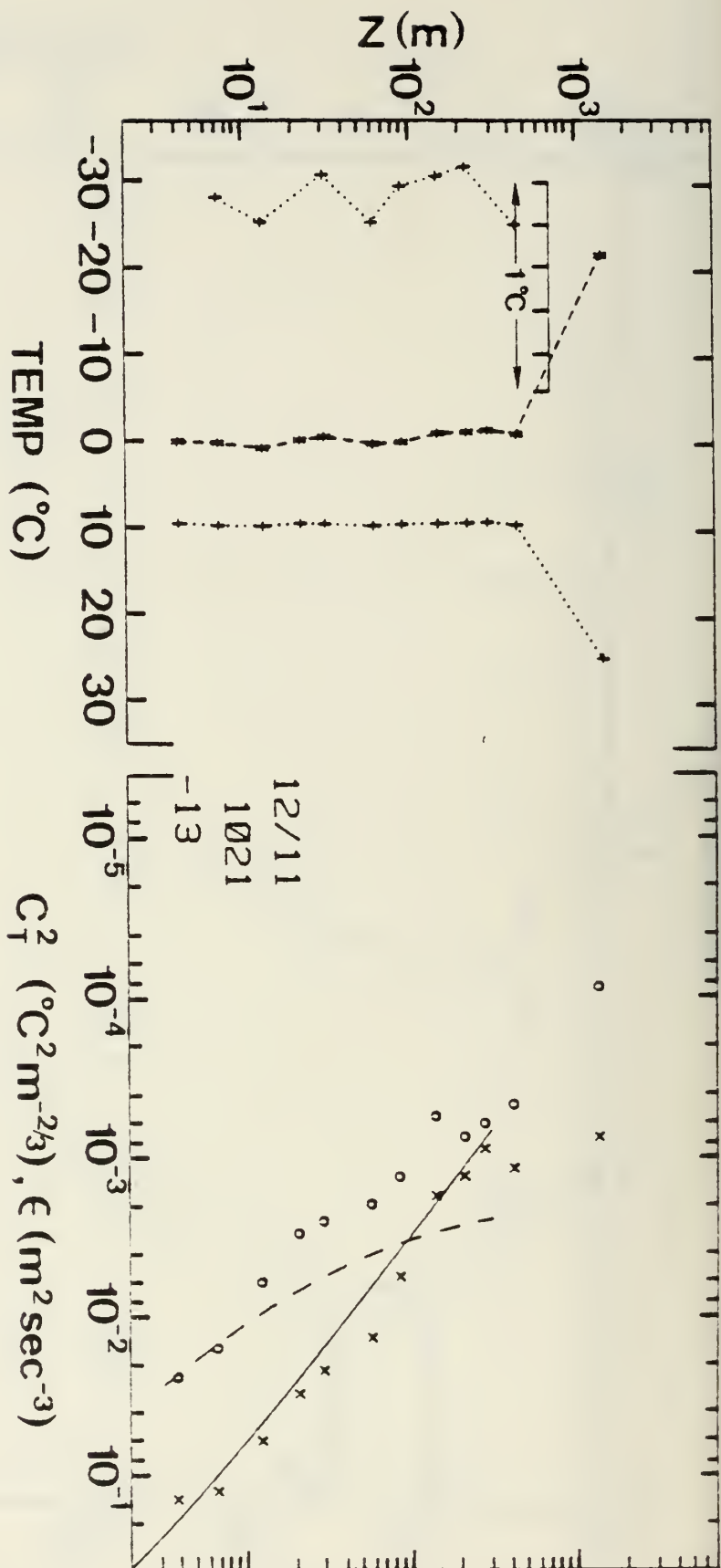


NOTE: The data points plotted are virtual potential temperature (+), dew point temperature (*), CT_2 (x), and ϵ (o). The solid line is the MOS expression for CT_2 , and the long dash line is the MOS expression for ϵ . The extreme left-hand side of the graph shows an expanded scale plot of virtual potential temperature. The date, time, and Month-Obukhov stability length, L, are given in the lower center of the graph.

Figure A7b. Turbulence profile for PC 12/10 1637.



PC 12/11 1021.



NOTE: The data points plotted are virtual potential temperature (+), dew point temperature (*), C_T^2 (x), and ϵ (o). The solid line is the MOS expression for C_T^2 , and the long dash line is the MOS expression for ϵ . The extreme left-hand side of the graph shows an expanded scale plot of virtual potential temperature. The date, time, and Monin-Obukhov stability length, L , are given in the lower center of the graph.

Figure 88b. Turbulence profile for PC 12/11 1021.

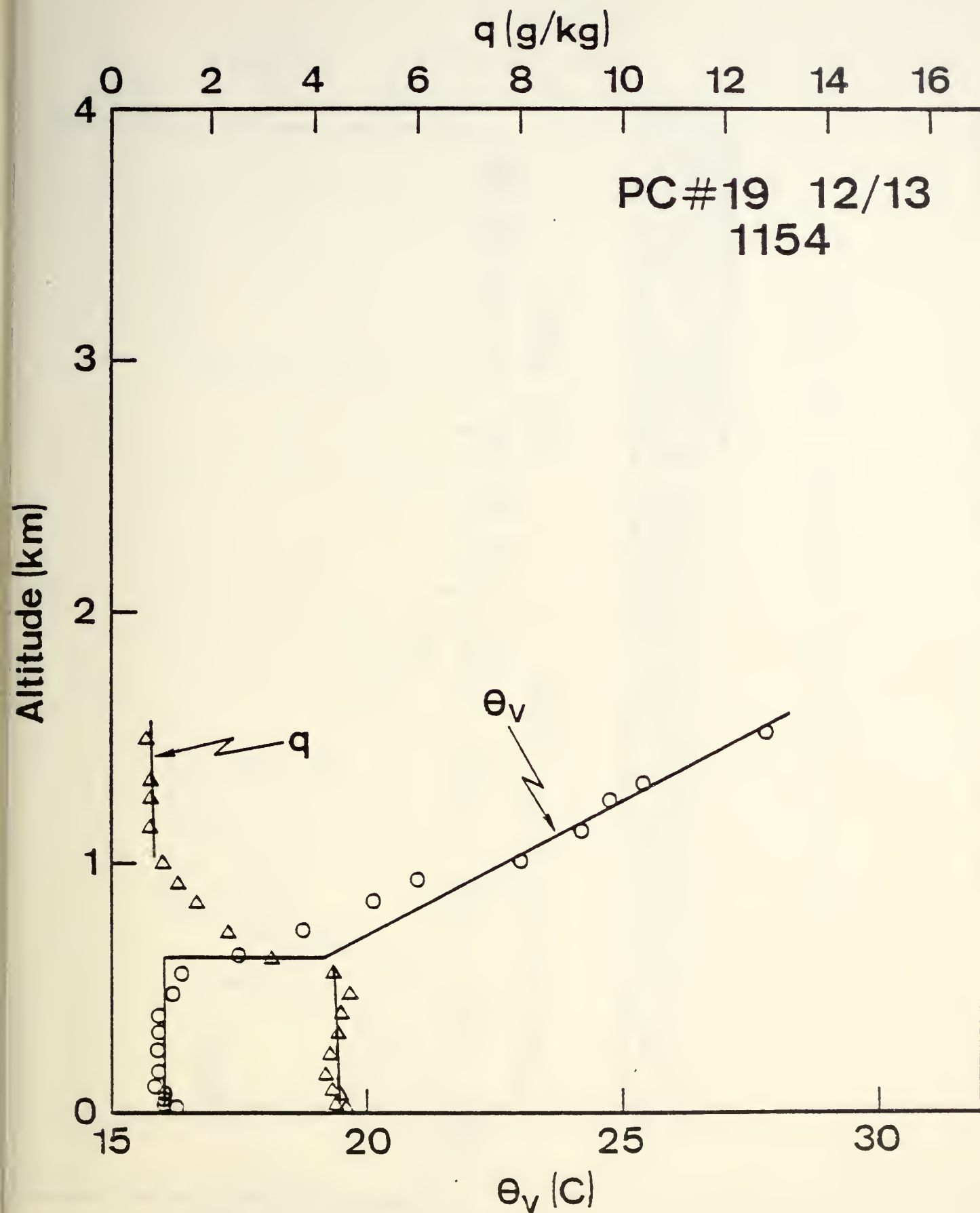
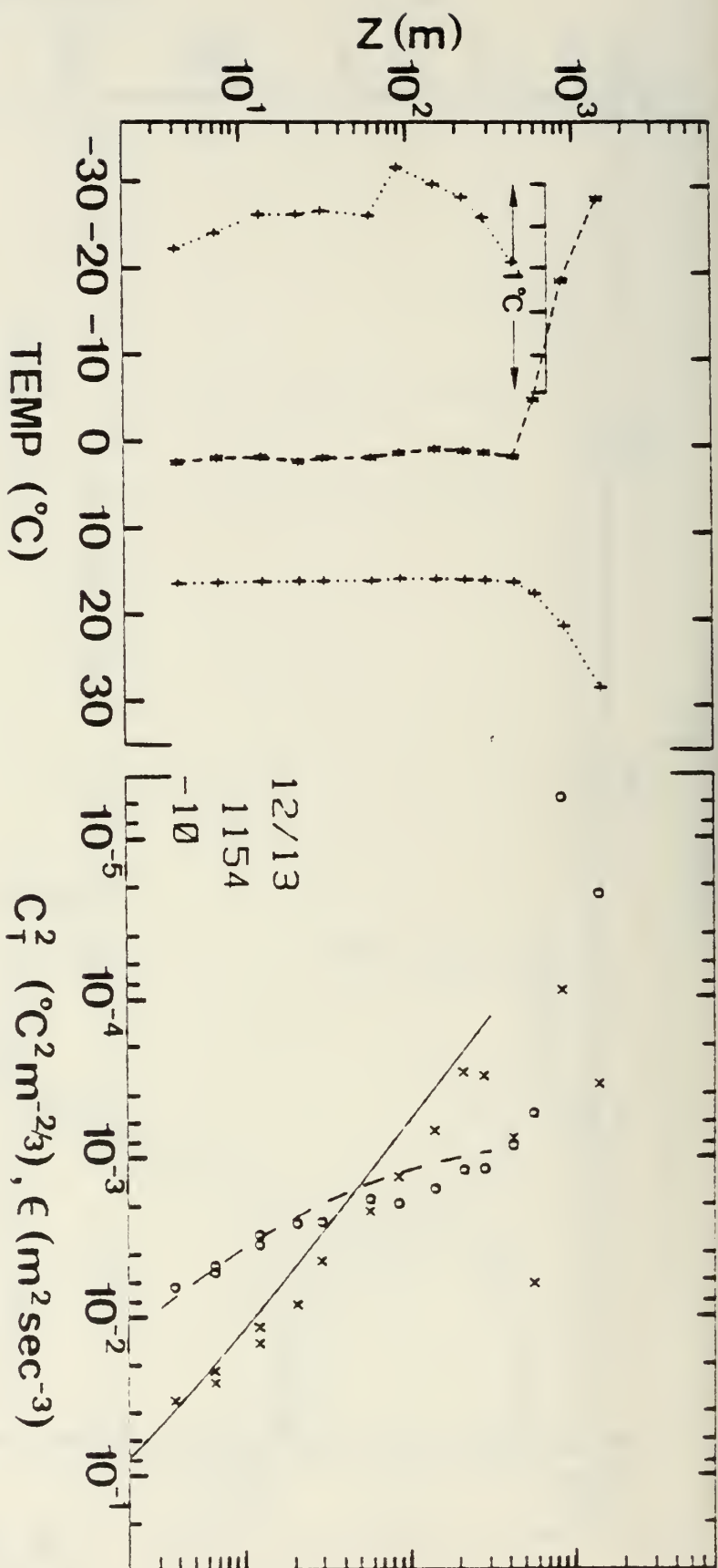


Figure A9a. Mean profile for PC 12/13 1154.



NOTE: The data points plotted are virtual potential temperature (+), dew point temperature (*), C_T^2 (x), and $e(0)$. The solid line is the MOS expression for C_T^2 , and the long dash line is the MOS expression for e . The extreme left-hand side of the graph shows an expanded scale plot of virtual potential temperature. The date, time, and Monin-Obukhov stability length, L , are given in the lower center of the graph.

Figure A9b. Turbulence profile for PG 12/13 1154.

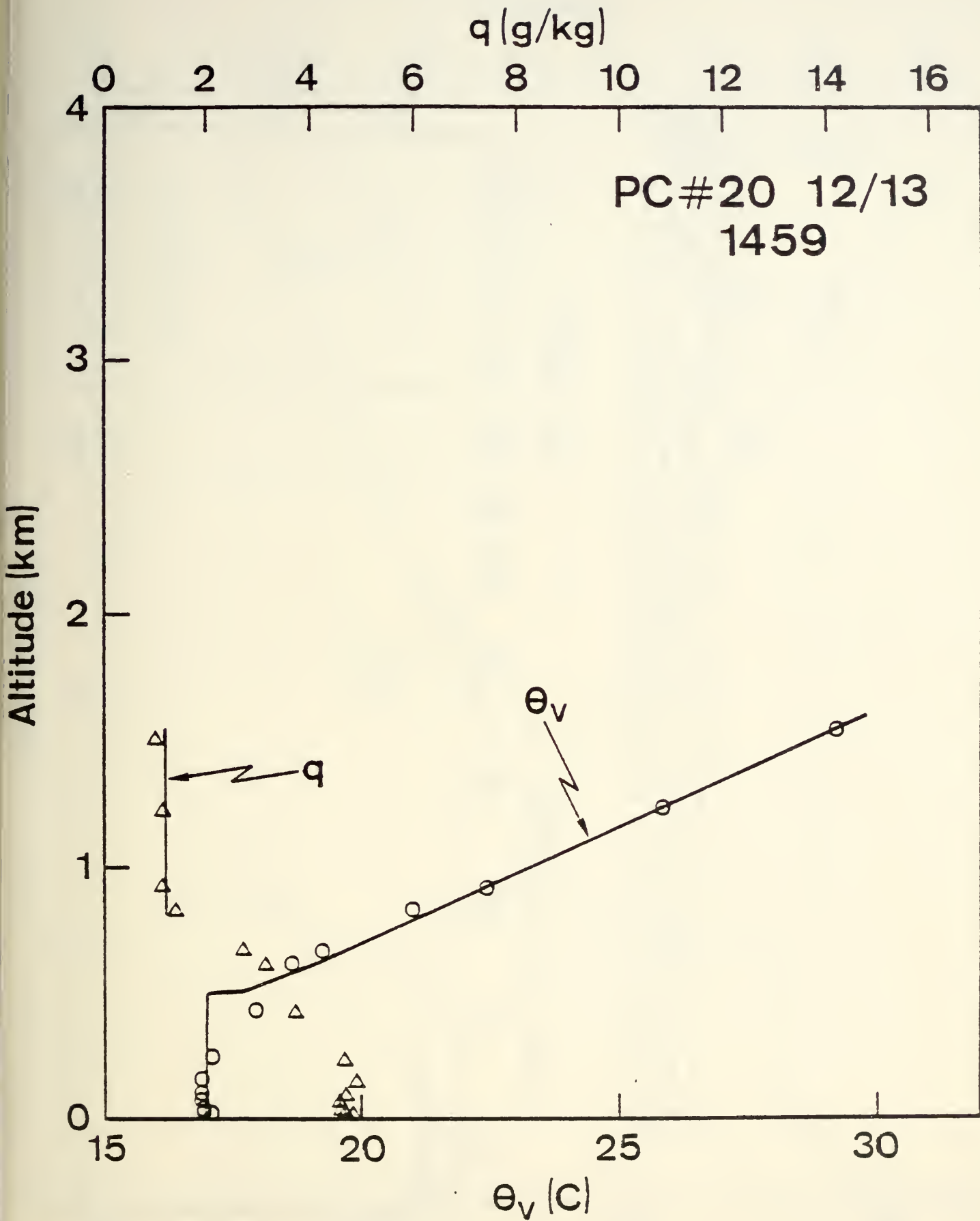
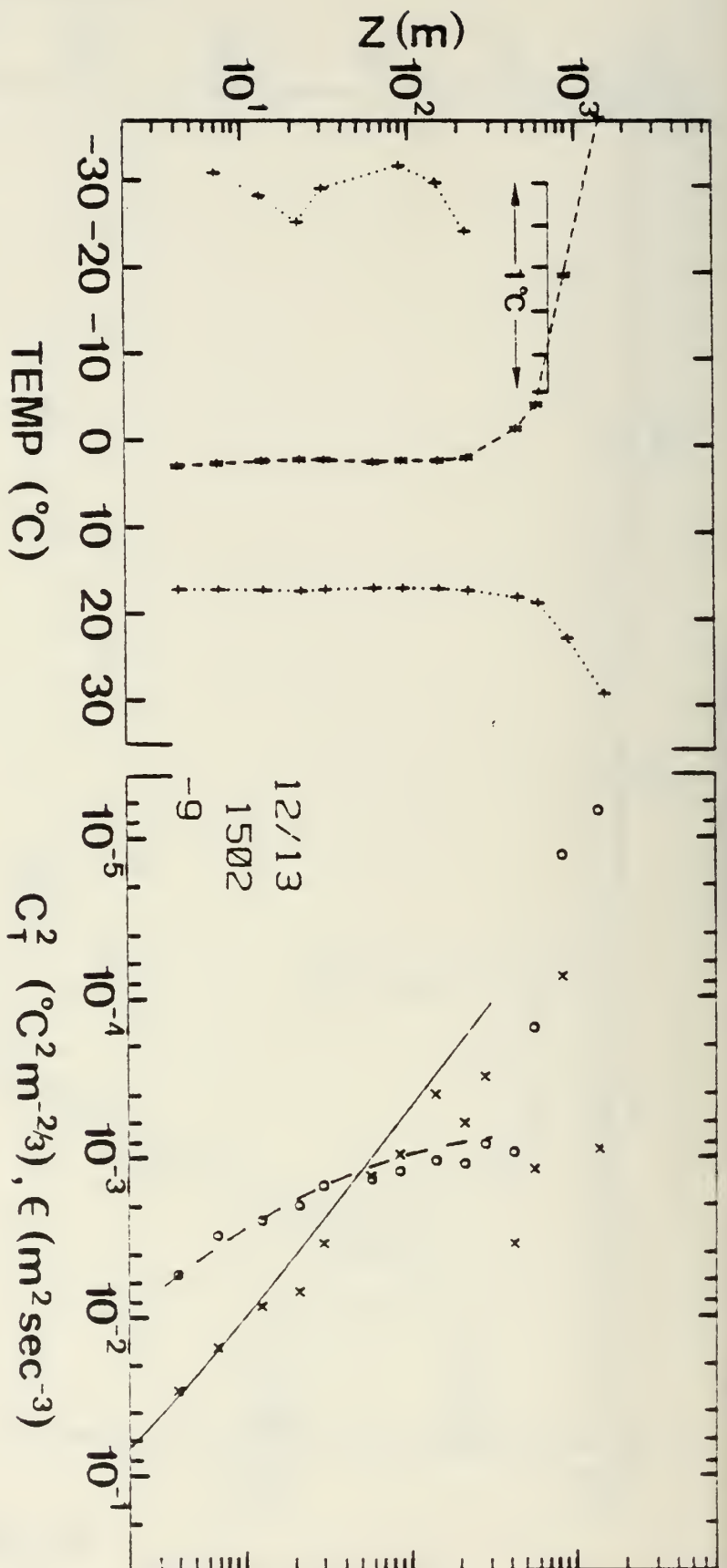
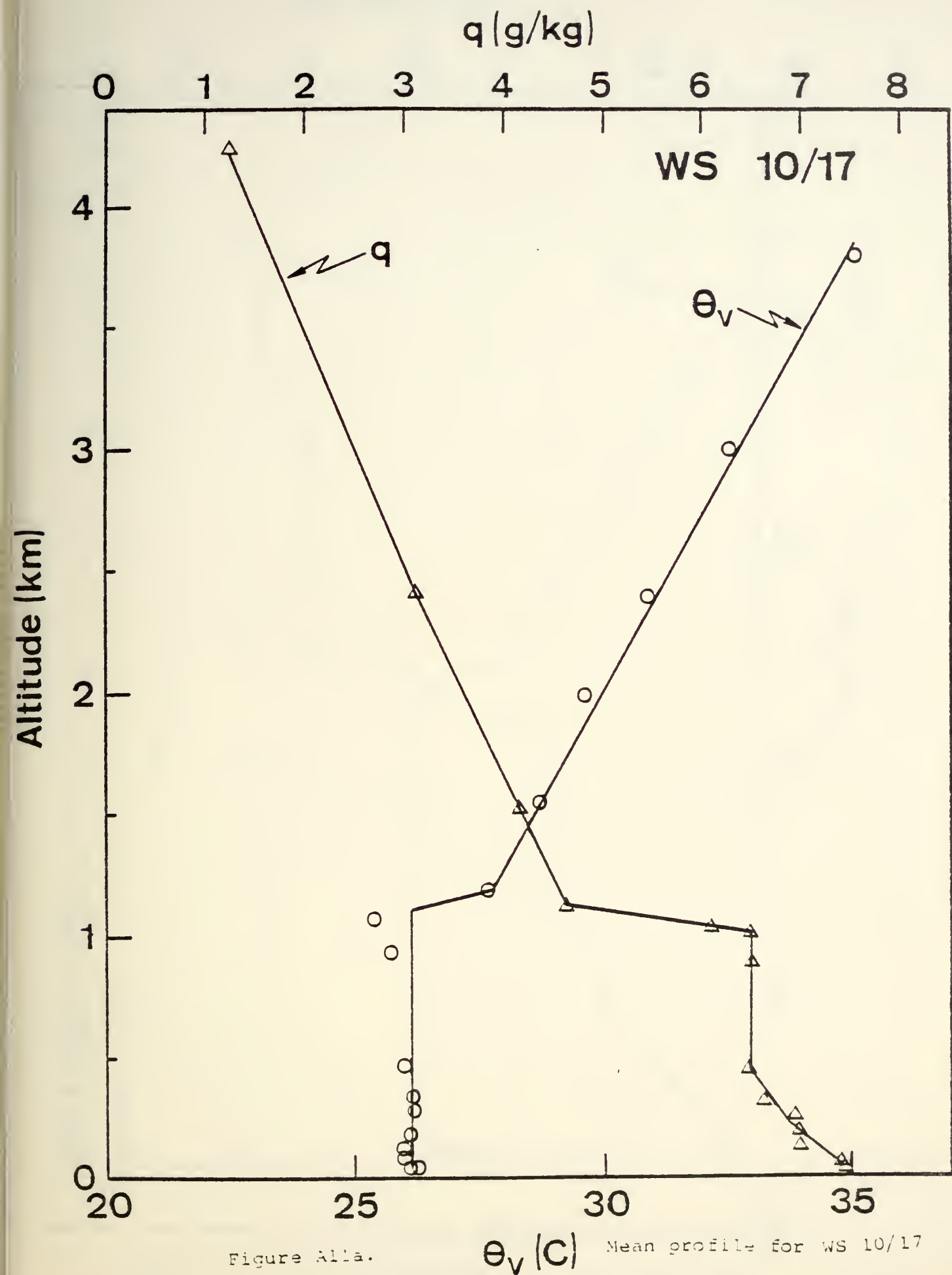


Figure A10a. Mean profile for PC 12/13 1459.



NOTE: The data points plotted are virtual potential temperature (+), dew point temperature (x), C_T^2 (x), and ϵ (o). The solid line is the MOS expression for C_T^2 , and the long dash line is the MOS expression for ϵ . The extreme left-hand side of the graph shows an expanded scale plot of virtual potential temperature. The date, time, and Monin-Obukhov stability length, L , are given in the lower center of the graph.

Figure A10b. Turbulence profile for FC 12/13 1459.



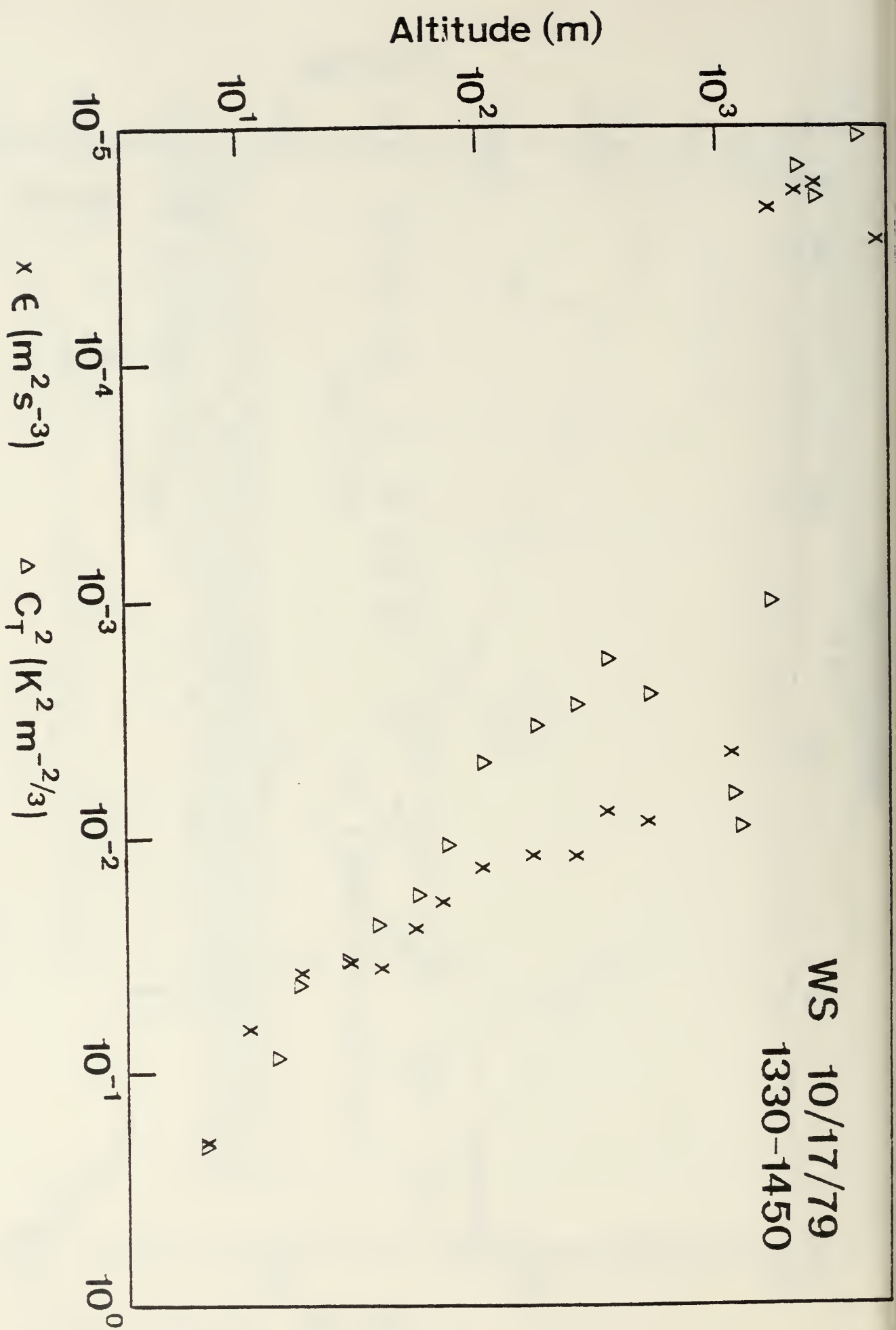


Figure A11b. Turbulence profile for WS 10/17 1330.

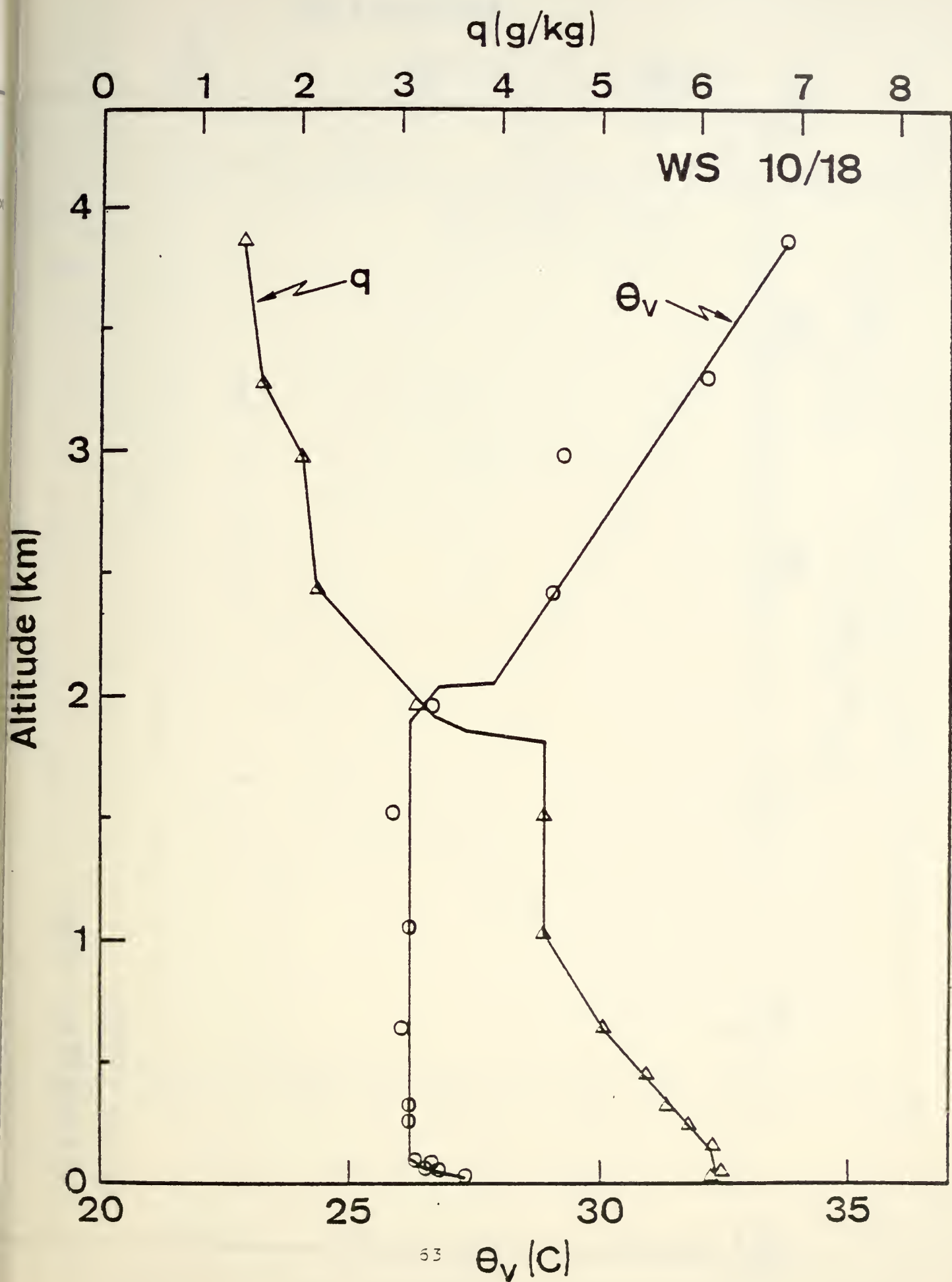


Figure A12a. Mean profile for WS 10/18 1330.

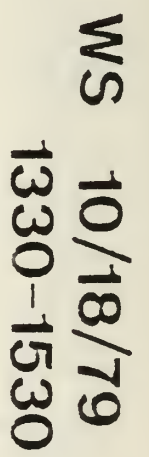


Figure A12b. Turbulence profile for WS 10/18 1330.

MIX RATIO (G/KG)

2 4 6 8 10

04/30 1446

HEIGHT (KM)

1.0

0.0

10 15 20 25 30 35

VP TEMP (CENT)

Figure A13a. Mean profile for

MG 4/30

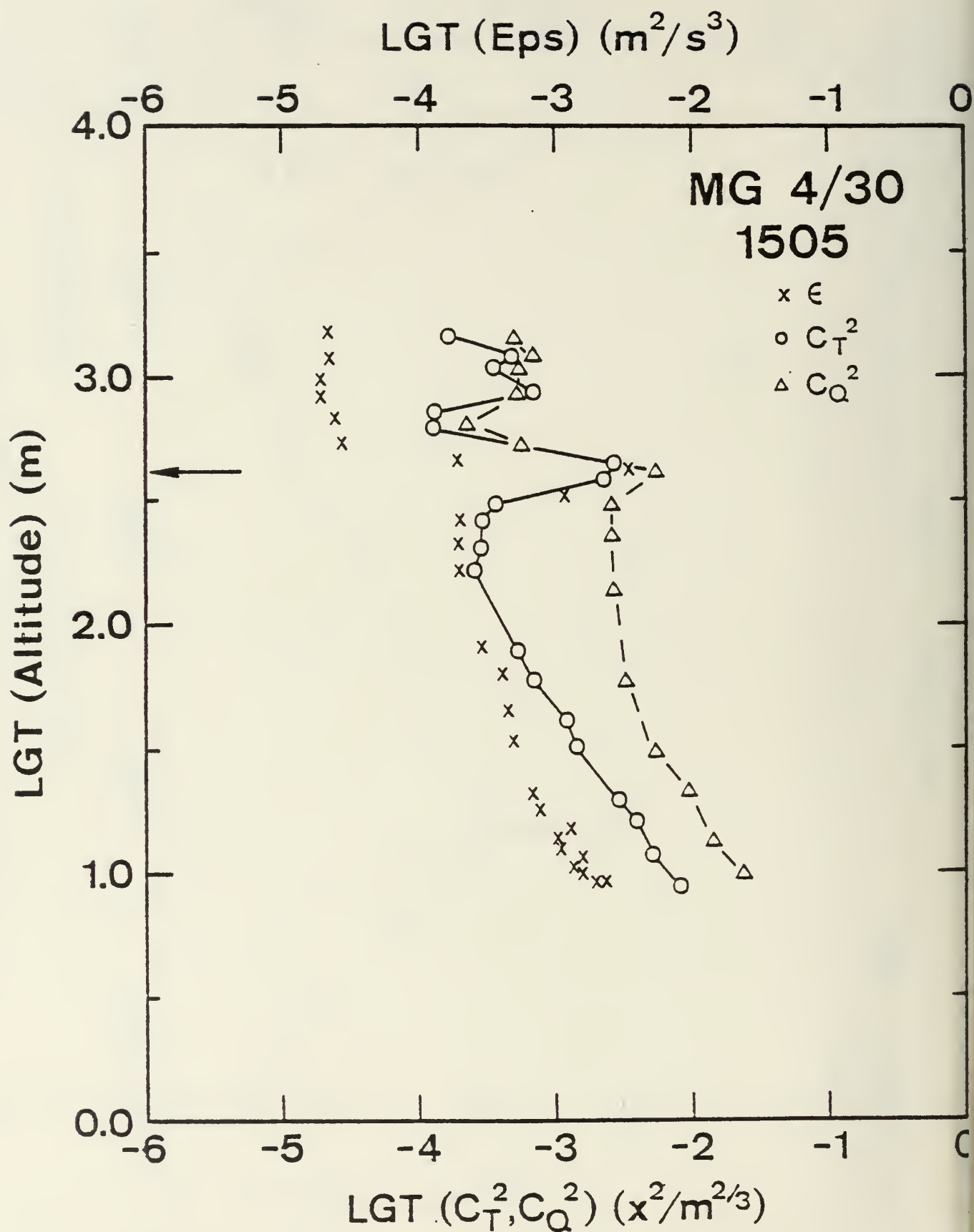


Figure A13b. Turbulence profile for MG 4/30

MIX RATIO (G/KG)

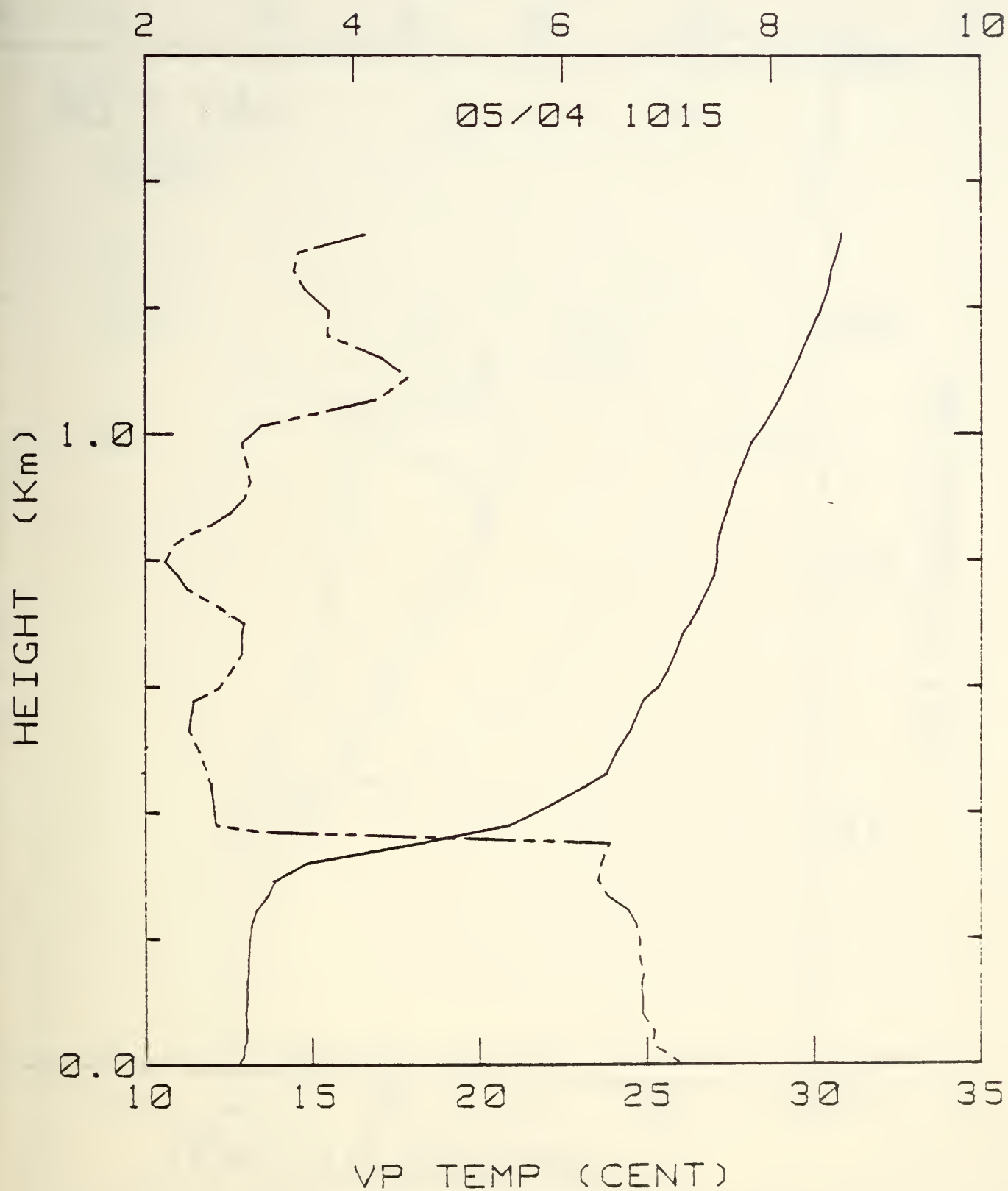


Figure A14a. Mean profile for MG 5/4 1024.

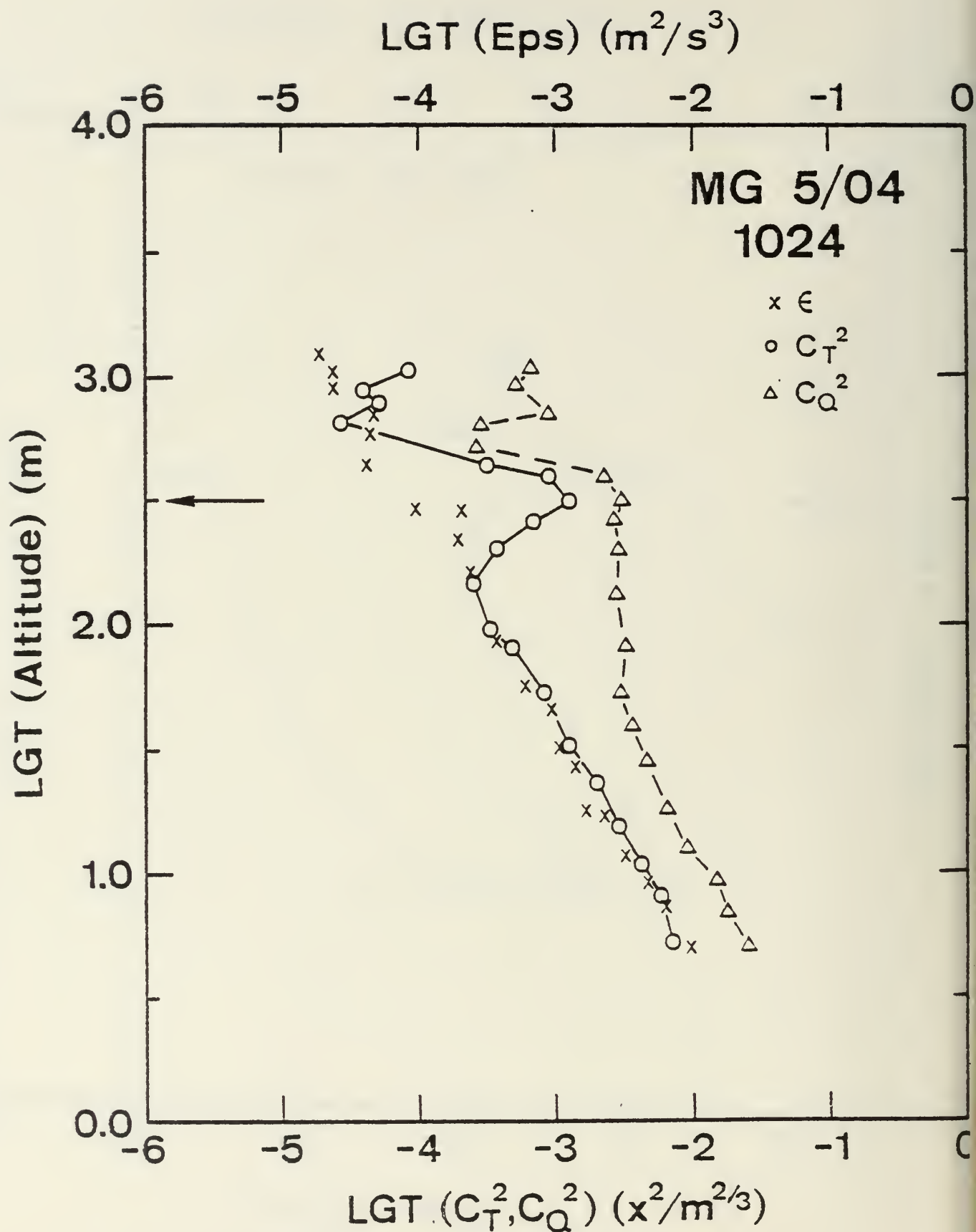


Figure A14b. Turbulence profile for MG 5/4 1024.

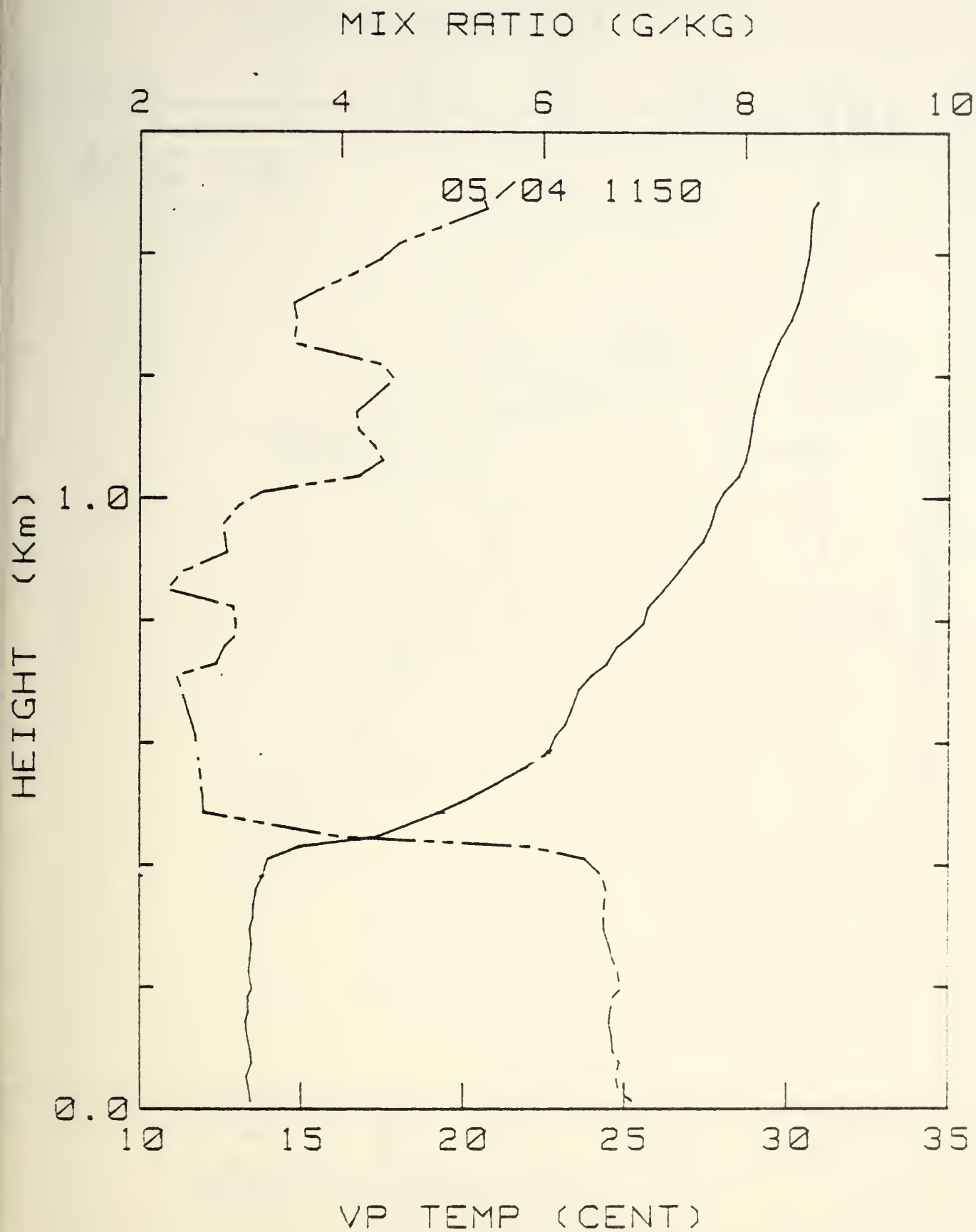


Figure A15a. Mean profile for MC 5/4 1201.

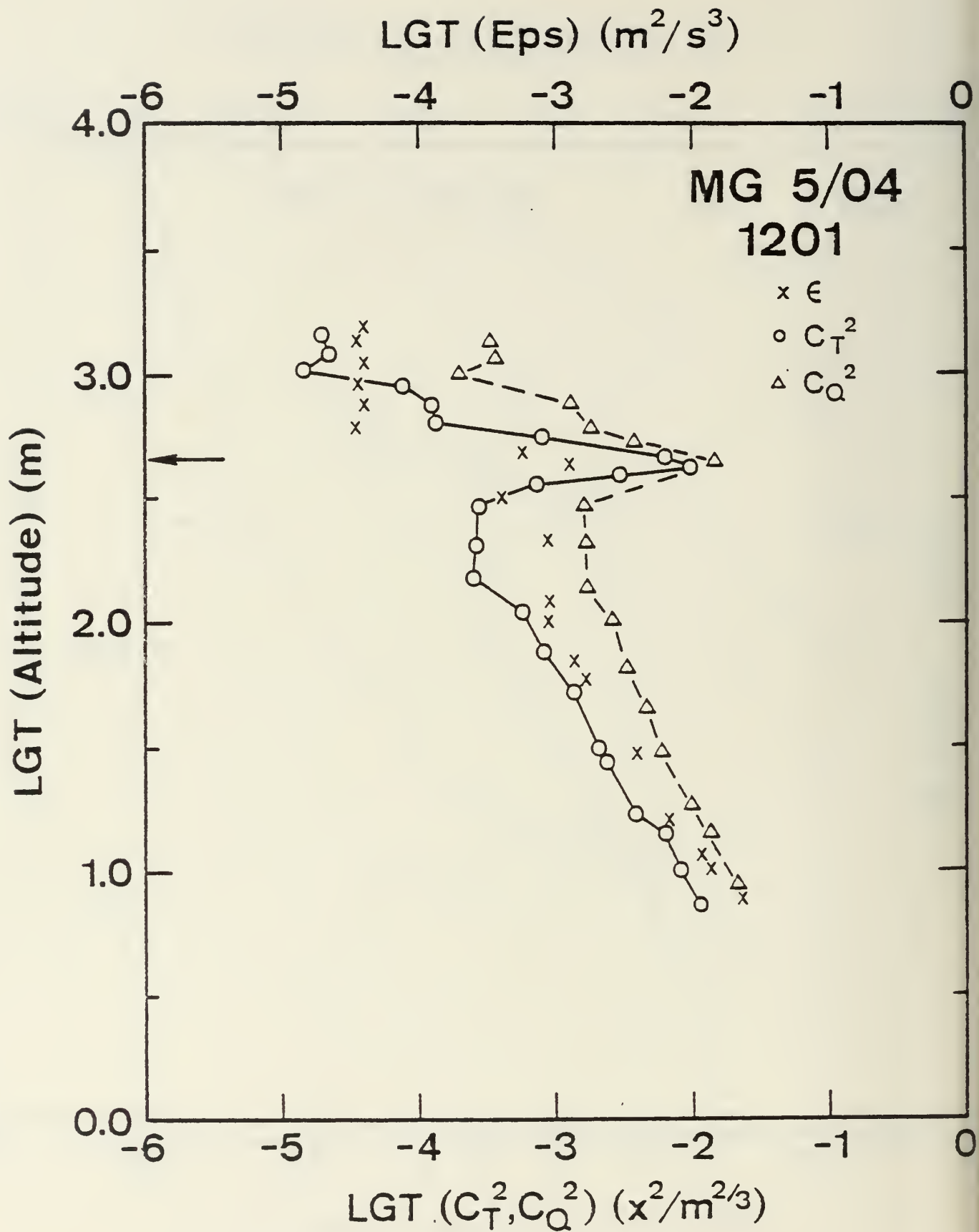


Figure A15b. Turbulence profile for MC 5,4 1201.

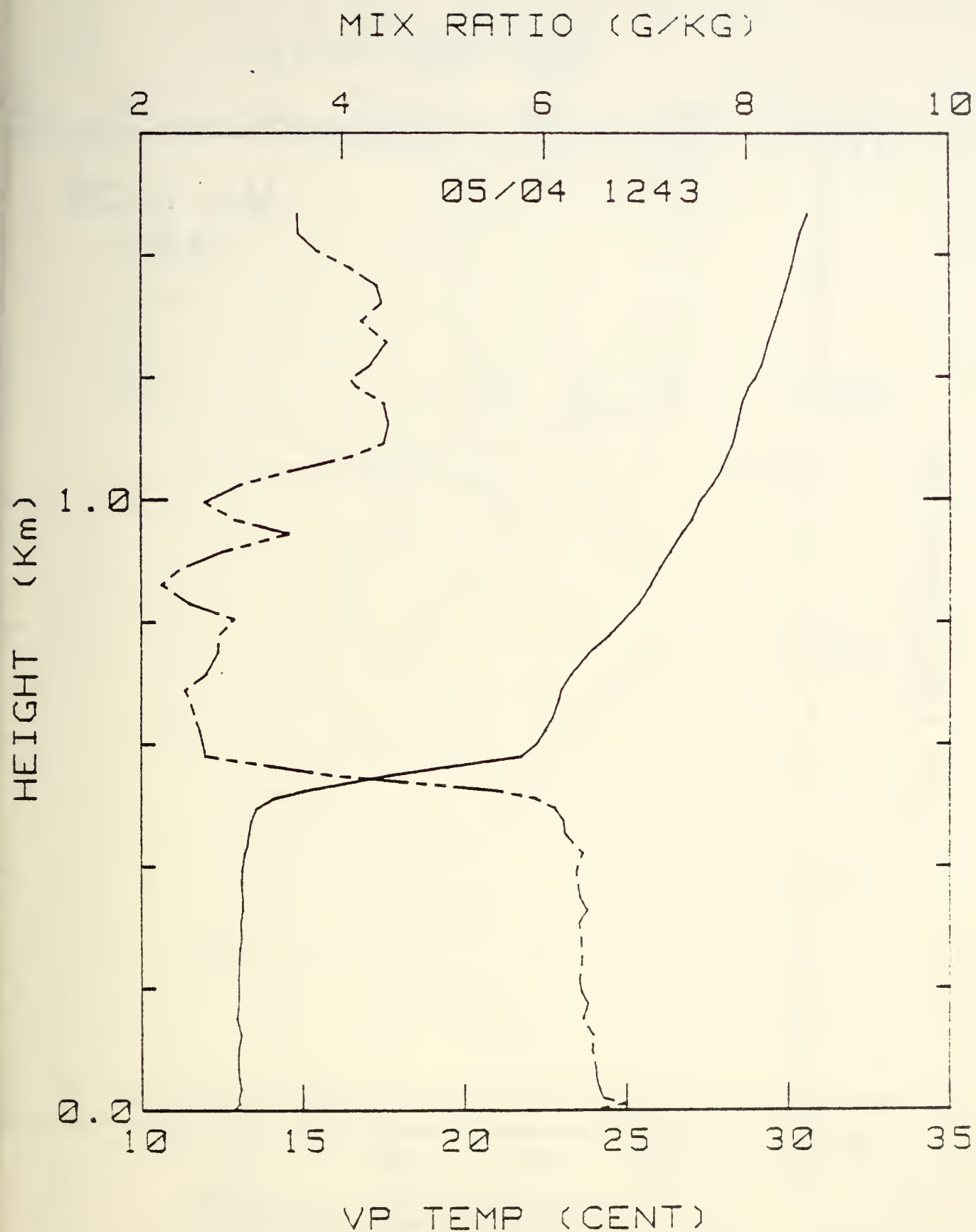


Figure A16a. Mean profile for MG 5/4 1244.

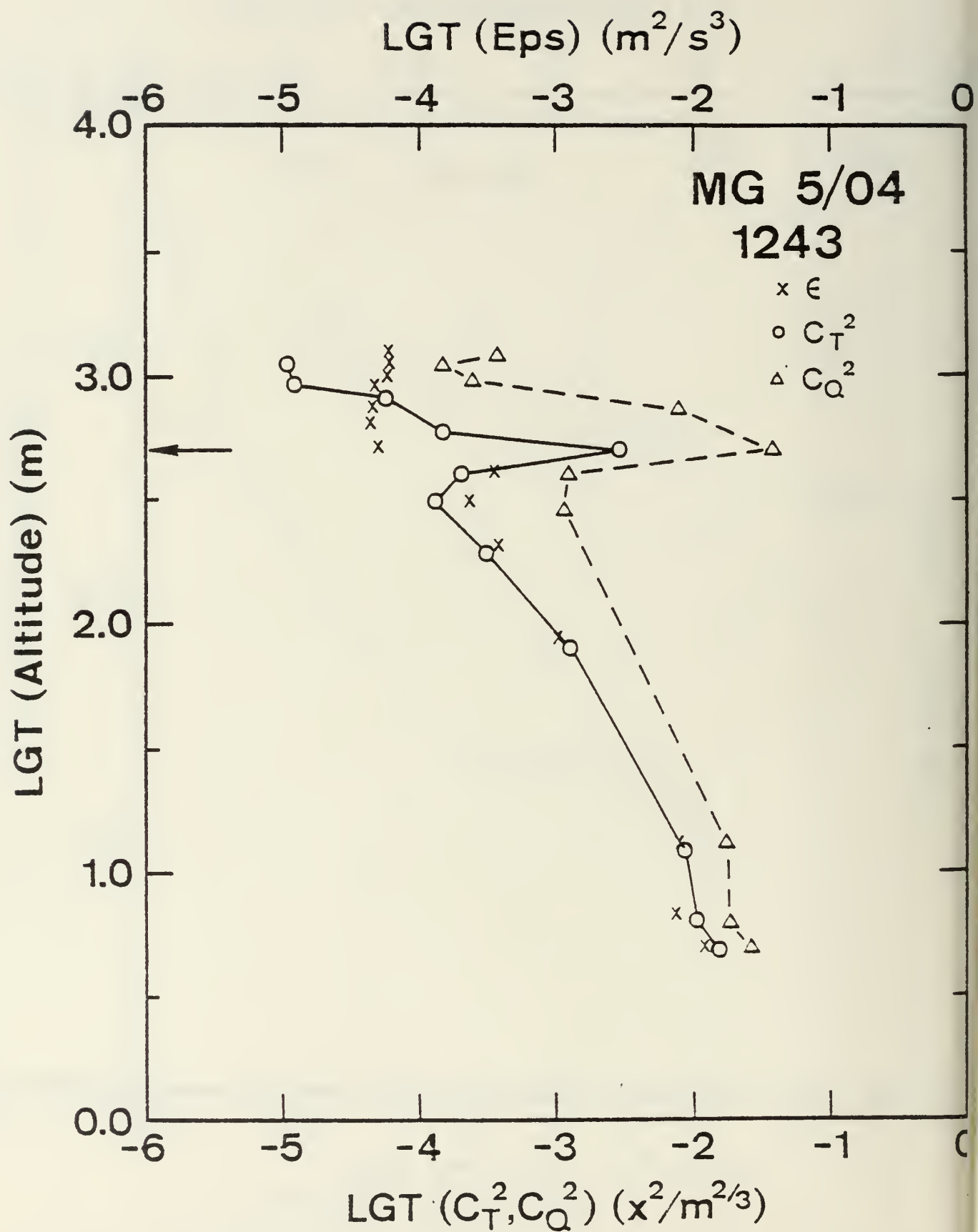


Figure A16b. Turbulence profile for MG 5/4 1244.

MIX RATIO (G/KG)

2 4 6 8 10

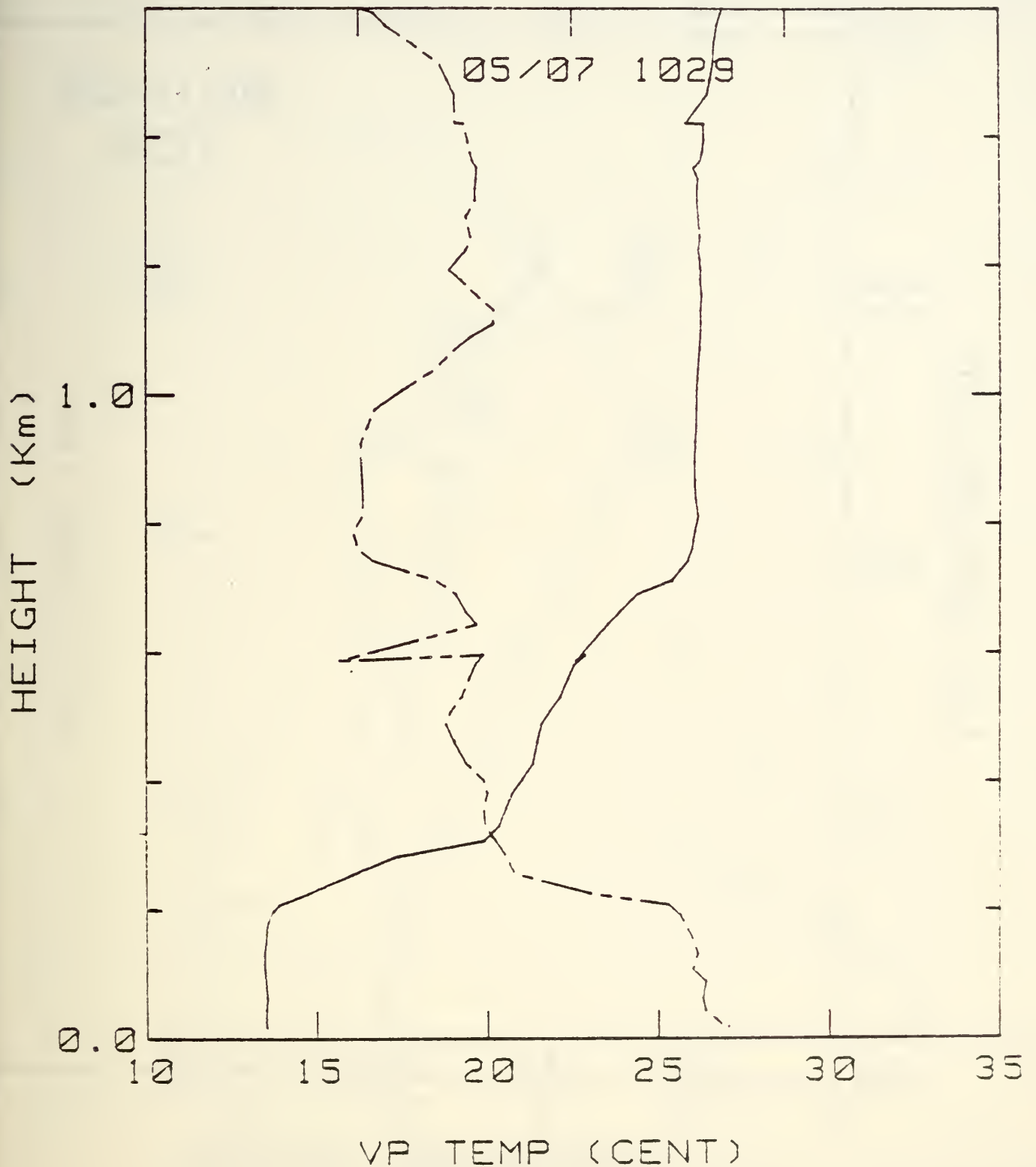


Figure A17a. Mean profile for MG 5/7 1043.

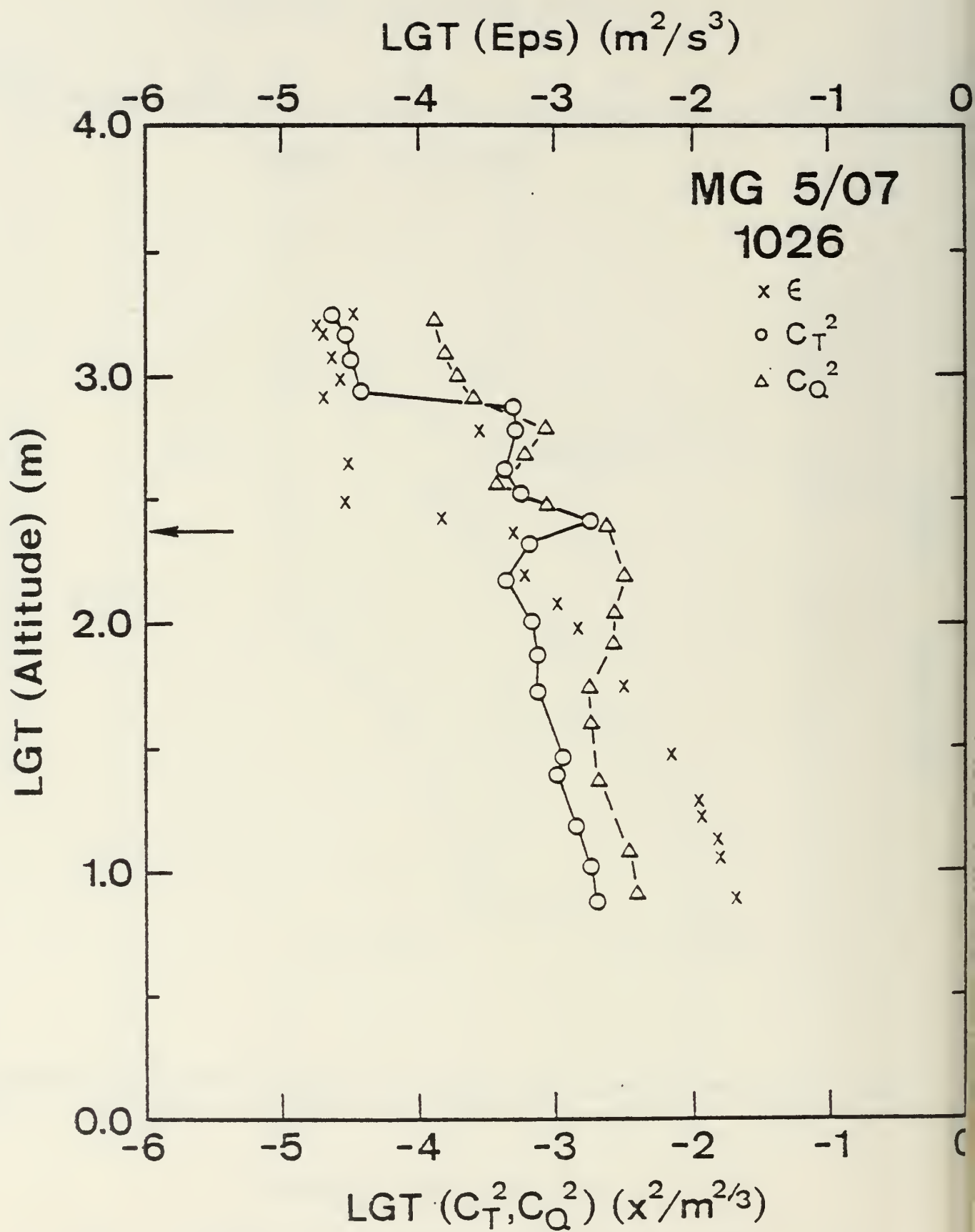


Figure A17b. Turbulence profile for MG 5/7 1043.

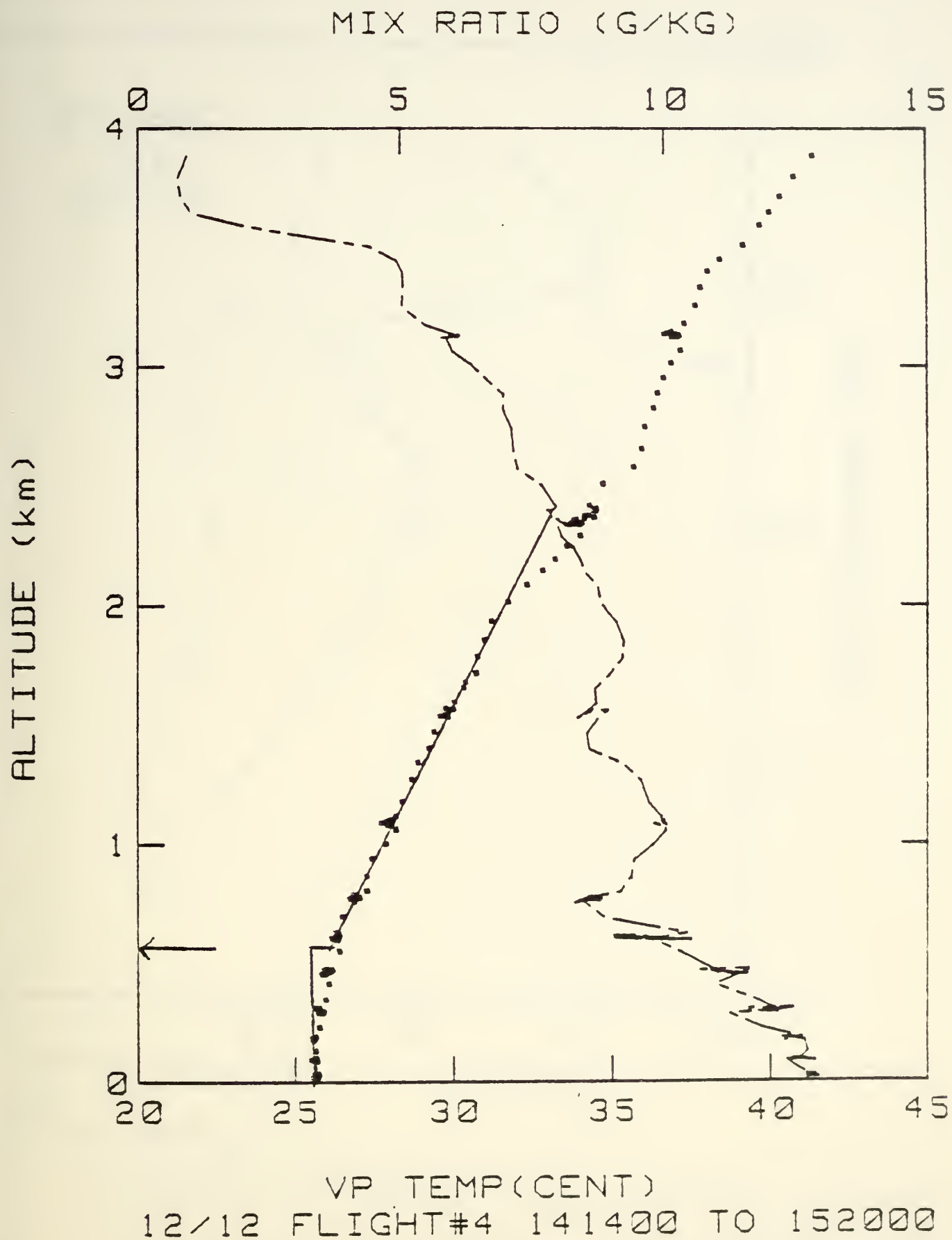


Figure A18a. Mean profile for

BH 12/12 1414.

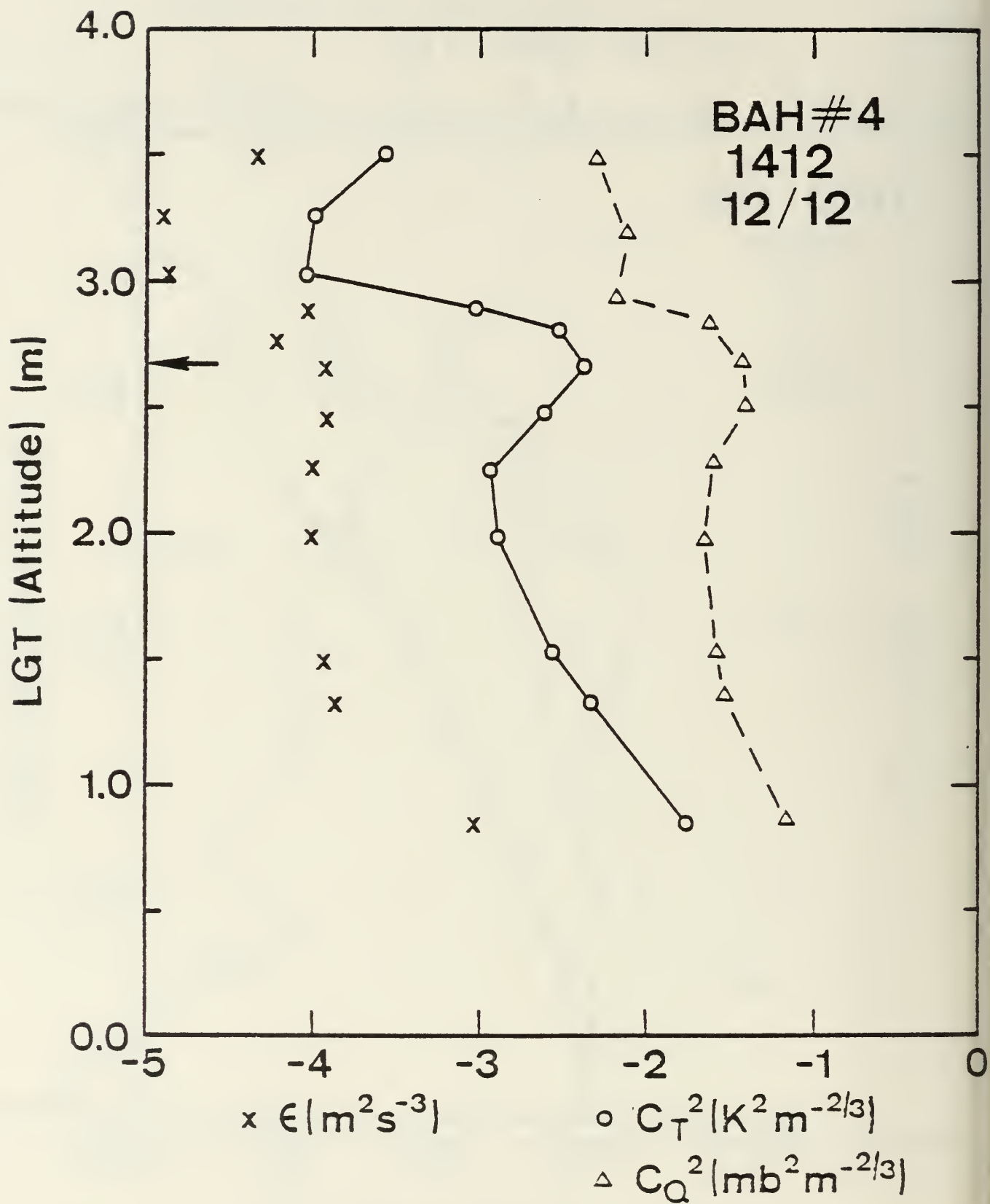


Figure A16b. Turbulence profile for BH 12/12 1414.

MIX RATIO (G/G)

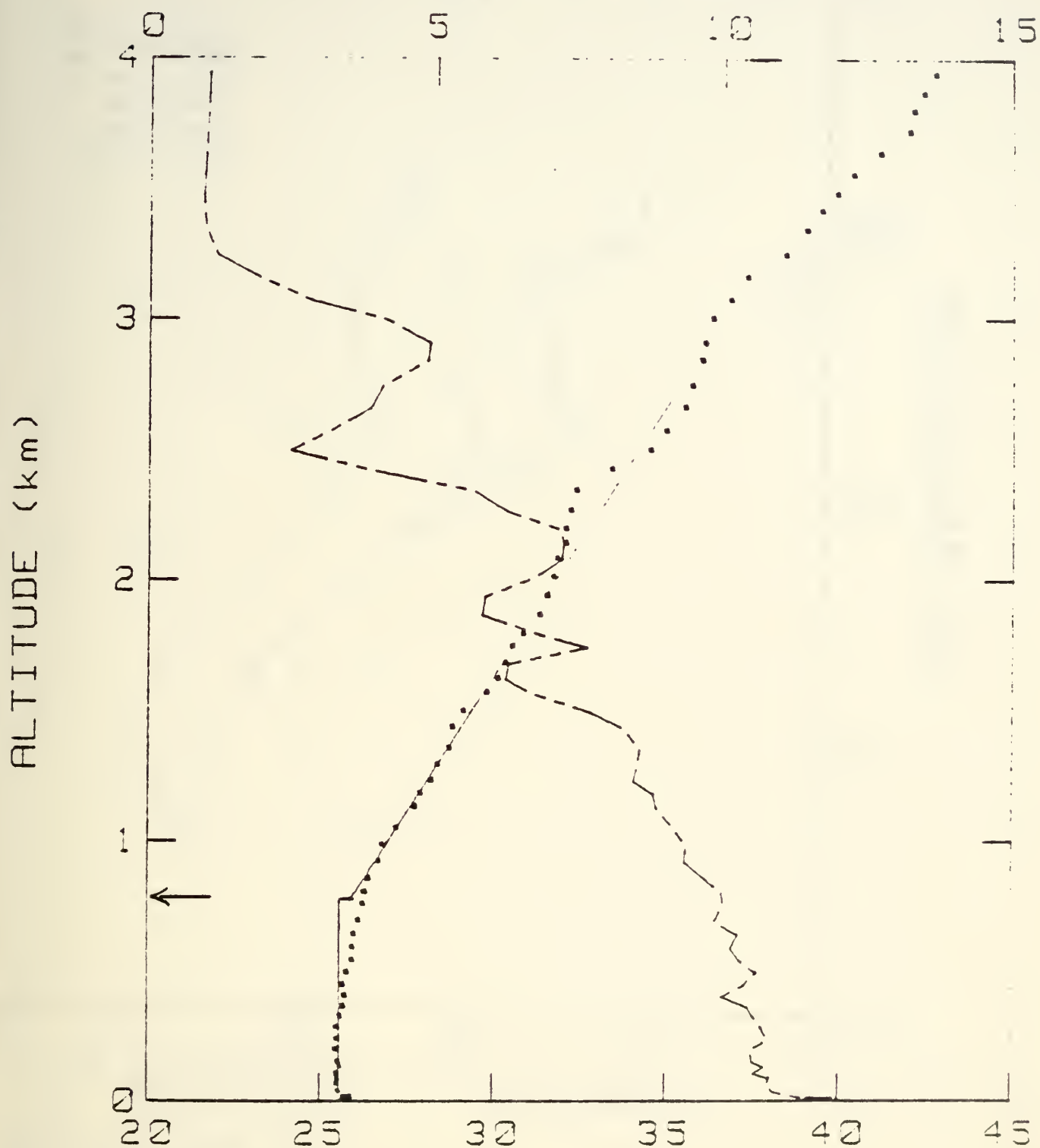


Figure A19a. Mean profile for

BH 12/13 1540.

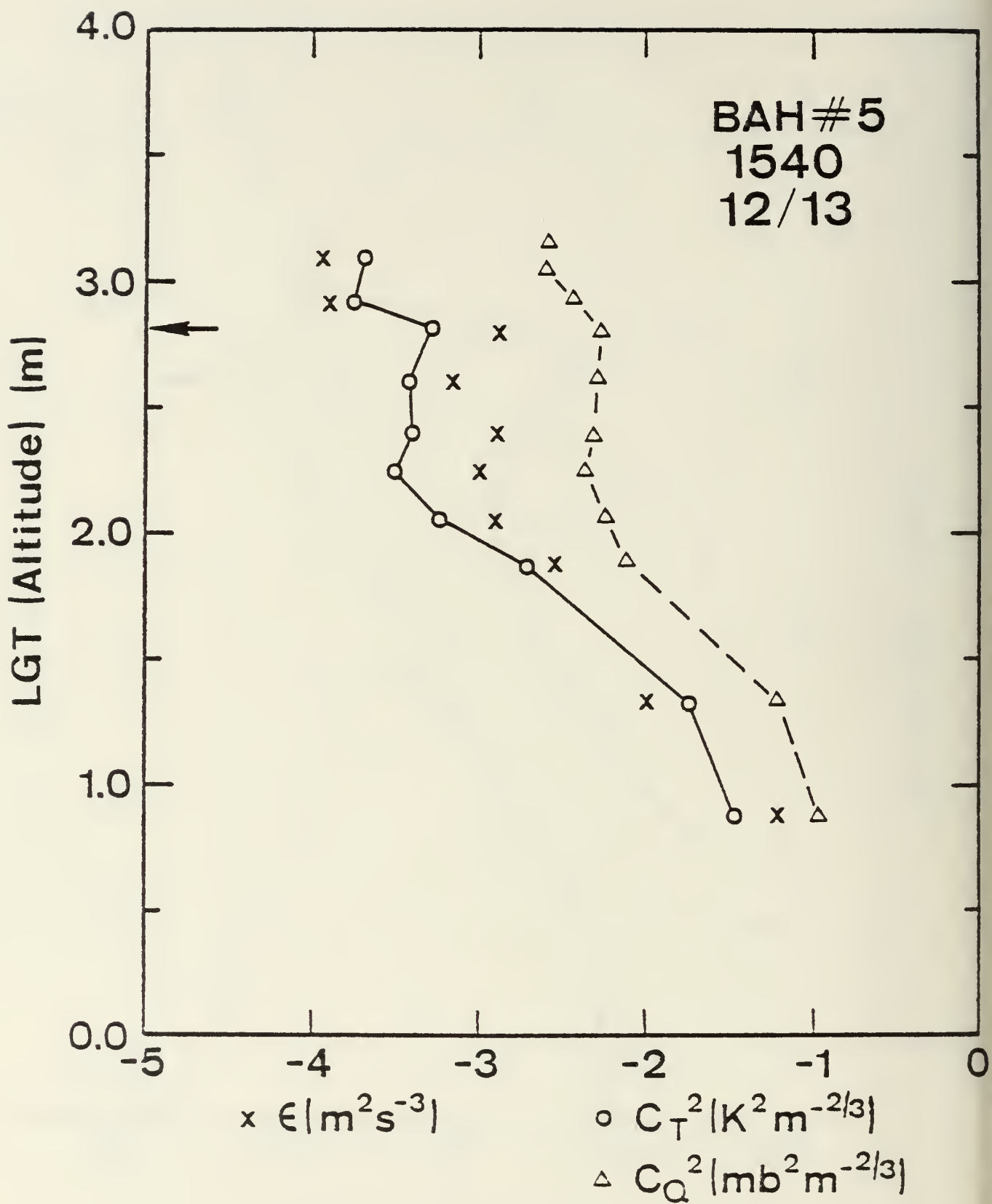
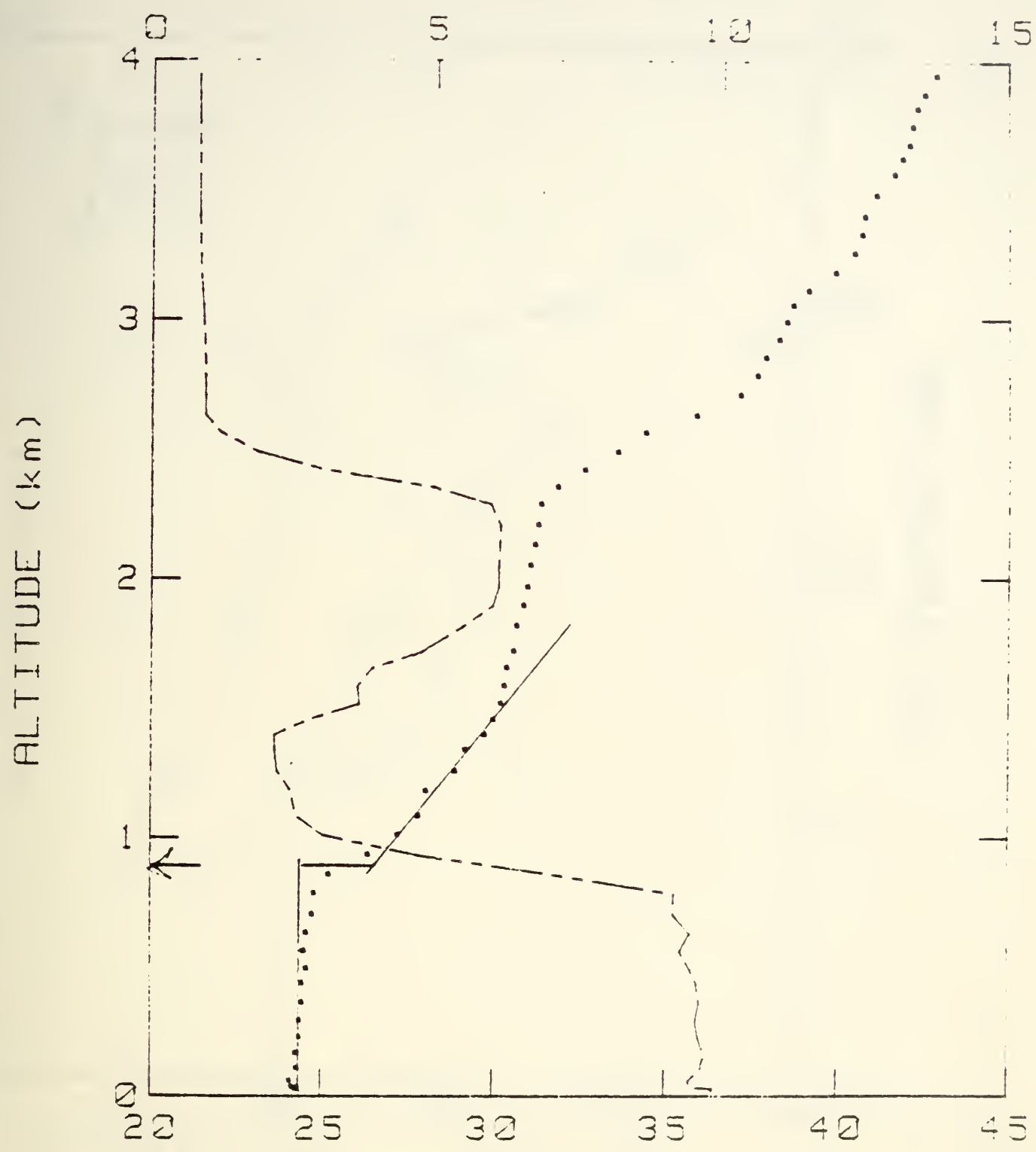


Figure A19b. Turbulence profile for BH 12/13 1540.

111-42111-10-11



VP TEMP (CENT)
12/14 FLIGHT#4 132100 TO 135200

Figure A20a. Mean profile for BH 12/14 1300.

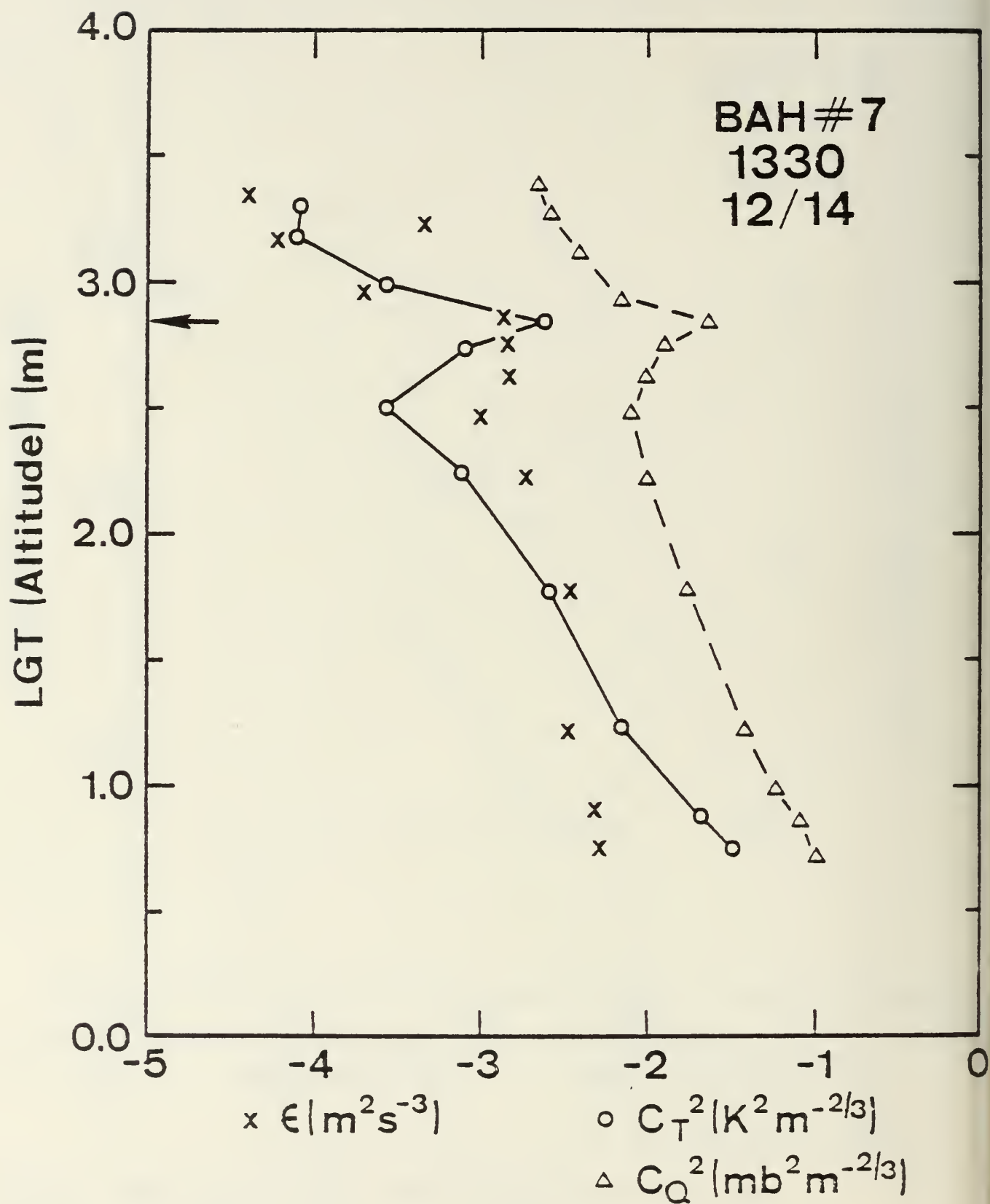
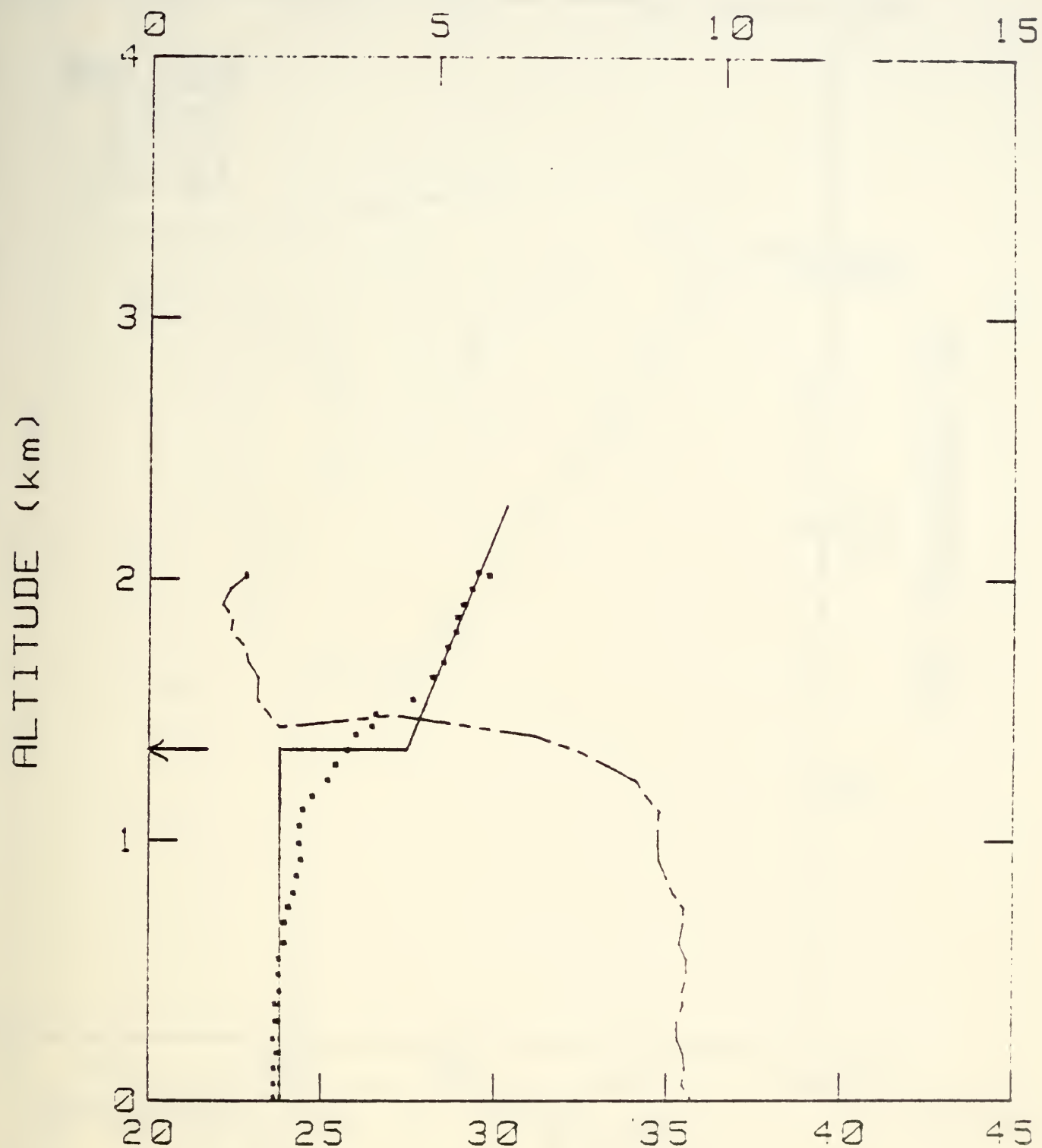


Figure A20b. Turbulence profile for BH 12/14 1330.

MIX RATIO (G/KG)



VP TEMP (CENT)
12/15 FLIGHT#8 133300 TO 134700

Figure A21a. Mean profile for BH 12/15 1333.

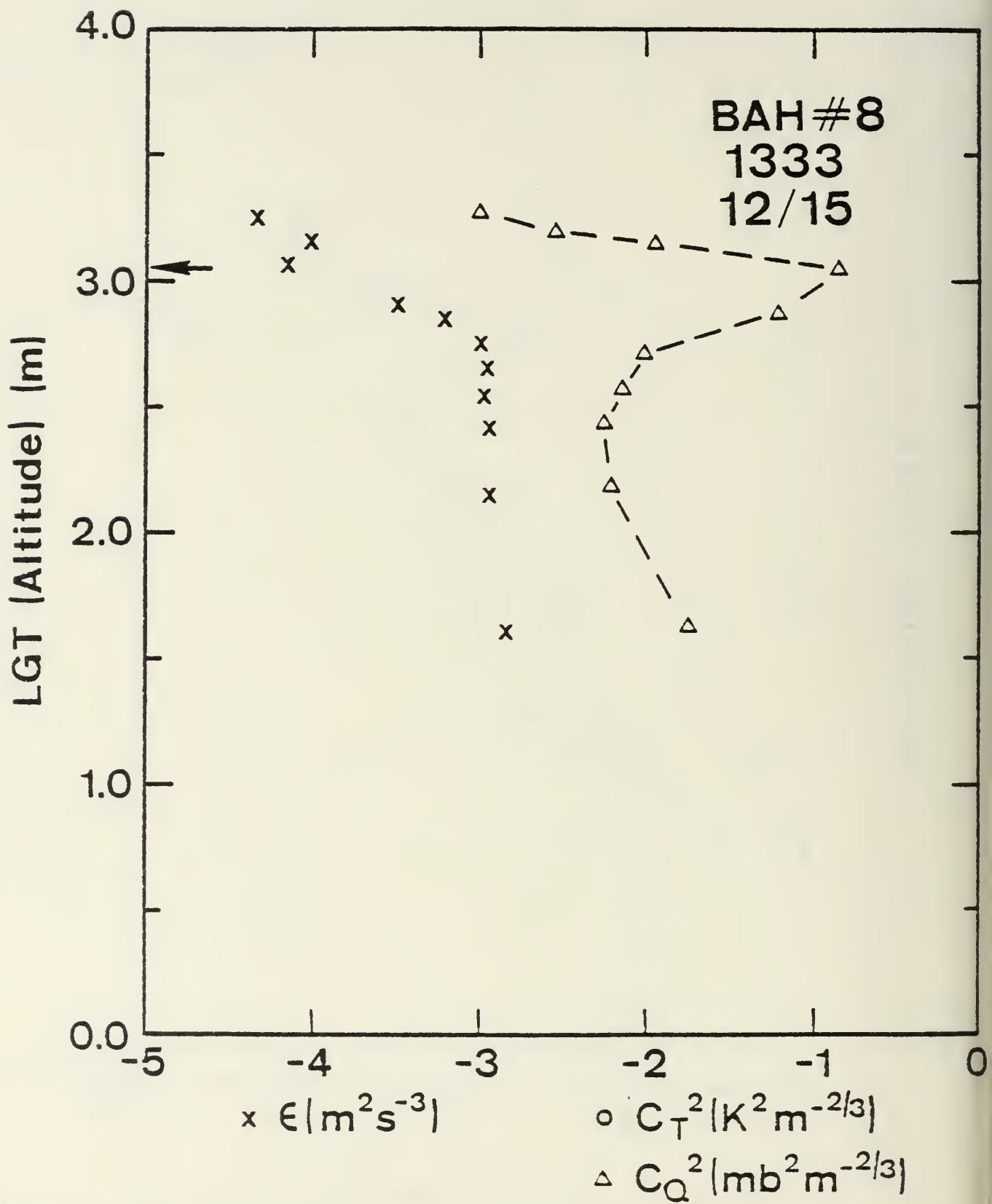


Figure A21b. Turbulence profile for BH 12/15 1333.

MIX RATIO (G/KG)

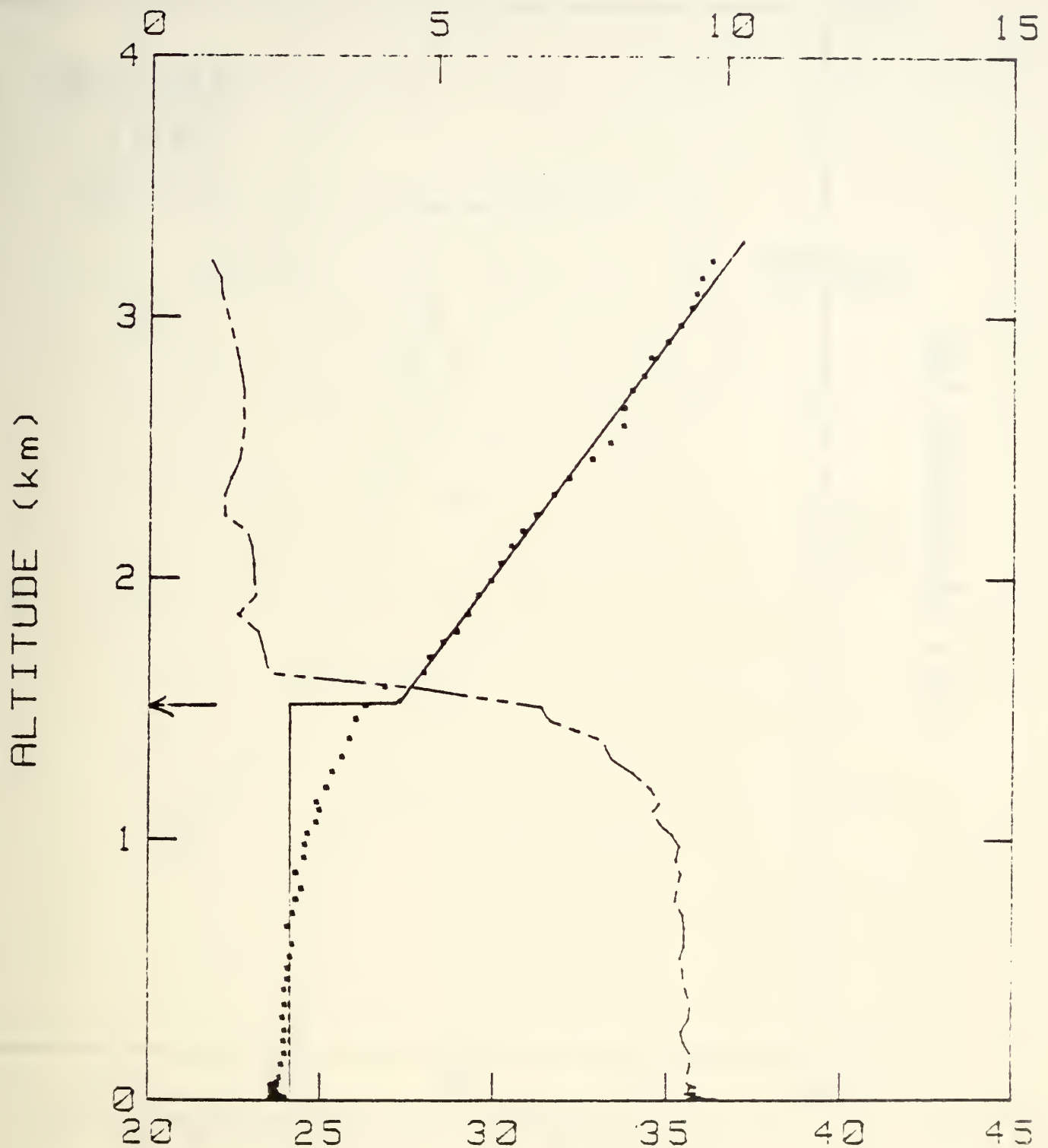


Figure A22a. Mean profile for

BH 12/15 1347.

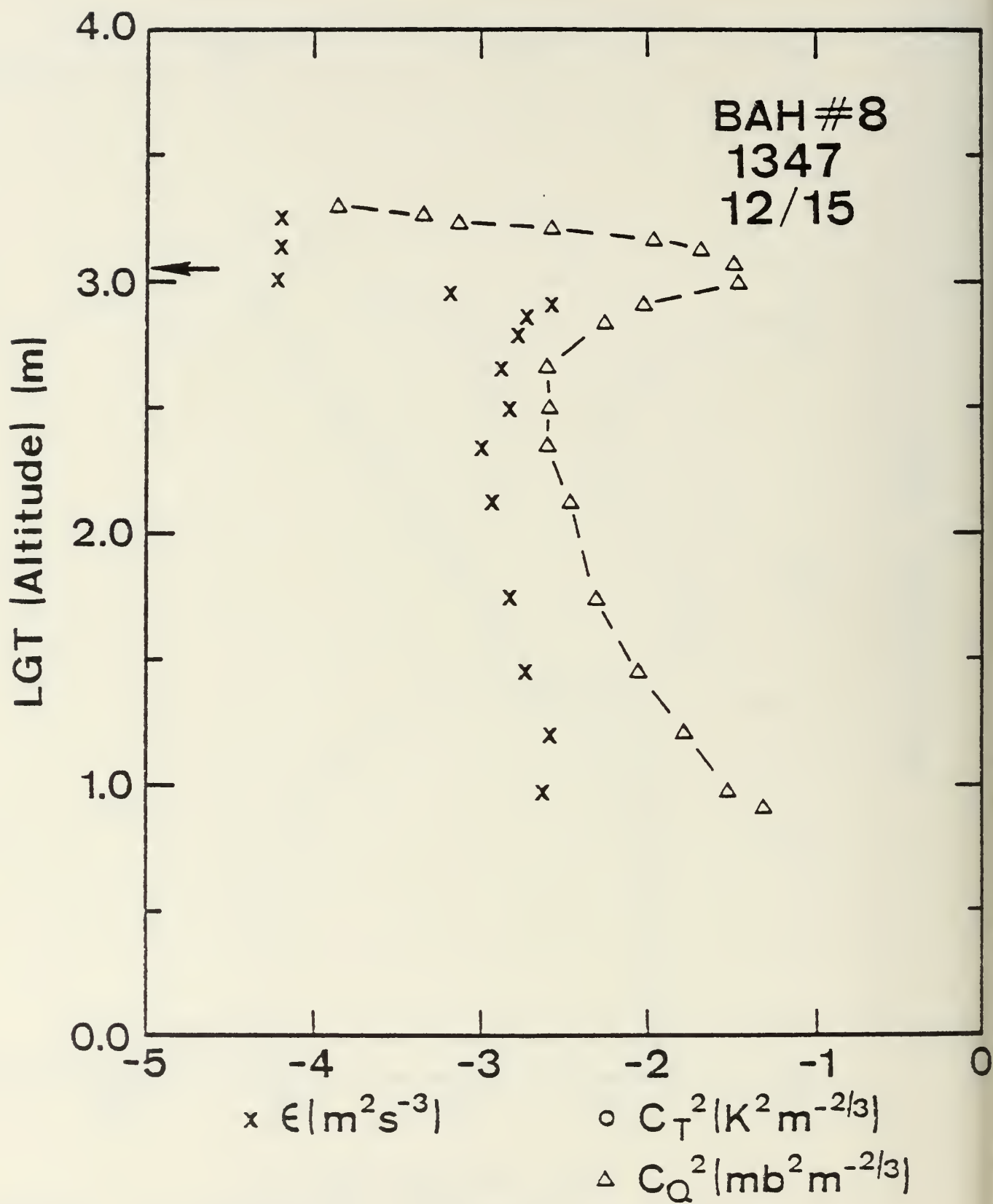
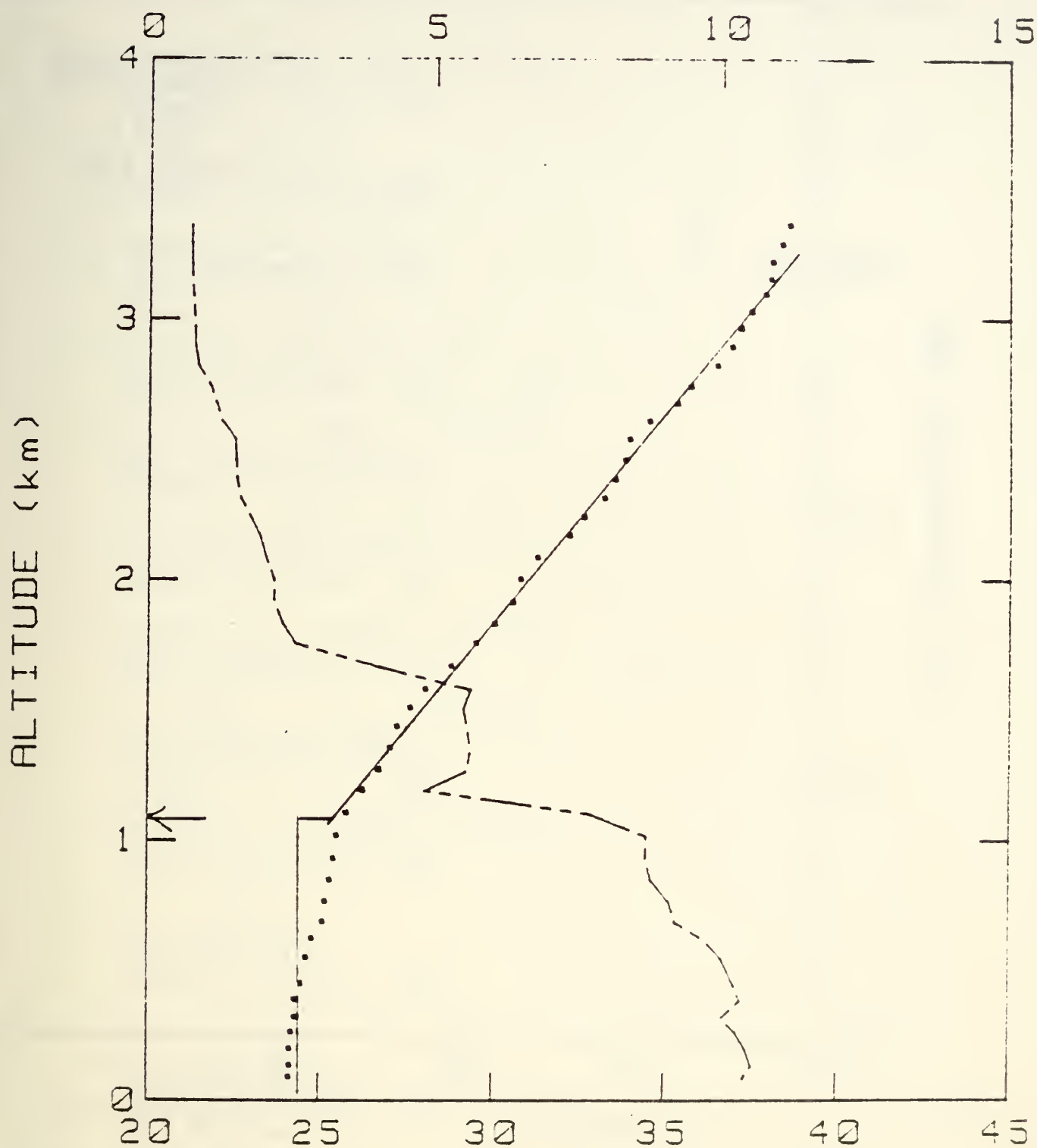


Figure A22b. Turbulence profile: for BH 12/15 1347.

MIX RATIO (G/KG)



VP TEMP (CENT)

12/15 FLIGHT#8 163100 TO 164900

Figure A23a. Mean profile for

BH 12/15 1637.

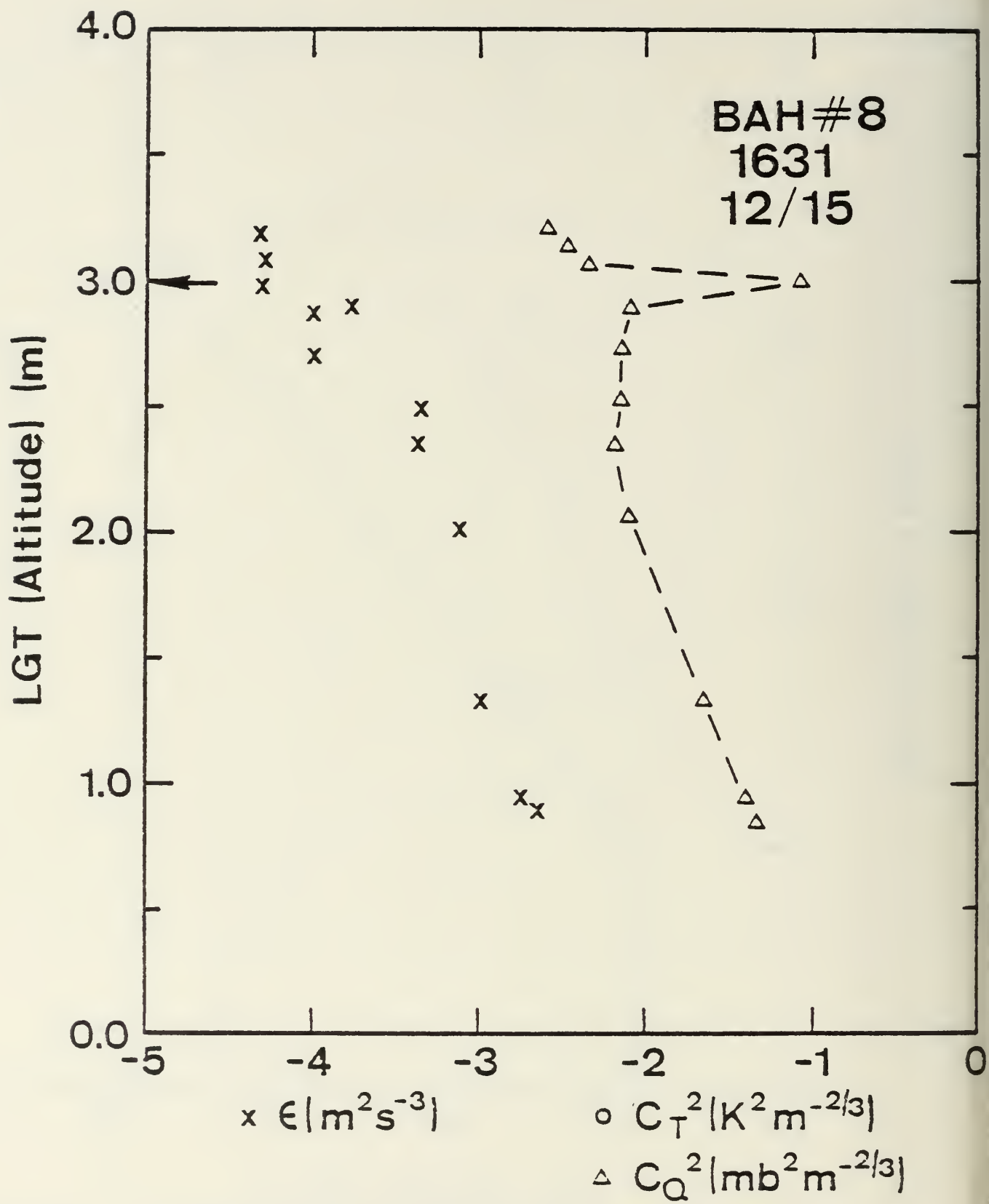


Figure A23b. Turbulence profile for BH 12/15 1637.

DISTRIBUTION LIST

	No. of Copies
1. Defense Technical Information Center Cameron Station Alexandria, Virginia 22314	2
2. Library, Code 0142 Naval Postgraduate School Monterey, California 93940	2
3. Dean of Research, Code 012 Naval Postgraduate School Monterey, California 93940	1
4. Professor J. Dyer, Code 61Dy Naval Postgraduate School Monterey, California 93940	1
5. Professor R. J. Renard, Code 63Rd Naval Postgraduate School Monterey, California 93940	1
6. Professor C.N.K. Mooers, Code 68Mr Naval Postgraduate School Monterey, California 93940	1
7. Professor K. L. Davidson, Code 63Ds Naval Postgraduate School Monterey, California 93940	10
8. Professor G. E. Schacher, Code 61Sq Naval Postgraduate School Monterey, California 93940	10
9. Assoc Prof R. W. Garwood, Code 68Gd Naval Postgraduate School Monterey, California 93940	1
10. Dr. C. W. Fairall BDM Corporation 1340 Munras Street Monterey, California 93940	10
11. Mr. Don Spiel BDM Corporation 1340 Munras Street Monterey, California 93940	2
12. Dr. A. Weinstein Director of Research Naval Environmental Prediction Research Facility Monterey, California 93940	1

13. CAPT K. Van Sickle 1
Naval Environmental Prediction Research Facility
Monterey, California 93940
14. Dr. A. Goroch 1
Naval Environmental Prediction Research Facility
Monterey, California 93940
15. Dr. Alex Shlanta, Code 3173 1
Naval Weapons Center
China Lake, California 93555
16. Dr. Barry Katz, Code R42 1
Naval Surface Weapons Center
White Oak Laboratory
Silver Spring, Maryland 20362
17. Dr. J. H. Richter, Code 532 1
Naval Ocean Systems Center
San Diego, California 92152
18. Dr. Lothar Ruhnke, Code 8320 1
Naval Research Laboratory
Washington, D.C. 20375
19. Mr. Herb Hitney, Code 532 1
Naval Ocean Systems Center
San Diego, California 92152
20. Mr. Herb Hughes, Code 532 1
Naval Ocean Systems Center
San Diego, California 92152
21. Mr. Stuart Gatham, Code 8320 1
Naval Research Laboratory
Washington, DC 20375
22. LCDR Stan Grigsby, PMS-405 1
Naval Sea Systems Command
Washington, DC 20360
23. Dr. Steven Burke 1
Naval Environmental Prediction Research Facility
Monterey, California 93940
24. Mr. Sam Brand 1
Naval Environmental Prediction Research Facility
Monterey, California 93940

25. Mr. Paul Banas, Code 9220 1
Naval Oceanographic Office
NSTL Station, Mississippi 39522
26. Dr. Paul Moersdorf, Code 9220 1
Naval Oceanographic Office
NSTL Station, Mississippi 39522
27. LT Mark Schultz 1
Naval Environmental Prediction Research Facility
Monterey, California 93940
28. Mr. Ted Zuba, Code AIR-370 1
Naval Air Systems Command
Washington, DC 20360
29. Mr. Jay Rosenthal 1
Geophysics Division
Pacific Missile Range
Point Mugu, California 93042
30. Dr. Michael J. Kraus 1
AFGL/LYS
Hanscom AFB, Massachusetts 01731
31. MAJ Bob Wright 1
AWS/DOOE
Scott AFB, Illinois 62225
32. MAJ Ed Kolczynski 1
AWS/SYX
Scott AFB, Illinois 62225
33. Mr. Joel S. Davis 1
Defense Sciences Division
Science Applications, Inc.
1010 Woodman Drive, Suite 200
Dayton, Ohio 45432
34. Mr. L. Biberman 1
Institute for Defense Analysis
400 Army Navy Drive
Arlington, Virginia 22202
35. Dr. Richard Gomez 1
DELAS-EO-MO
Atmospheric Sciences Laboratory
White Sands, New Mexico 88002
36. Dr. R. Fenn 1
Air Force Geophysics Laboratory
Hanscom AFB, Massachusetts 02173

37. Mr. Glen Spaulding, MAT 72 1
Naval Material Command
Washington, DC 20362

38. Dr. Paul Twitchell 1
Office of Naval Research
666 Summer Street
Boston, Massachusetts 02210

39. CDR Thomas Callaham, Code N341 1
Naval Oceanography Command
NSTL Station, Mississippi 39529

40. Dr. C. A. Friehe 1
Deputy Manager for Research, RAF
National Center for Atmospheric Research
Boulder, Colorado 80307

41. Dr. J. C. Wyngaard 1
CIRES
University of Colorado/NOAA
Boulder, Colorado 80309

42. Dr. Marvin L. Wesely 1
Radiological and Environmental Research Division
Argonne National Laboratory
Argonne, Illinois 60439

43. Mr. Jim Hughes, Code 470 1
Office of Naval Research
800 N. Quincy Street
Arlington, Virginia 22217



DUDLEY KNOX LIBRARY



3 2768 00333299 0